

Estimation of Ice Basal Reflectivity of Byrd Glacier using RES data

By

Santhosh Kumar Malyala

Submitted to the graduate degree program in Electrical Engineering and Computer Science and the Graduate Faculty of the University of Kansas in partial fulfillment of the requirements for the degree of Master of Science.

Chair: Dr. Carl Leuschen

Co – Chair: Dr. Jilu Li

Dr. Christopher Allen

Dr. John Paden

Date Defended: 09 June 2017

The thesis committee for Santhosh Kumar Malyala certifies that this
is the approved version of the following thesis:

Estimation of Ice Basal Reflectivity of Byrd Glacier using RES data

Chair: Dr. Carl Leuschen

Co-Chair: Dr. Jilu Li

Date Approved: 09 June 2017

Abstract

Ice basal reflectivity is much needed for the determination of ice basal conditions and for the accurate modeling of ice sheets to estimate future global mean sea level rise. Reflectivity values can be determined from the received radio echo sounding data if the power loss caused by different components along the two-way transmission of electromagnetic waves is accurately compensated.

For the large volume of received radio echo sounding data collected over Byrd glacier in 2011-2012 with a multichannel radar system, the spherical spreading loss caused due to two-way propagation, power reduction due to roughness and relative englacial attenuation is compensated to estimate the relative reflectivity values of the Byrd glacier ice base.

In order to estimate the scattered incoherent power component due to roughness, the distributions of echo amplitudes returned from the air-firn interface and from the ice – bed interface are modeled to estimate RMS height variations. The englacial attenuation rate for two-way propagation along the ice depth is modeled using the collected radar data. The estimated air-firn interface roughness parameters are relatively cross verified using Neal's method and with correlations to the Landsat image mosaic of Antarctica. Estimated relative basal reflectivity values are validated using cross-over analysis and abruptness index measurements. From the Byrd relative reflectivity map, the corresponding echograms at the locations of potential subglacial water systems are checked for observable lake features.

The results are checked for correlations with previously predicted lake locations and subglacial flow paths. While the results do not exactly match with the previously identified locations with elevation changes, high relative reflectivity values are observed close to those locations, aligning exactly or close to previously predicted flow paths providing a new window into the subglacial hydrological network. Relative reflectivity values are clustered to indicate the different potential basal conditions beneath the Byrd glacier.

Acknowledgements

First, I would like to thank Dr. Jilu Li, for guiding and enlightening me throughout the path of this research. This work would not have been possible without his help. I would like to thank Prof. Christopher Allen and Dr. James Stiles for their great teachings and long discussions. I would like to thank Dr. Stearns for all the Glaciology discussions and advices. I would like to thank Dr. Fernando Rodriguez-Morales and Dr. Prasad Gogineni for the constructive feedbacks. I would like to thank Dr. Carlton Leuschen and Dr. John Paden for the help and support. I would like to thank Logan and all my other friends for their continuous support and suggestions. I would also like to thank staff, faculty and students at CREsis for helping me through my Master's journey at KU.

Table of contents

Chapter 1 Introduction.....	1
1.1 Background and motivations	1
1.2 Thesis organization	4
Chapter 2 Radio echo sounding of ice sheets.....	5
2.1 Radar equations.....	5
2.2 Challenges in estimation of ice basal reflectivity	7
Chapter 3 Estimation of roughness	8
3.1 Methods to estimate RMS height σ	8
3.1.1 Method using power statistics.....	8
3.1.2 Method using waveforms.....	13
3.1.3 Method using amplitude distribution model	15
Chapter 4 Estimation of Ice attenuation.....	24
4.1 Previous methods	24
4.2 Modified englacial attenuation.....	30
4.3 Localized englacial attenuation.....	34
Chapter 5 Results and validation	38
5.1 Estimated relative reflectivity values	38
5.2 Validation using cross-over analysis:	39
5.3 Validation using geo-physical Features	44
5.4 Validation using abruptness index:	49
5.5 Correlation with predicted subglacial lakes and flow paths.....	52
5.6 Clustering of estimated basal conditions	57
Chapter 6 Summary and Conclusions	60
6.1 Summary	60
6.2 Conclusions and future work	61
References	

Table of Figures

Figure 1.1 Map of Antarctica (on left side) and Byrd Glacier with radar flight paths (on right side)	3
Figure 3.1 Estimated RMS height and correlation length for a smooth air – firn interface (20111213_05_009).....	10
Figure 3.2 Echogram of a smooth air – firn interface (20111213_05_009) Bottom right image shows the corresponding flight line of the echogram	10
Figure 3.3 Estimated RMS height and correlation length of a relatively rough air – firn interface	12
Figure 3.4 Echogram and flight path of a relatively rough air – firn interface (20111212_01_002) Bottom- right image shows the corresponding flight line of the echogram	12
Figure 3.5 Specular reflections of Byrd Glacier ice – bed interface	14
Figure 3.6 Bed echoes of smooth and relatively rough interfaces.	15
Figure 3.7 Distribution of the returned echoes amplitude values from a smooth air – firn interface location	16
Figure 3.8 Distribution of amplitude values of returned echoes from a rough air – firn interface location	16
Figure 3.9 RMS height of smooth air – firn interface (20111213_05_009)	18
Figure 3.10 RMS height of relatively rough air – firn interface (20111212_01_002).....	18
Figure 3.11 Roughness estimates for data frame 20111213_05_009, top plot represents estimated roughness using amplitude distribution method and bottom plot represents estimated roughness using Neal’s method	19
Figure 3.12 Roughness estimates for data frame 20111212_02_005 – top plot represents estimated roughness using amplitude distribution model method – bottom plot represents estimated roughness using Neal’s method	19
Figure 3.13 Air – firn interface roughness map	20
Figure 3.14 Scaled images of estimated air – firn interface roughness map.....	21
Figure 3.15 Ice – bed interface roughness	22

Figure 3.16 InSAR-based velocity map of Antarctica colorbar represents the velocity magnitude in km/yr	23
Figure 4.1 Echogram of Greenland 20110502_02_002 data frame	24
Figure 4.2 Echogram of 20111213_05_009 data frame, Byrd Glacier	25
Figure 4.3 Echogram of 20111212_01_002 data frame of Byrd Glacier.....	26
Figure 4.4 Relative reflectivity map for $Na = 5$ dB/km (top left), $Na = 10$ dB/km (top right), $Na = 15$ dB/km (bottom left) and $Na = 20$ dB/km (bottom right)	28
Figure 4.5 Relative englacial attenuation (dB) using a 10 dB/km englacial attenuation rate	29
Figure 4.6 Need for spatially variable attenuation rate	30
Figure 4.7 Estimated Relative englacial attenuation in dB using modified attenuation rate	32
Figure 4.8 Relative reflectivity values estimated using the modified attenuation rate	33
Figure 4.9 Histograms of estimated relative reflectivity values using modeled attenuation rate (on left) and constant attenuation rate (on right).....	34
Figure 4.10 Variation of assumed Na for different depth values	35
Figure 4.11 Na values (shown in red color) in along track dimension and the apparent attenuation (shown in blue)	35
Figure 4.12 Estimated Na for short intervals in the along track direction.....	36
Figure 4.13 Estimated relative englacial attenuation in dB assuming a localized attenuation rate (shown on the left side) and the depth at the corresponding locations (shown on the right side)	37
Figure 5.1 Relative reflectivity values using unique Na for each 1km along track interval	38
Figure 5.2 Relative reflectivity map with cross over locations.....	39
Figure 5.3 Difference in estimated relative reflectivity values at cross over locations	40
Figure 5.4 Histogram of estimated relative reflectivity value differences at cross over locations	41
Figure 5.5 Difference in depth values of ice sheet at cross over locations	41

Figure 5.6 Differences in estimated relative reflectivity values and depth at the corresponding locations; these corresponding locations on the map are shown in top-right figure.....	42
Figure 5.7 Plots of received power from ice-bed interface along with the roll of aircraft from corresponding flight path locations 20111212_01_018 (on left side) and 20111228_02_001 (on right side)	43
Figure 5.8 Examples for high thickness of the ice sheet with corresponding flight path locations and estimated relative reflectivity map shown inside the echogram	44
Figure 5.9 Examples for ice-bed interface configurations (highlighted with a black color rectangle) with corresponding flight path locations and estimated relative reflectivity map shown inside the echogram ..	45
Figure 5.10 Examples for high dielectric contrast at the ice – bed interface (highlighted with a black color rectangle) with corresponding flight paths locations and estimated relative reflectivity map shown inside the echogram.....	46
Figure 5.11 Examples for a flat air-firn interface and flat ice – bed interface (highlighted with white and black color rectangles, respectively) with corresponding flight path locations and estimated relative reflectivity map shown inside the echogram.....	47
Figure 5.12 Examples for angle of internal reflectors dipping greater than bed topography (highlighted with a black color rectangle) with corresponding flight path locations and estimated relative reflectivity map shown inside the echogram	48
Figure 5.13 Abruptness index and estimated relative reflectivity maps	49
Figure 5.14 Abruptness values, relative reflectivity values and echogram with flight path locations for data frame 20111201_04_002.....	50
Figure 5.15 Abruptness values, relative reflectivity values and echogram with flight path locations for data frame 20111213_05_008.....	51
Figure 5.16 Volume change history of seventeen sites.....	52
Figure 5.17 Hydraulic potential map of Byrd glacier in dB	53
Figure 5.18 2D interpolated hydraulic potential map in dB.....	54

Figure 5.19 Equipotential contours of φ	54
Figure 5.20 Estimated relative reflectivity map with flow paths	55
Figure 5.21 Areas with predicted flow path (highlighted in black colored rectangle) in echogram and in corresponding 20111219_04_004 flight path	56
Figure 5.22 Echograms of flight path 20111214_04_012 and 20111219_04_003 (shown inside echograms) from estimated new potential subglacial water flow path locations (shown in black colored rectangles)	57
Figure 5.23 Sum of with-in cluster sums of point-to-centroid L1 distances	58
Figure 5.24 Sum of with-in cluster sums of point-to-centroid L2 distances	59
Figure 5.25 Estimated clusters of basal conditions	59

Chapter 1 Introduction

1.1 Background and motivations

The climate-related changes, such as rising temperatures, rapidly retreating glaciers, thawing permafrost, rising sea level, increase in downpours, extended growing seasons, lengthening ice-free seasons in oceans, rivers and lakes, alterations in river flows and earlier snowmelt, are being observed globally [1]. Out of all these indicators, global mean sea level value can be used as an indicator of climate change, because the density of sea water depends on the temperature, and the global sea level represents many aspects of hydrological cycles. The global sea level parameter is also used as a key observational constraint on climate models [2].

The current (Feb 2017) rate of change of global mean sea level is $\uparrow 3.4 (\pm 0.4)$ mm/yr [3] and according to fifth assessment report of the IPCC (Intergovernmental Panel on Climate Change) the estimated sea level rise by the year 2100 will likely be about 52-98 cm for RCP8.5 (medium confidence) [4]. A 1- meter rise of sea level could affect the lives of more than 100 million people [2]. The major sources of this sea level rise are – expansion of sea water as it warms and added water from melting land ice [3].

The two major ice sheets are Greenland and Antarctica. The ice sheet of Greenland extends almost 1.7 million square kilometers and could potentially contribute to a sea level rise of 7.3 m and the ice sheet of Antarctica extends almost 14 million square kilometers and could potentially contribute to a sea level rise of 57 m [5], [6]. In order to better understand the sea level pattern, the glaciers of Greenland and Antarctica are being studied to model the ice sheets because of their potential effects on sea-level change [7], [5]. The mass loss of an ice sheet directly contributes to sea level rise and the changes in the mass balance of Greenland and Antarctica are $\downarrow 281 (\pm 29)$ Gt/yr, and $\downarrow 118 (\pm 79)$ Gt/yr respectively [3].

The East Antarctic ice sheet (EAIS) alone extends about 10.2 million square kilometers [5] and could potentially contribute to a sea level rise of 52 m [6]. The subglacial lakes beneath the East Antarctica

ice sheet have been first reported in the early 1960s and 1970s [8]. An accelerated ice velocity is observed on Byrd glacier, East Antarctica, between December 2005 and February 2007 [9].

The catchment basin of Byrd Glacier (80.5° S, 160° E) is $1,070,400 \text{ km}^2$ and is the largest catchment basin in Antarctica and it funnels $20.6 \pm 1.6 \text{ Gt yr}^{-1}$ [10] of ice to the Ross Ice Shelf through a $\sim 75\text{km}$ long, $\sim 20\text{km}$ wide fjord [9]. There are over 300 subglacial lakes beneath Antarctica [11], and these subglacial lakes form an important component of the basal hydrological system which affects the dynamics of the Antarctic ice sheet [12]. Ice sheet surface elevation changes are used to infer the movement of subglacial water between subglacial lakes and along ice streams [13]. Seventeen sites of rapid ice-elevation changes have been identified within the Byrd Glacier catchment, potentially making the Byrd Glacier bed the most hydrologically active location in East Antarctica [14]. The time-lapse of Byrd Glacier's ice sheet flow can be observed [here](https://earthengine.google.com/timelapse/#v=-80.86076,154.56803,7.425,1atLng&t=1.80) (web link: <https://earthengine.google.com/timelapse/#v=-80.86076,154.56803,7.425,1atLng&t=1.80>) using Google's Earth Engine. The location of the Byrd glacier is shown in Figure 1.1.

The stability of grounding zones of an ice sheet depends on bed topography [15] [16] [17] and basal conditions [18]. Ice basal conditions are also much needed for the reliable and accurate modeling of ice sheets for the better understanding of ice flow dynamics to improve the prediction of future sea level rise. In the fifth assessment report of the IPCC, it is stated that the collapse of marine-based sectors of the Antarctic ice sheet, if initiated, could cause the stated likely range of sea level rise for the 21st century to rise substantially. It is also stated that significant uncertainties remain, particularly related to the magnitude and rate of the ice-sheet contribution for the 21st century and beyond [4].

The basal materials from ice core drilling provides us direct evidence of ice basal conditions, but drilling a bore hole into ice is expensive, spatially limited and could also potentially contaminate the ecosystems beneath the ice sheets. Other methods like seismic sounding have deeper penetration into ice bed materials than radio echo sounding but require more effort to setup, are more expensive and have smaller spatial coverage compared to radar. Radar is much more feasible than the methods involving

seismic experiments or drilling of boreholes to study complete glaciers due to its efficient large spatial coverage and cost effectiveness [19] [20]. InSAR can also be used to map the velocity of the glaciers [21]. All the information presented by these different methods can be used complementary to obtain better results.

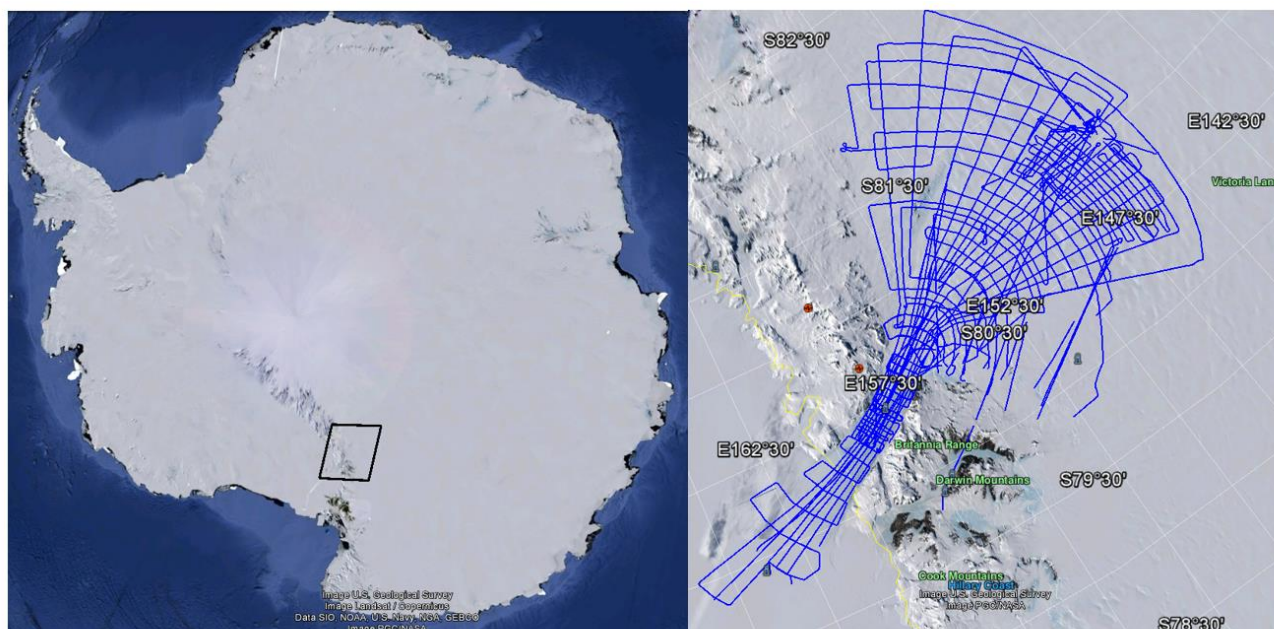


Figure 1.1 Map of Antarctica (on left side) and Byrd Glacier with radar flight paths (on right side)

The purpose of this work is to estimate the relative reflectivity values of the Byrd glacier and to better understand the subglacial hydrological system beneath Byrd glacier. The estimated relative reflectivity values can be used to better understand the ice flow dynamics and to better model the ice sheets. In this work, the relative reflectivity values are estimated, from data collected over Byrd glacier in 2011-2012 with multichannel radar, by compensating the power loss in the received echo returns caused by roughness, spherical spreading loss, and englacial attenuation.

1.2 Thesis organization

In Chapter 2, the ice sheet structure is discussed and the radio echo sounding method for estimating the basal reflectivity values is introduced, including radar equations. The challenges in estimating the reflectivity values from the radar data are also discussed.

In Chapter 3, the roughness values of air- firn interface and ice – bed interface are estimated using received data statistics. The estimated air-firn interface roughness values are relatively validated using the Neal's method and correlations from the LIMA (Landsat Image Mosaic of Antarctica). The estimated roughness maps of air – firn interface and ice – bed interface are also provided.

In Chapter 4, the methods to estimate englacial attenuation are discussed and the need for a new modeled attenuation rate is explained. The englacial attenuation rate is estimated from the received data by assuming a localized attenuation rate and by using a modeled attenuation rate constant and the estimated englacial attenuation map is provided.

In Chapter 5, the relative reflectivity values are estimated and a relative reflectivity map is generated for the Byrd Glacial catchment area. Cross-over analysis is done to validate the method used to estimate the relative reflectivity values. The corresponding echograms at the locations of potential subglacial water systems are checked for the observable lake features. The estimated relative reflectivity map is also validated using the abruptness index measurements. The locations with higher relative reflectivity values are checked with the previously predicted lake locations and subglacial flow paths to find correlations.

In Chapter 6, summary and conclusions of this work are presented and additional steps that can be taken to improve the accuracy of the estimated relative reflectivity values are also discussed.

Chapter 2 Radio echo sounding of ice sheets

2.1 Radar equations

An ice sheet is formed by the accumulation of snow. The elevation of Greenland and east Antarctica ice sheets are 3 km to 4 km high at their summits [22]. The internal layers of the ice sheet contain accumulation information of snowfall in each year. The basal condition is the state of the ice – bed interface, such as if it is melting, frozen or thawed etc. As we move from the top of the ice sheet towards its base, the temperature profile of the ice sheet increases due to geothermal heat.

Ice sounding radar operates by transmitting signals and receiving the backscattered echoes at a VHF band so that the attenuation of the EM wave in the ice is low enough to penetrate the ice sheet. The required along-track resolution is achieved by SAR processing. The reflected radar-sounding echoes are directly related to the dielectric contrast of two media, so radar echo sounding (RES) data has been used to interpret the basal conditions from the estimated reflectivity values [23].

The signal power received (P_r) by the radar from an ice sheet with small scale roughness, is given by [24] [25]

$$P_r = P_t \left(\frac{\lambda}{4\pi} \right)^2 \frac{G_t G_r}{\left[2 \left(h + \frac{z}{n_i} \right) \right]^2 L_i^2} \rho |\langle R_b \rangle|^2 \quad (2.1)$$

where λ is the wavelength in air, G_t and G_r are the gains of transmit and receive antennas, ρ accounts for small roughness scattering effects, P_t is the transmitted power, h is the height of aircraft above ice, z is ice thickness, n_i is the index of refraction for ice, L_i is englacial attenuation for one-way transmission, and $\langle R_b \rangle$ is the averaged basal reflection coefficient over the imaged resolution cell, given by

$$R_b = \frac{\sqrt{\varepsilon_1} - \sqrt{\varepsilon_2}}{\sqrt{\varepsilon_1} + \sqrt{\varepsilon_2}} \quad (2.2)$$

where ε_1 and ε_2 are the complex dielectric permittivity of two media interface expressed as $\varepsilon = \varepsilon_r(1 - j \tan\delta)$, ε_r is the relative permittivity and $\tan\delta$ is the loss tangent.

The ice sheet surface undulations in the radar illuminating area will result in the reduction of power reflected by a factor of ρ due to the phase variations ϕ caused by vertical root mean square variations of the air – firm interface [23]. Similar is the case for the ice – bed interface. The power reduction factor ρ caused by roughness can be calculated by [23]

$$\rho = e^{-\phi^2} I_0^2\left(\frac{\phi^2}{2}\right) \quad (2.3)$$

where I_0 is the zeroth-order modified Bessel function of the first kind and ϕ is the phase shift which is given by

$$\phi = \frac{4\pi\sigma}{\lambda_s} \quad (2.4)$$

where σ is the vertical root mean square (RMS) displacement of the surface from its mean plane and λ_s is the wavelength at the reflecting surface. The phase shift in the returned echoes from the ice – bed interface due to the RMS displacement of air – firm interface and the RMS displacement of ice – bed interface are calculated using the equations 3.12 and 3.13 respectively from Chapter 3

The radar equation can be written in dB as

$$[P]_{dB} = [S]_{dB} - [G]_{dB} + [R]_{dB} - [L]_{dB} \quad (2.5)$$

where P is the received power (after correcting for roughness), S is the system parameters including transmit power P_t , transmit gain G_t , receive gain G_r and processing gain. G is the geometric spreading loss, R is the ice – bed interface reflectivity, and L is the englacial attenuation

The total geometric spreading loss is calculated by

$$[G]_{dB} = 2\left[2\pi\left(h + \frac{z}{n_i}\right)\right]_{dB} \quad (2.6)$$

Geometrically corrected bed-echo power P^c is given by

$$[P]_{dB} + [G]_{dB} = [P^c]_{dB} = [S]_{dB} + [R]_{dB} - [L]_{dB} \quad (2.7)$$

Rearranging the above equation gives

$$[R]_{dB} = [P^c]_{dB} + [L]_{dB} - [S]_{dB} \quad (2.8)$$

2.2 Challenges in estimation of ice basal reflectivity

Assuming the system is well calibrated, data is noise free, and the effects of ice bed geometry on received power are negligible, the major challenges in constraining the reflectivity values R from the received RES data are accurate estimation of the englacial attenuation rate and losses due to air – firn interface roughness and ice – bed interface roughness [26]. The englacial attenuation depends on the dielectric permittivity of ice, which varies with depth and location, as different locations could have different impurity concentrations, density profiles and temperature profiles of the ice column [27]. The accurate estimation of englacial attenuation requires accurate estimation of the dielectric permittivity. In addition to the basal conditions, the returned echoes from ice – bed interface are affected by the roughness of the interface, topography of the interface, and roll effects of the aircraft. As mentioned, the estimation of losses due to roughness depends on the RMS height, and methods to estimate the RMS height are provided in Chapter 3 and the methods to estimate the englacial attenuation rate are given in Chapter 4.

Chapter 3 Estimation of roughness

The interface roughness is characterized by the RMS height variations of the interface. Whenever the transmitted pulse spreads across an interface, an echo is generated from the integration of currents induced on that interface [28], and the phase of this induced currents is affected by the interface RMS height and thus the integrated echoed power is affected by the RMS height. To estimate the roughness, the pulse compressed data without incoherent averaging and decimation are used to meet the high spatial sampling requirement.

3.1 Methods to estimate RMS height σ

The RMS height variations of an interface can be estimated from data statistics or modeled using various models with constraints on the scale of roughness.

3.1.1 Method using power statistics

When an aircraft moves at a constant distance over the air – firm interface, if the air – firm interface is rough, the echo amplitude variations are caused by variations in phase – resulting in a phenomenon called fading [29]. In case of a smooth, uniform interface a single scattering center is located at normal incidence and the echo amplitudes will not fade, but, in the case of a rough or non-uniform interface, there could be more than one independent scattering centers in the illuminated area causing amplitude fading due to interference between individual echo returns [23].

In Neal's method [30], the RMS height is obtained by using statistics of power variance σ_p and fading length x_f . The power variance is given by

$$\sigma_p = \frac{\langle P(x)P(x) \rangle}{\langle P(x) \rangle^2} - 1 \quad (3.1)$$

where x represents the along track position.

The fading length is defined as the distance over which the auto correlation function, $\rho_p(\mu)$, drop to the value of $1/e$

$$x_f = \mu |_{\rho_p(\mu)=1/e} \quad (3.2)$$

The autocorrelation function, $\rho_p(\mu)$, is given as

$$\rho_p(\mu) = \frac{\langle P(x)P(x+\mu) \rangle - \langle P(x) \rangle^2}{\langle P(x)P(x) \rangle - \langle P(x) \rangle^2} \quad (3.3)$$

The correlation length l is the distance at which the autocovariance function drops to $1/e$ of its initial value and it is the length beyond which the surface undulations become statistically independent.

Now using these calculated values, the phase shift ϕ and correlation length l are estimated using the theoretical model given by the two equations below:

$$\sigma_p = 2\phi^2 \left(\frac{1}{1+2\Gamma} - \frac{1}{1+R_F^2} \right) \quad (3.4)$$

$$\rho_p(\mu) = \frac{\left\{ e^{-\left(\frac{\mu}{l}\right)^2 \left[1 - \frac{2}{2+\Gamma} \right]} - \frac{1+2\Gamma}{1+R_F^2} e^{-\left(\frac{\mu}{l}\right)^2 \left(\frac{1}{1+R_F^2} \right)} \left[\cos \frac{\mu^2 R_F}{l^2 (1+R_F^2)} + R_F \sin \frac{\mu^2 R_F}{l^2 (1+R_F^2)} \right] \right\}}{\left(1 - \frac{1+2\Gamma}{1+R_F^2} \right)} \quad (3.5)$$

where R_F is the Fraunhofer region of the sounding geometry given by $R_F = \lambda \left(h + \frac{z}{n} \right) / (\pi l^2)$ and $\Gamma = \lambda^2 \left(h + \frac{z}{n} \right) / (4\pi^2 l^2 \tau)$ in which λ is the wavelength, z is the depth, h is the terrain clearance, n is the refractive index of ice and τ is the pulse length in terms of distance in air.

The best values of RMS height and correlation length are selected based on the minimum mean square error between the theoretically estimated values and those calculated from the data; the theoretical estimates of power variance and fading length are obtained by iteratively substituting phase variation values associated with the possible RMS values and the possible correlation length values in the theoretical model equations.

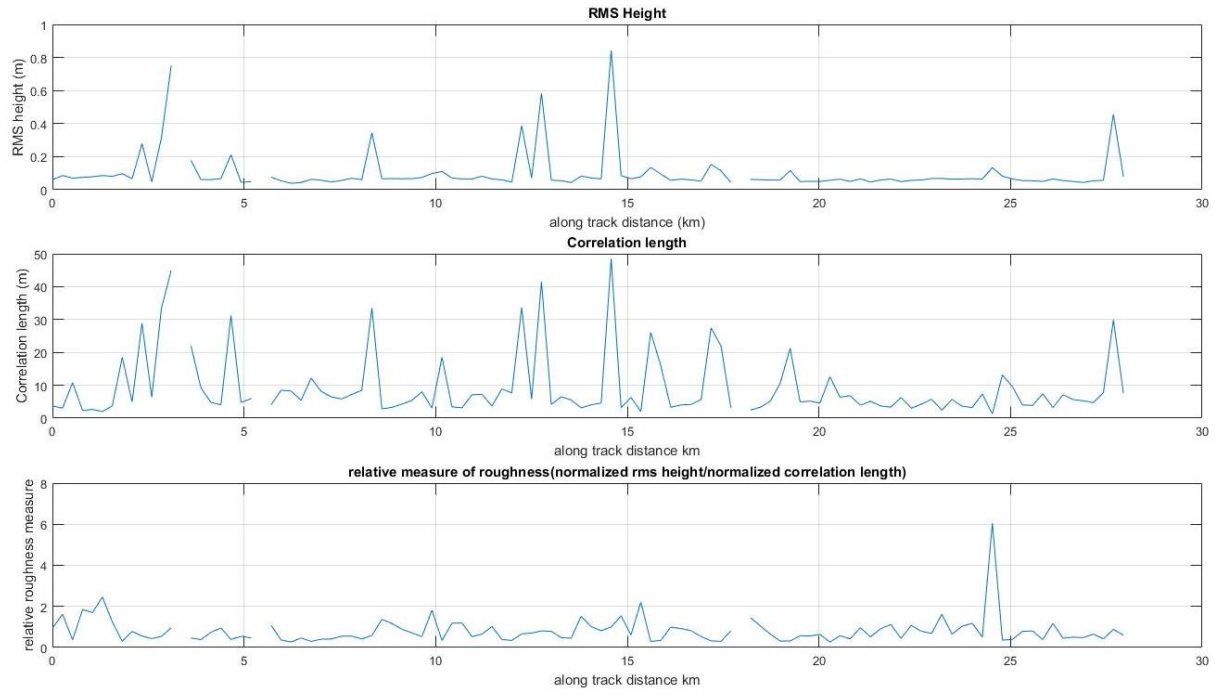


Figure 3.1 Estimated RMS height and correlation length for a smooth air – firn interface (20111213_05_009)

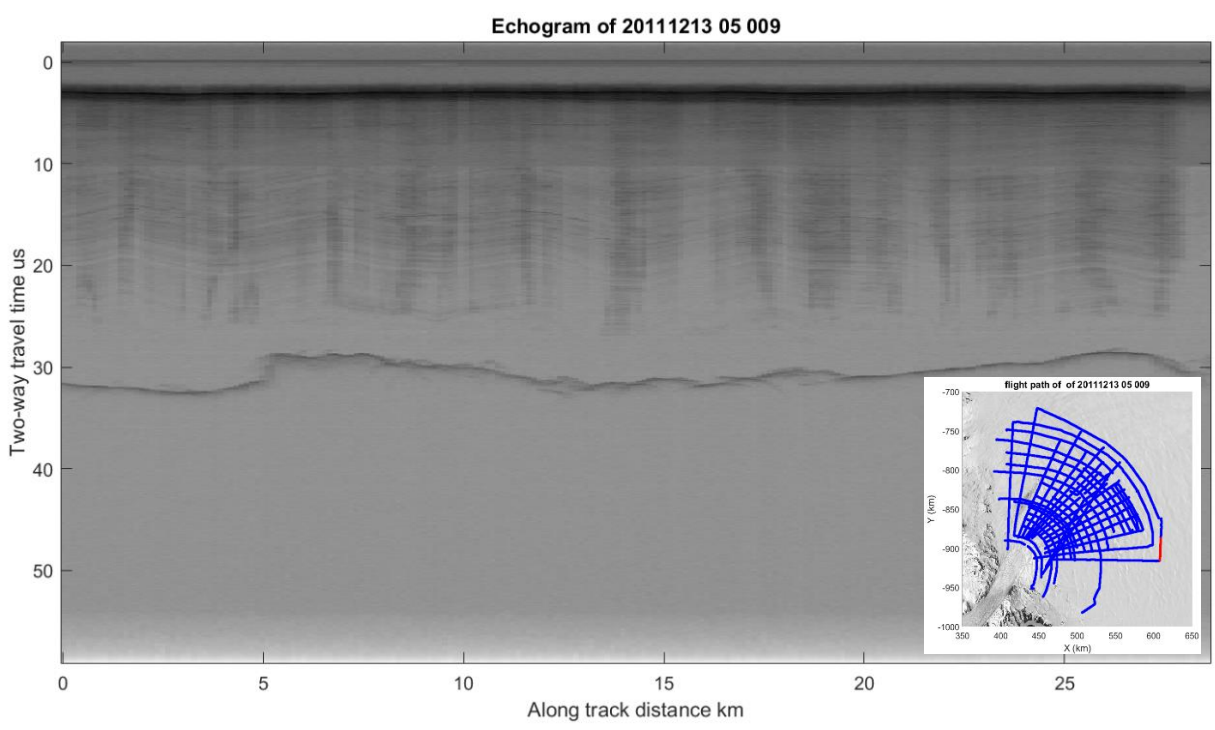


Figure 3.2 Echogram of a smooth air – firn interface (20111213_05_009) Bottom right image shows the corresponding flight line of the echogram

The results of this method, for a smooth air – firn interface of Byrd glacier data (20111213_05_009) [31] is shown in Figure 3.1.

The corresponding echogram with the flight path of the data frame 20111213_05_009 is shown in Figure 3.2. The echogram is the image obtained after the SAR processing of the data. The vertical axis of an echogram represents two-way propagation time of the wave and the horizontal axis represents the along track or azimuth direction. The color levels in the echogram represent the power received at the receiver.

According to Figure 3.1, most of the estimated RMS height values of air – firn interface for the data frame 20111213_05_009 are less than 6 cm. To get a sense of roughness, a relative roughness measure is calculated as the ratio of normalized RMS height to the normalized correlation length. This parameter will be high if the correlation length is small and RMS variation is high, i.e. the area is relatively more rough if the RMS height varies largely in short correlation lengths and vice-versa.

This model is valid only for $\phi^2 < 0.3$ but this is not always the case for air – firn interface roughness of the ice sheets

For a relatively rough air – firn interface of Byrd glacier data (20111212_01_002) [31], the estimated roughness parameters are shown in Figure 3.3.

For this data frame 20111212_01_002, the estimated RMS height variations are more than 10cm and at most of the locations this method could not estimate the RMS height because it exceeds the limit beyond which this method is no longer valid. The echogram with the corresponding flight path for this data frame is shown in Figure 3.4

The correlation between the locations with high estimated roughness values and the locations with ice surface scattering in the echogram of Figure 3.4, shown in dark gray color, can also be observed from the results.

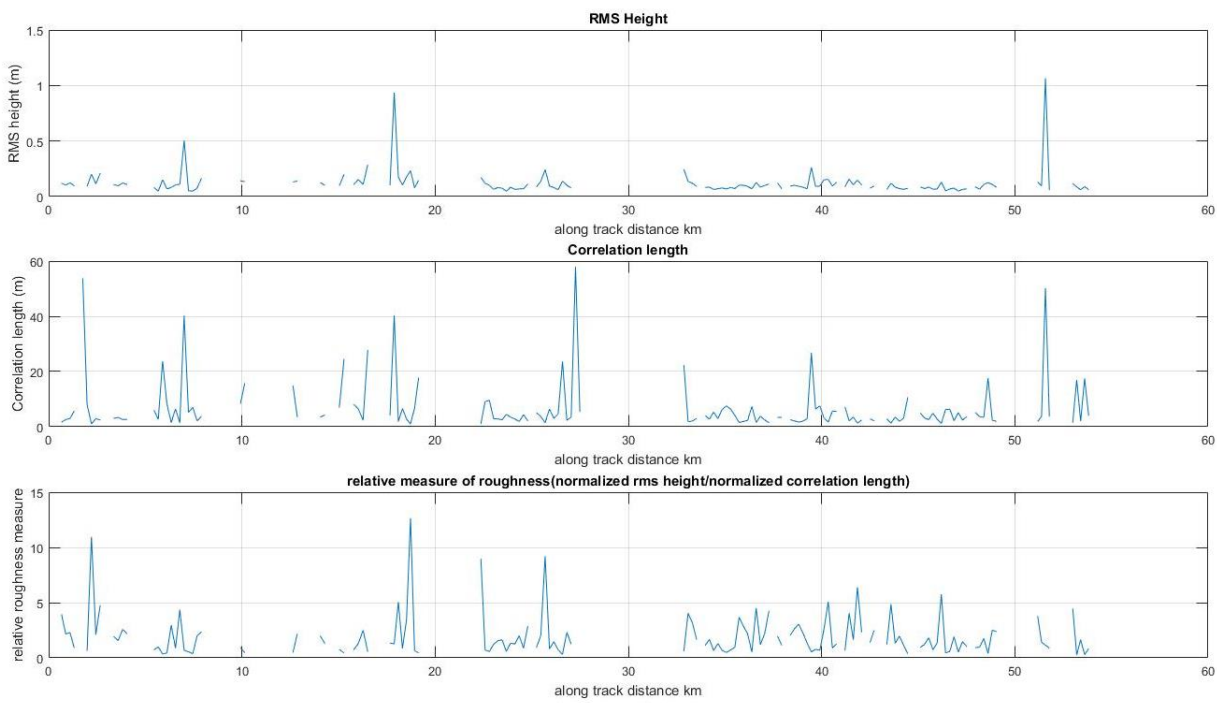


Figure 3.3 Estimated RMS height and correlation length of a relatively rough air – firm interface

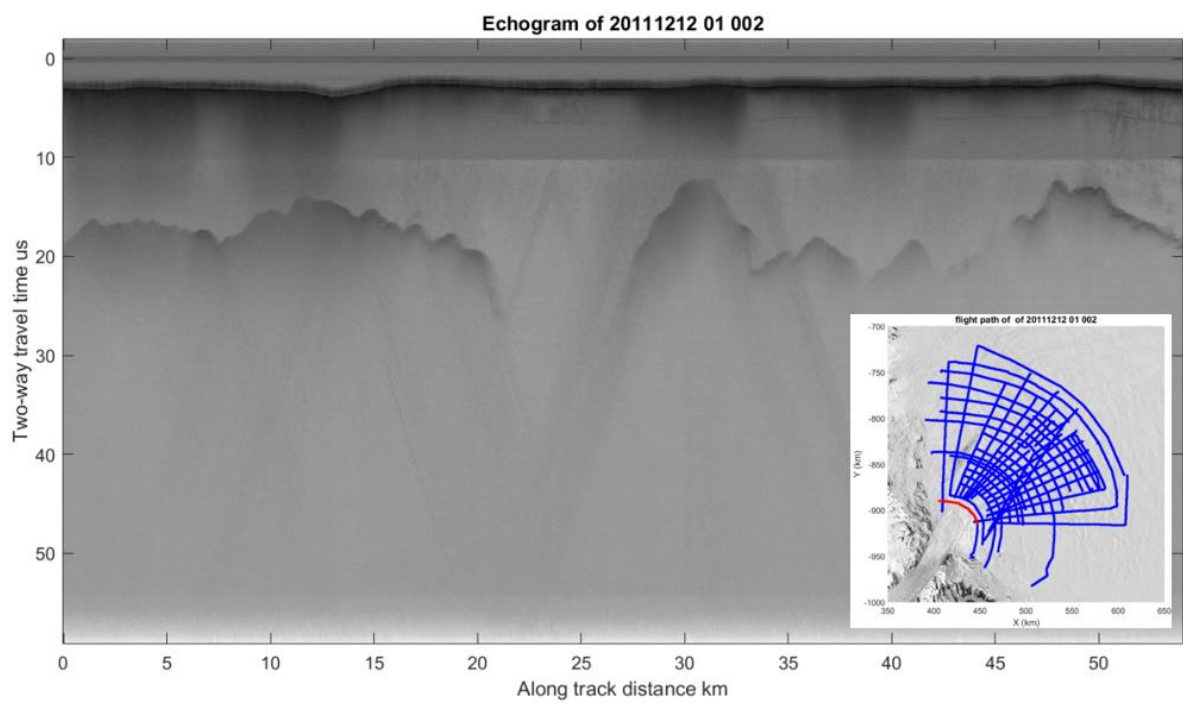


Figure 3.4 Echogram and flight path of a relatively rough air – firm interface (20111212_01_002) Bottom-right image shows the corresponding flight line of the echogram

3.1.2 Method using waveforms

The received echo signal can be modeled [32] as the multiple convolution of radar point target $P_{PTR}(t)$, flat surface impulse response $P_{FSIR}(t)$ and surface height density function $P_{pdf}(t)$, mathematically given as

$$P(t) = P_{PTR}(t) * P_{FSIR}(t) * P_{pdf} \quad (3.6)$$

In this model, $P_{PTR}(t)$ is approximated by the natural specular reflections in the data. The specular reflections for the ice – bed interface of Byrd glacier are calculated using abruptness index and are shown in Figure 3.5. Abruptness index [33] is given as

$$I_{abr}(x) = \frac{P_{peak}(x)}{P_{ag}(x)} \quad (3.7)$$

where $P_{peak}(x)$ is the peak power of the received signal echo and $P_{ag}(x)$ is the aggregate power of the received bed echo over the depth interval. For all the abruptness calculated locations SNR of $P_{peak}(x)$ is greater than 5dB.

We can choose a Gaussian function as the probability density function $P_{pdf}(t)$ or other function based on knowledge about the surface, if available for those locations. $P_{FSIR}(t)$ is the average backscattered power from a mean flat rough surface with the same backscattering cross section per unit scattering area as the true surface:

$$P_{FSIR}(t) = \frac{P_t \lambda^2}{(4\pi)^3} \int_{illuminated\ area} \frac{\delta(t-t_d) G_t(\theta, \psi) G_r(\theta, \psi) \sigma_o(\theta, \psi)}{r^4} dA \quad (3.8)$$

where r is the distance from the antenna to the elemental scatter at elevation and azimuth angles θ and ψ , δ is the Dirac delta function, t_d is the two-way propagation time, $G_t(\theta, \psi)$ and $G_r(\theta, \psi)$ are the transmit and receive antenna gains and $\sigma_o(\theta, \psi)$ is the unit backscattering cross section.

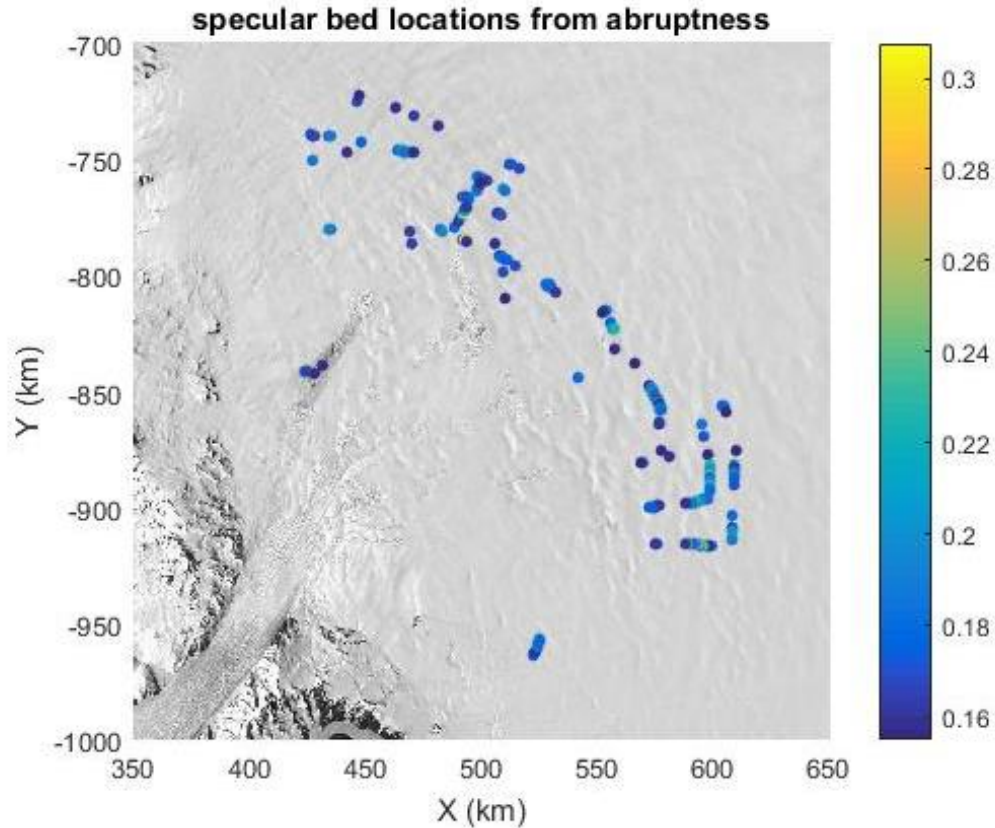


Figure 3.5 Specular reflections of Byrd Glacier ice – bed interface

An example of smooth and relatively rough bed echoes from the flight line 20111212_01_017 is shown in Figure 3.6.

In the case of specular reflections, leading and trailing edges of the echoes can be differentiated by using the only peak of the reflected echo. But in the case of rough echoes, there could be multiple peaks and the first peak might not be the highest of the peaks. In these cases, the way the trailing edge and leading edge are defined, will affect the roughness estimation.

In general, the magnitude of the echoes at the ice – bed interface are proportional to the dielectric contrast at the interface and the width of the peak in the echoes are proportional to the roughness at the interface. But the same echo shapes can be obtained for various bed and ice conditions [34]. For example, the geometry of the bed could also affect the magnitude of the peak.

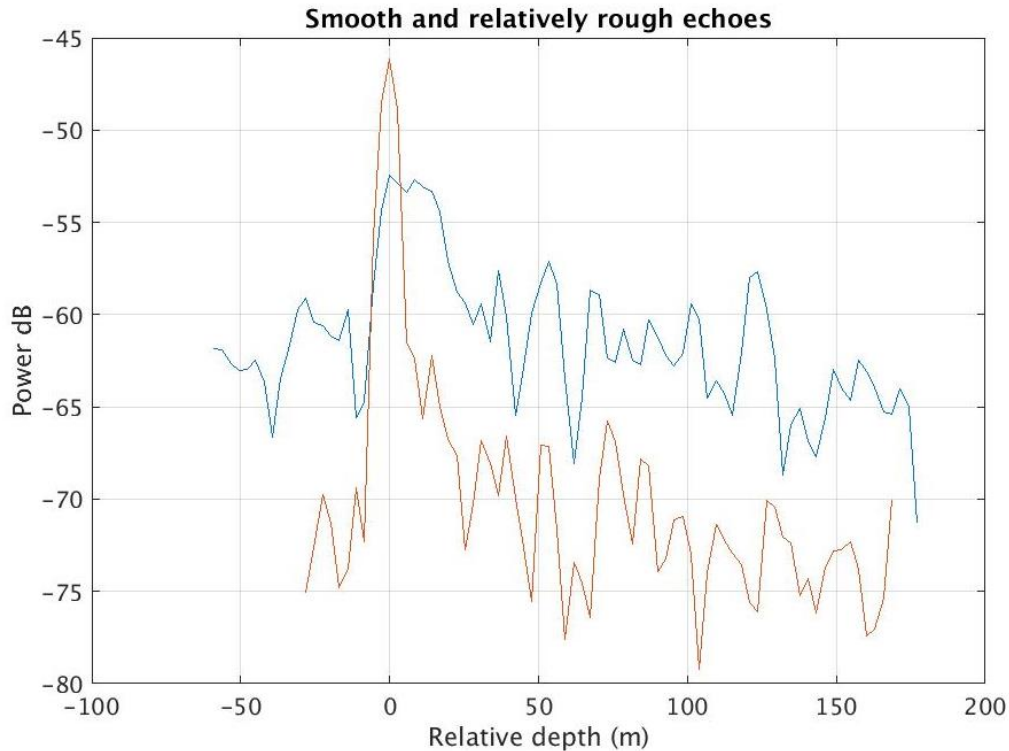


Figure 3.6 Bed echoes of smooth and relatively rough interfaces.

3.1.3 Method using amplitude distribution model

Following the method given in [35], the receive signal at the antenna is the summation of backscattered radiation consisting of coherent (or deterministic) component and diffused (or random) component. If the surface interface is specular the backscattered radiation is dominated by the coherent component with a negligible incoherent component. In case of rough surfaces, the received backscattered radiation is dominated by incoherent component. This is shown in Figure 3.7 and in Figure 3.8 using the distribution of received amplitude values for about 200m of along track bin from a smooth and relatively rough surface locations

The amplitude variations across the radar resolution cells can be caused due to a change in the subglacial materials with high to low reflection coefficient values or due to multiple interfering scattering centers within each cell [23]. The echograms at these locations can be observed to reduce the ambiguity.

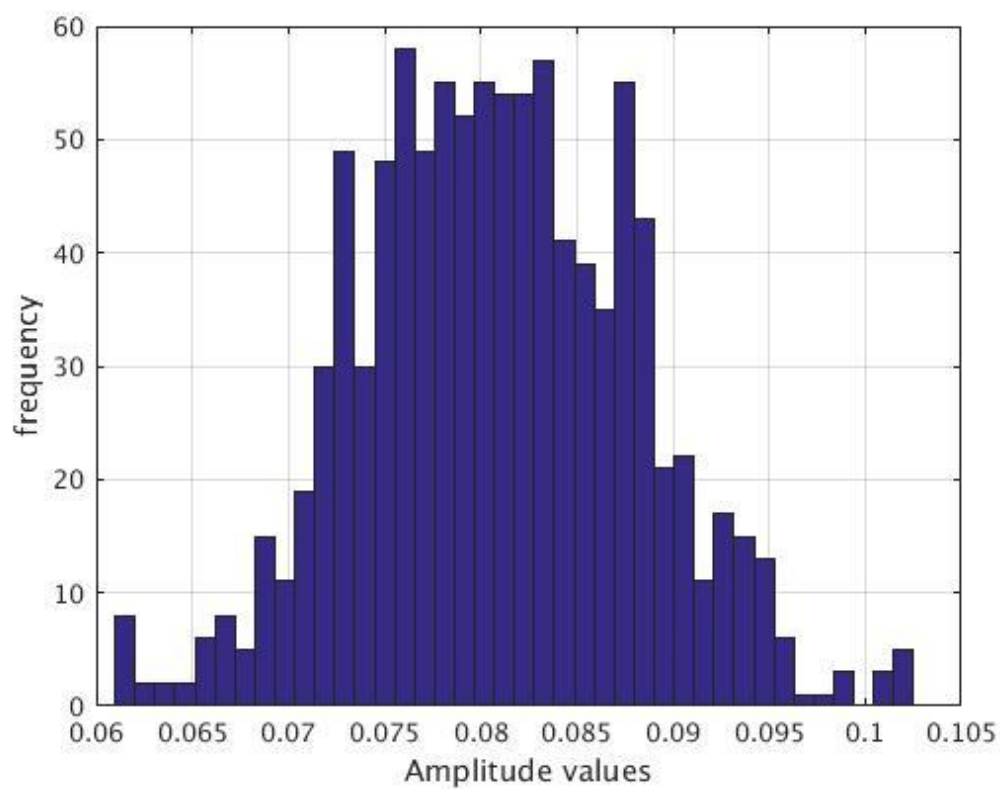


Figure 3.7 Distribution of the returned echoes amplitude values from a smooth air – firn interface location

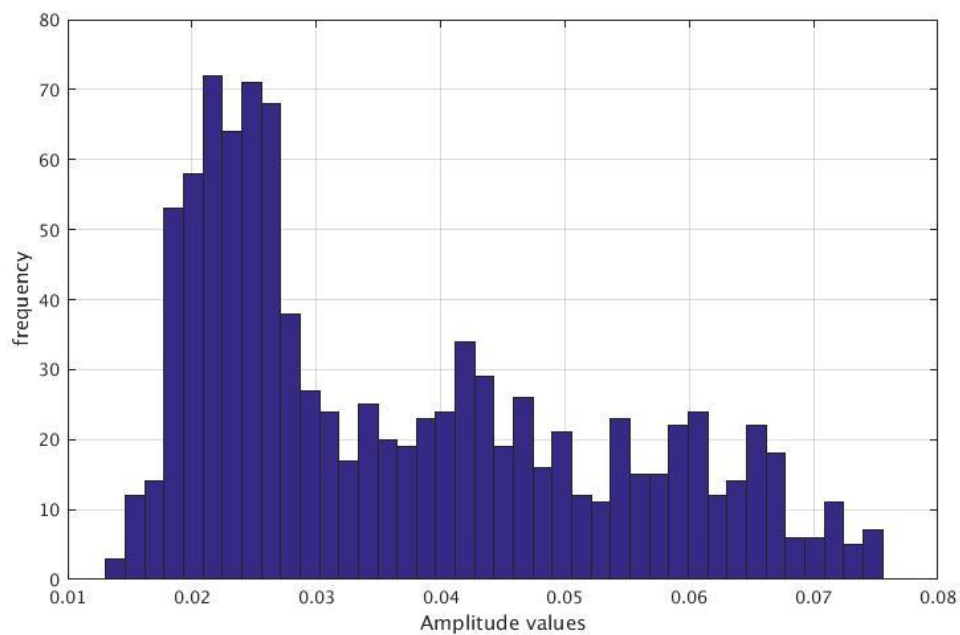


Figure 3.8 Distribution of amplitude values of returned echoes from a rough air – firn interface location

The amplitude distribution of received echoes with both reflected and scattering components can be approximated by a rice distribution to estimate the coherent and incoherent components of the received power. As the coherent component decreases, the rice distribution approaches to Rayleigh distribution [23]; this can also be observed from above histograms.

The echo returns from the air – firm interface for the complete Byrd glacier is grouped into chunks of about 200 m each, over along-track distance, and a rice distribution is fitted to the amplitude values of each chunk of echo returns. Using the parameters obtained by fitting the distribution, coherent and incoherent components of the air – firm interface are estimated for the 200-m along-track distance.

Theoretically, the Coherent power component is given by

$$P_c = R_s^2 \exp(-(2k\sigma_h)^2) \quad (3.9)$$

where R_s is the Fresnel coefficient of air-firm interface, k is the wavenumber given as $k = \frac{2\pi}{\lambda}$ and σ_h is the RMS vertical height. The Incoherent component is given by

$$P_n = 4k^2 R_s^2 \sigma_h^2 \operatorname{erf}\left(\frac{\pi l_x}{2L_s}\right) \operatorname{erf}\left(k l_y \sqrt{\frac{c}{h\Delta f}}\right) \quad (3.10)$$

where l_x and l_y are correlation lengths in x and y directions, L_s is the synthetic aperture length, h is the range to the ice sheet surface, Δf is the signal bandwidth. For a given footprint dimension, a threshold exists beyond which correlation length can be neglected and for the correlation length greater than threshold $\operatorname{erf}(x) \approx 1$. The RMS height value can be estimated by fitting a value to the ratio of the obtained coherent and incoherent components, by minimizing the mean square error, using the below equation

$$\frac{P_c}{P_n} = \exp(-(2k\sigma_h)^2) [4k^2 \sigma_h^2]^{-1} \quad (3.11)$$

The RMS height of air – firm interface calculated using this method for the flight paths 20111213_05_009 and 20111212_01_002 are shown below in Figure 3.9 and Figure 3.10.

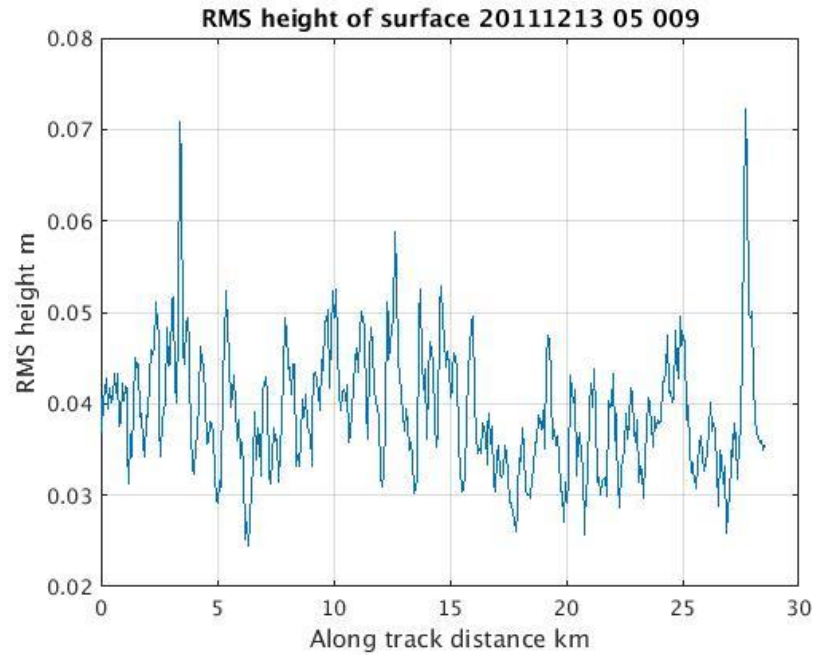


Figure 3.9 RMS height of smooth air – firm interface (20111213_05_009)

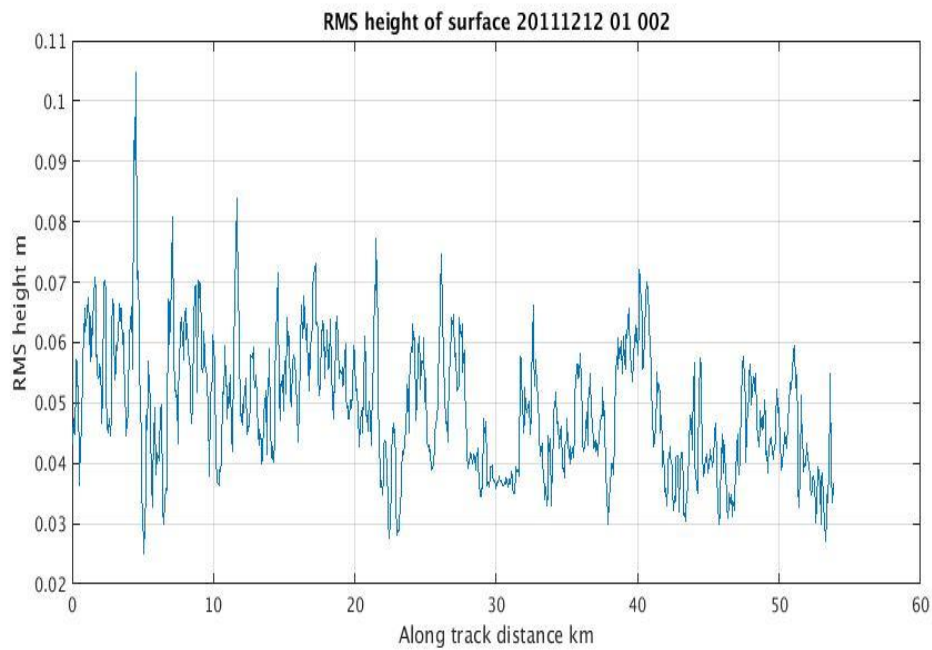


Figure 3.10 RMS height of relatively rough air – firm interface (20111212_01_002)

Comparing these results with those obtained using Neal's method, we see that both methods agree on the relative roughness of the data sets. The comparisons between the results using these two methods are shown below in Figure 3.11 and Figure 3.12.

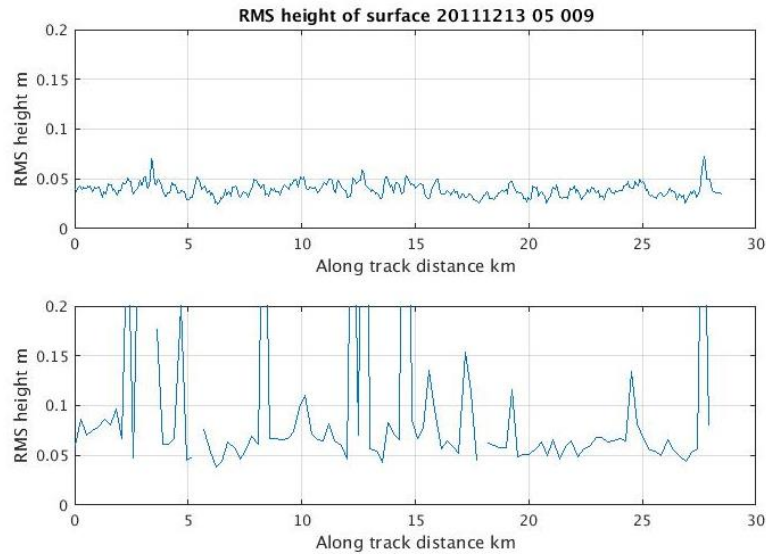


Figure 3.11 Roughness estimates for data frame 20111213_05_009, top plot represents estimated roughness using amplitude distribution method and bottom plot represents estimated roughness using Neal's method

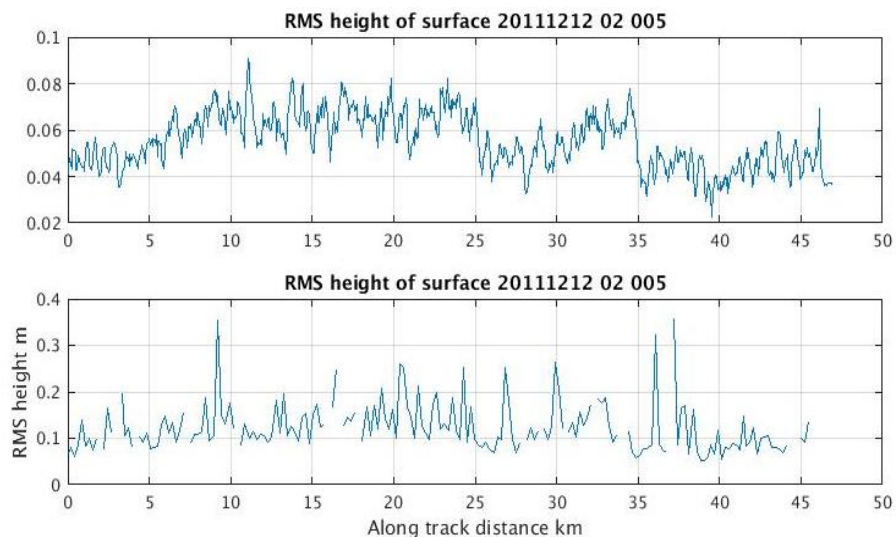


Figure 3.12 Roughness estimates for data frame 20111212_02_005 – top plot represents estimated roughness using amplitude distribution model method – bottom plot represents estimated roughness using Neal's method

On comparison, the roughness estimates from the Neal's method seem to be at a higher scale than the estimated roughness values from the amplitude distribution model, at the relatively rough locations. At relatively smooth locations, the roughness estimates from both methods agree closely and the locations with high estimated roughness values correlate with high surface scattering locations in echograms.

The map of air – firn interface roughness obtained using the amplitude distribution model method, for the complete Byrd glacier is shown below in Figure 3.13.

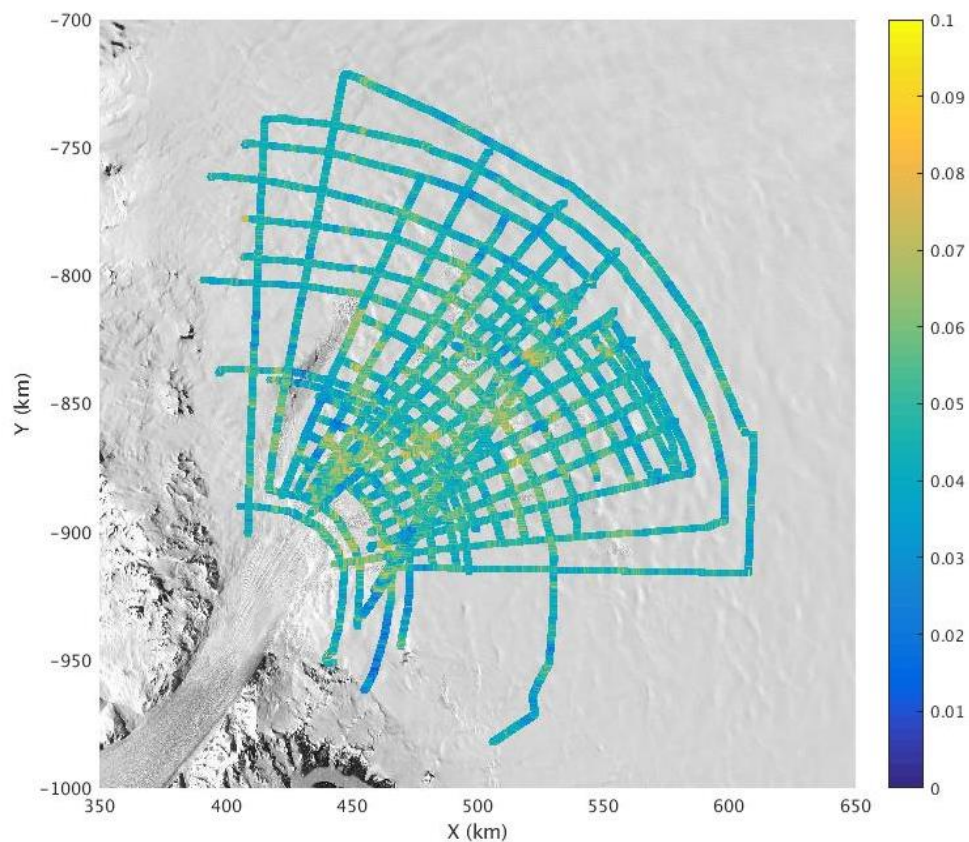


Figure 3.13 Air – firn interface roughness map

In the map above, the scale of roughness is color coded. It is observed the relatively high roughness occur at the trunk of the glacier where the glacier converges into the trunk and crevasses present. The

locations with relatively high roughness values correlate with the speckle pattern in the background LANDSAT LIMA image. This is shown in the Figure 3.14.

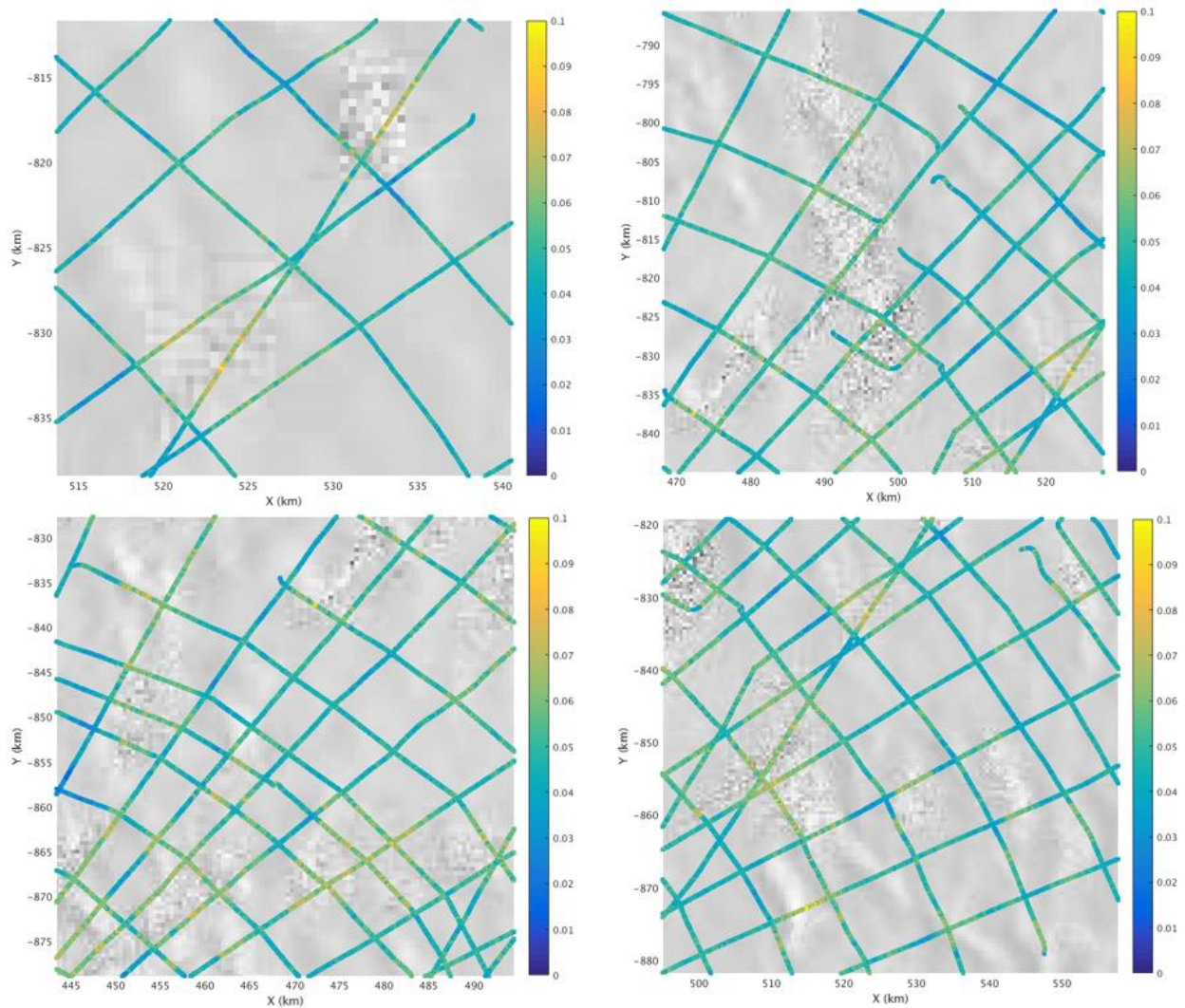


Figure 3.14 Scaled images of estimated air – firn interface roughness map

Assuming the phase difference in the echoes returned from the ice – bed interface is caused only by the RMS variations of air – firn interface, the phase variation in the reflected echo from the ice – bed interface is calculated by

$$\phi = \frac{4\pi\sigma}{\lambda} (\sqrt{\epsilon} - 1) \quad (3.12)$$

where σ is the RMS variations of air – firm interface [36]. The dielectric constant values in the above equation are estimated from the equation (3.9) of the coherent component using the estimated RMS height. The power reduction caused by this phase variation is calculated and compensated using the equation 2.3.

Similarly the rice distribution is fitted for the echoes from the ice – bed interface, for about every 200m along track distance and the roughness of the ice – bed interface is estimated. The corresponding ice – bed interface roughness map is shown below Figure 3.15.

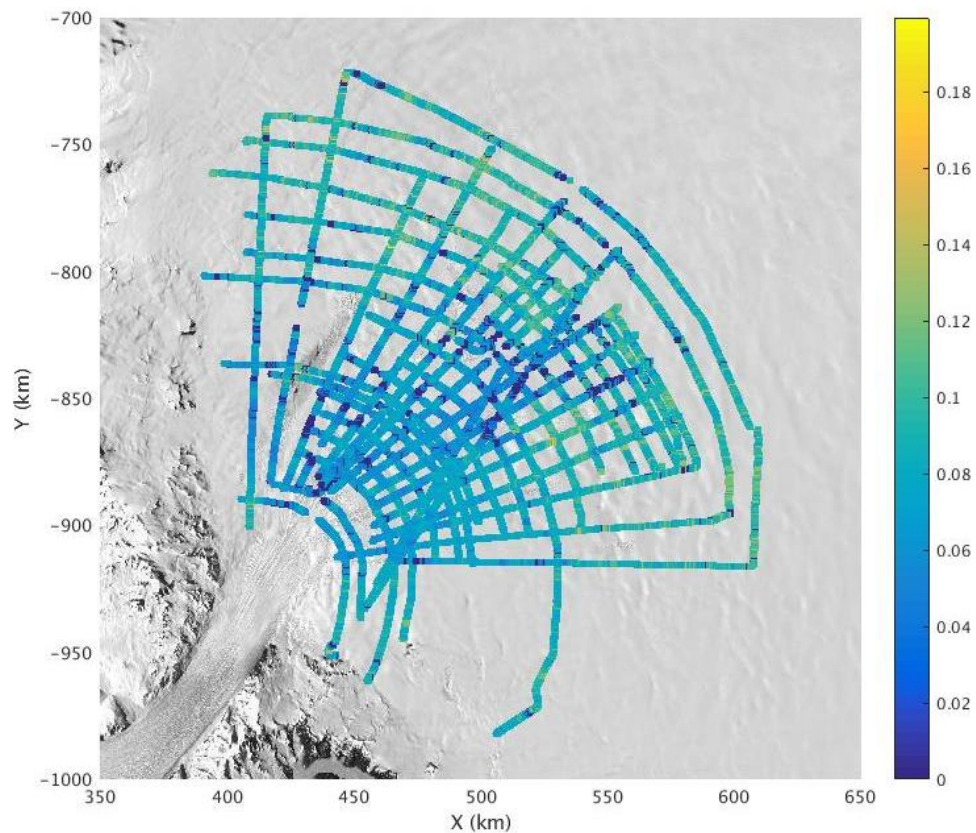


Figure 3.15 Ice – bed interface roughness

From the map above, the ice – bed interface roughness is relatively more than the estimated roughness at air – firm interface.

The phase variations in ice – bed interface returns due to the RMS height variations of the ice – bed interface are calculated by [36]

$$\phi = \frac{4\pi\sigma}{\lambda} \sqrt{\epsilon} \quad (3.13)$$

In this case, the dielectric constant of ice is assumed as 3.15 and the corresponding power reduction caused by this phase variation is calculated and compensated using the equation 2.3.

The following Figure 3.16 shows the InSAR-based velocity map of Antarctica in the Byrd Glacier region [37]

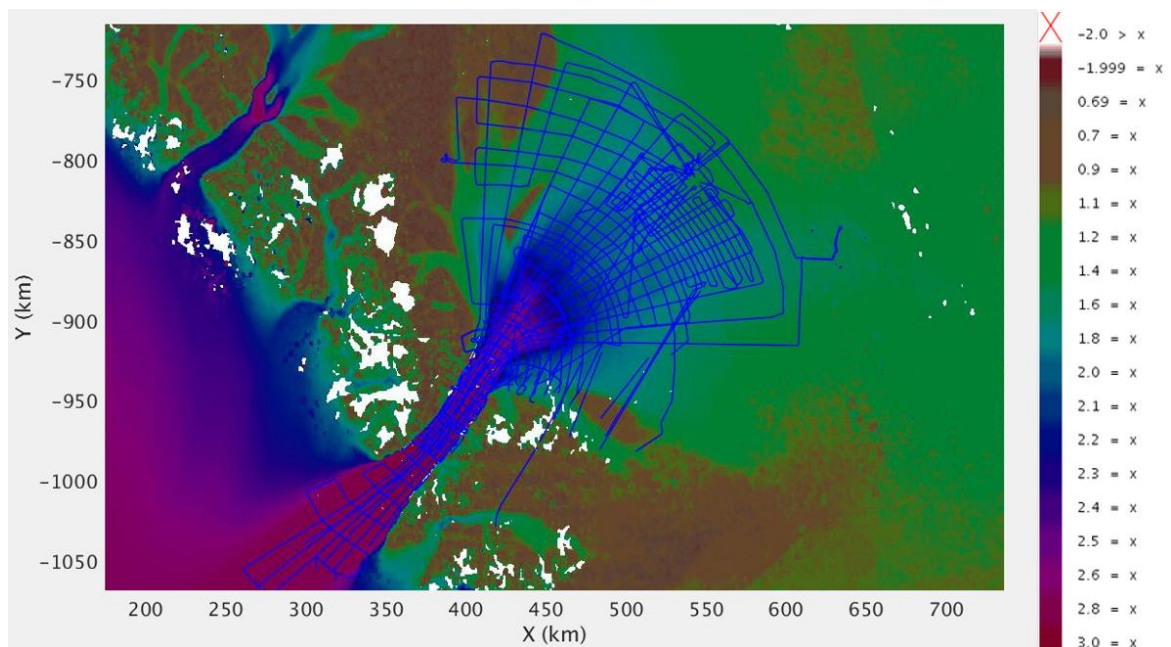


Figure 3.16 InSAR-based velocity map of Antarctica colorbar represents the velocity magnitude in km/yr

From the Figure 3.16 and Figure 3.13, higher velocity magnitudes can be observed at the trunk of the Byrd Glacier and the high estimated air-firn interface roughness values at these locations could be a result of different ice velocity rates near the trunk of the glacier.

From Figure 3.16 and Figure 3.15, lower estimated ice-bed interface roughness values can be observed in the areas of high velocity rates.

Chapter 4 Estimation of Ice attenuation

Once the power reduction due to roughness has been accounted, the reflectivity values can be estimated from the received power if the englacial attenuation is known. Englacial attenuation is given by

$$[L]_{dB} = 2N_a z \quad (4.1)$$

where z is the ice depth and N_a is the englacial attenuation rate dB/km.

4.1 Previous methods

The englacial attenuation rate can be determined by the ice core data or by growing pure ice in a lab for different impurity concentrations, pressure and temperature profiles, but it cannot be applied over complete glacier due to spatial variability.

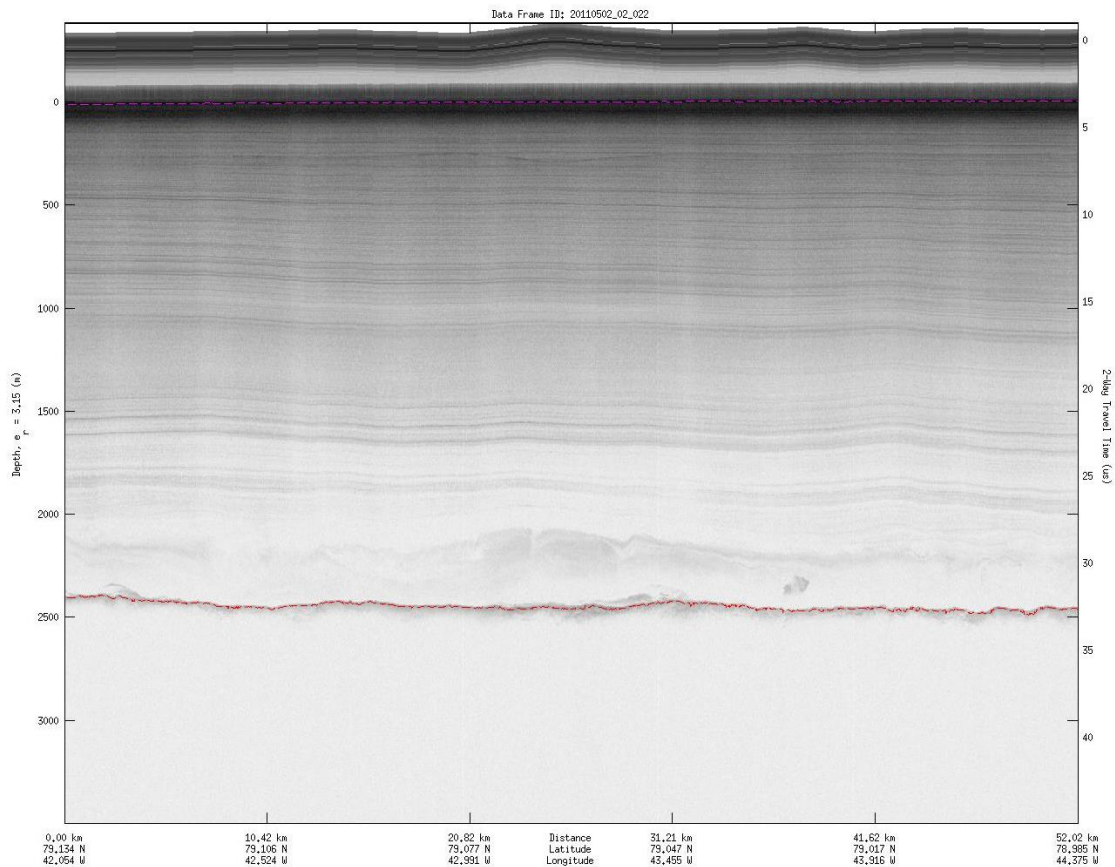


Figure 4.1 Echogram of Greenland 20110502_02_002 data frame

The power reflected at the internal layers of the ice sheet could be used for estimation of englacial attenuation, but the picking of internal layers for the Byrd glacier is much time taking. As the internal layers of Byrd glacier are not very distinct and separated as those of Greenland. An example of internal layers of Greenland and Antarctica is shown in Figure 4.1 and Figure 4.2.

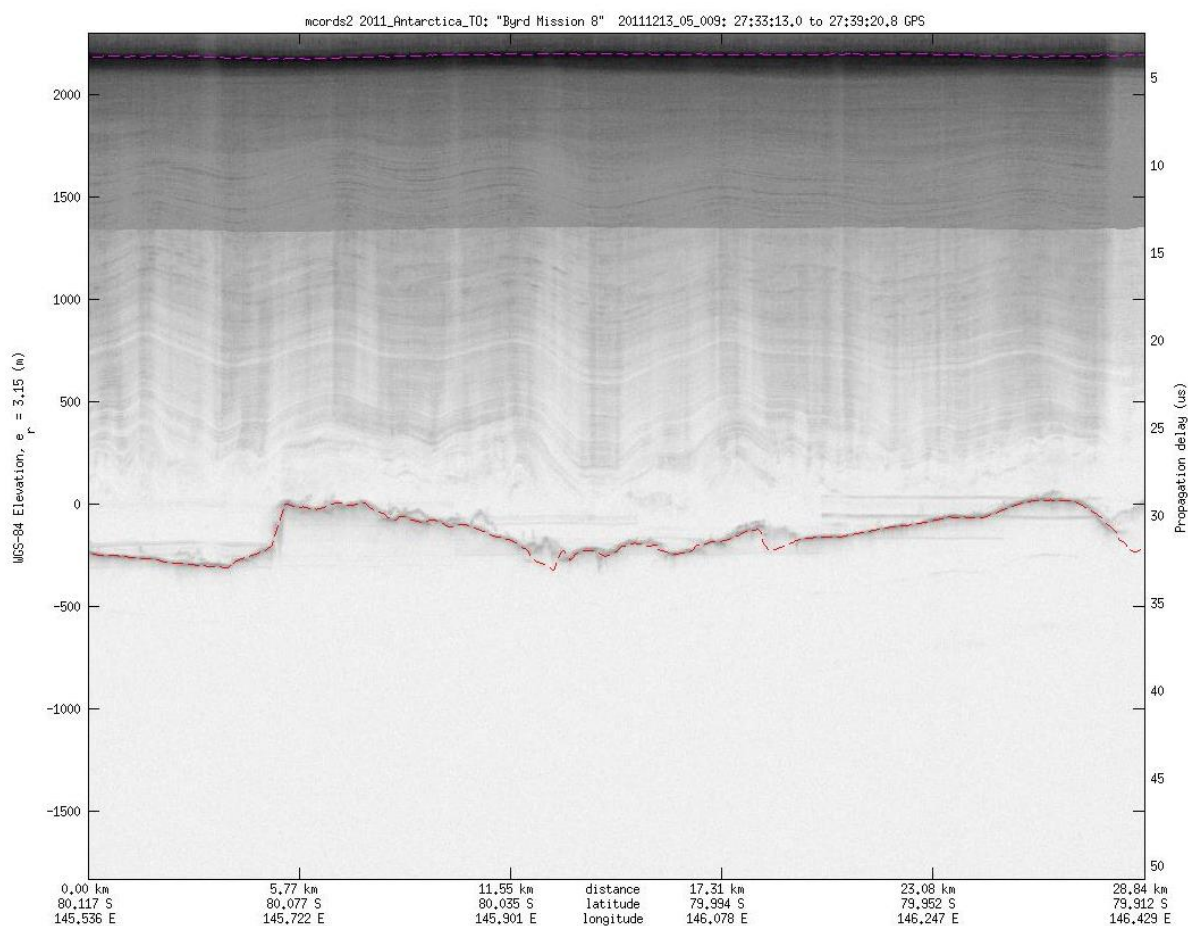


Figure 4.2 Echogram of 20111213_05_009 data frame, Byrd Glacier

If this method is chosen, it cannot be applied over the complete glacier because, in few areas of the ice sheet, the internal layers might just be very low in number or even be none as shown below in Figure 4.3.

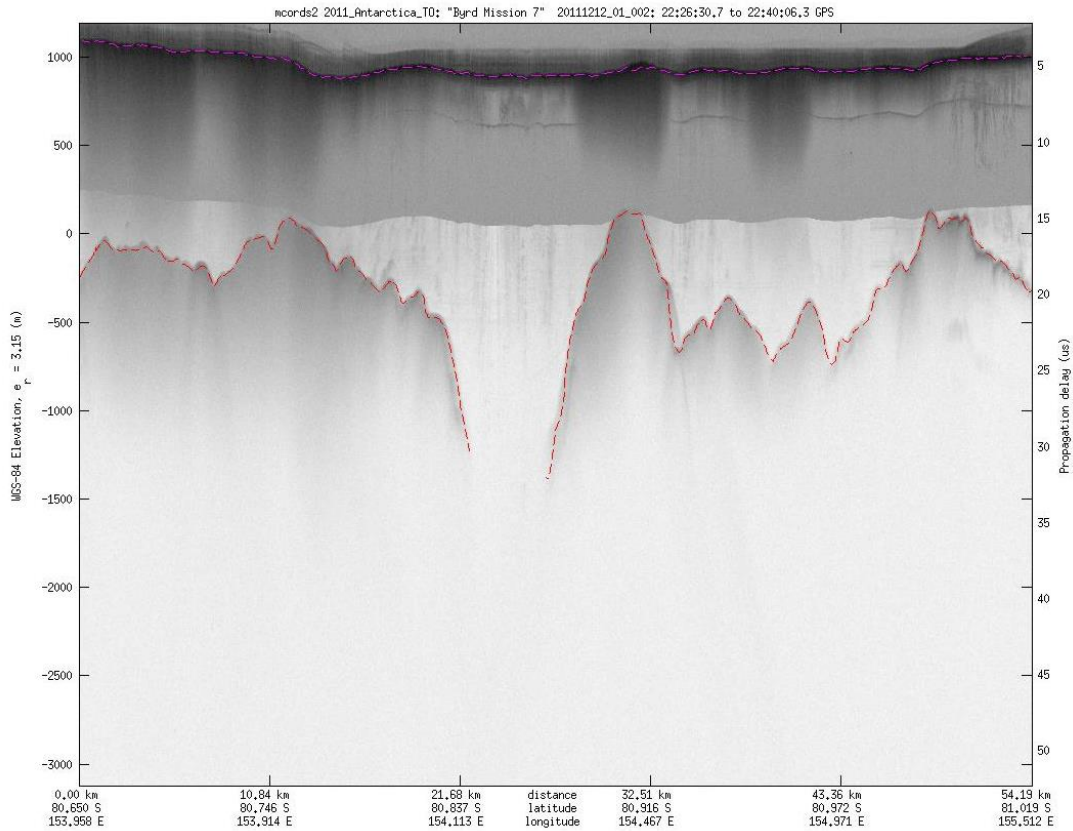


Figure 4.3 Echogram of 20111212_01_002 data frame of Byrd Glacier

The other methods to estimate englacial attenuation include a method assuming a constant englacial attenuation rate for the complete dataset to infer basal conditions from the radar data [38].

From the chapter 2, the geometrically corrected bed-echo power P^c is given by

$$[P^c]_{dB} = [S]_{dB} + [R]_{dB} - [L]_{dB} \quad (4.2)$$

Assuming $[S]_{dB}$ is constant along a flight line, the relative geometrically corrected bed-echo power P_r^c and relative englacial attenuation $[L - \bar{L}]_{dB}$ are given by

$$[P_r^c]_{dB} = [P^c - \bar{P}^c]_{dB} = [R - \bar{R}]_{dB} - [L - \bar{L}]_{dB} \quad (4.3)$$

$$[L - \bar{L}]_{dB} = 2 N_a (z - \bar{z}) \quad (4.4)$$

where \bar{z} is the average ice depth.

Assuming a constant attenuation rate N_a , enables to estimate the value of $[L - \bar{L}]_{dB}$ which in turns enables to estimate the relative reflectivity $[R - \bar{R}]_{dB}$. These relative reflectivity values can then be used to estimate the basal conditions.

But different values of N_a gives different sets of relative reflectivity values Figure 4.4 shows the relative reflectivity maps for N_a values of 5, 10, 15 and 25 along with the previously suspected subglacial lake locations based on elevation changes [14].

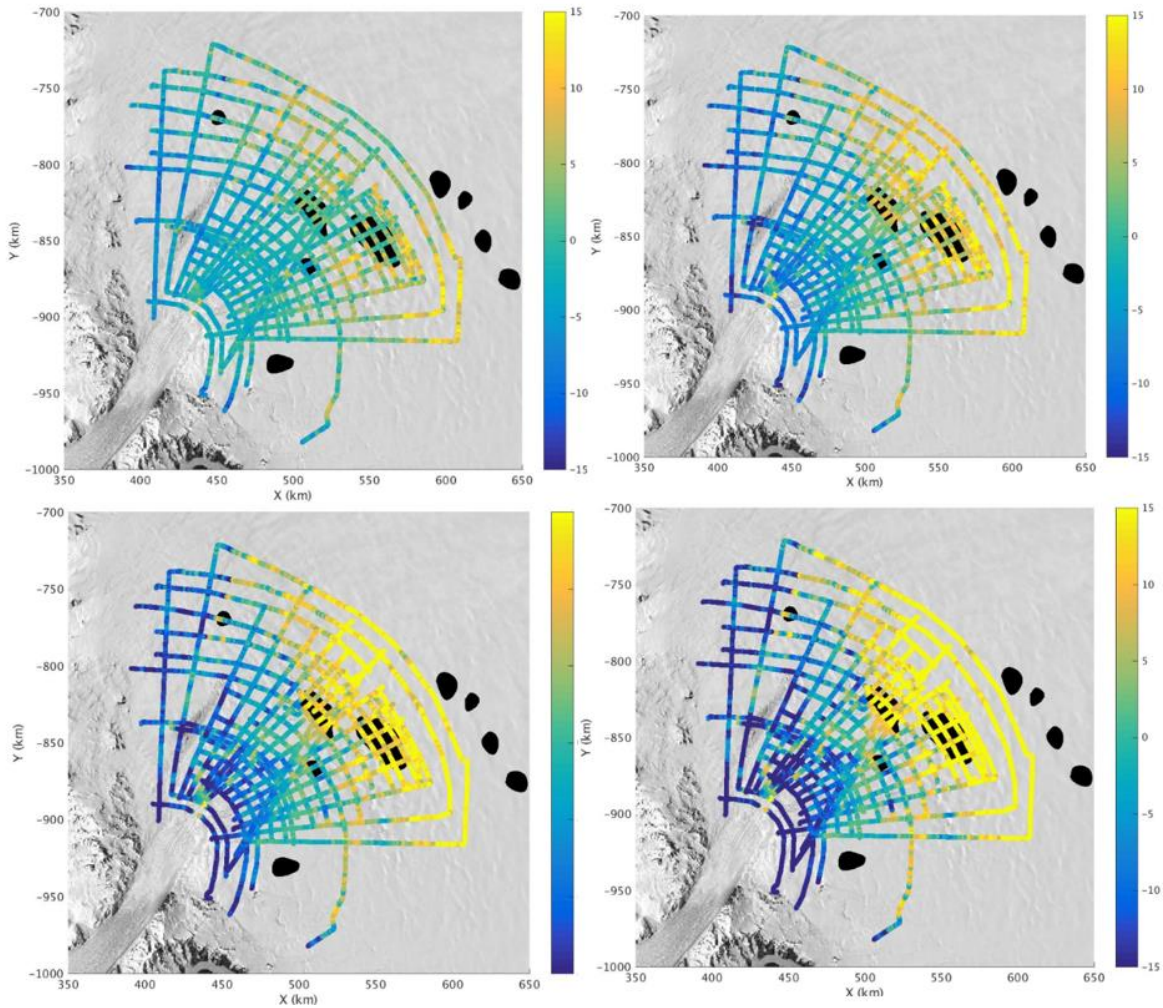


Figure 4.4 Relative reflectivity map for $N_a = 5$ dB/km (top left), $N_a = 10$ dB/km (top right), $N_a = 15$ dB/km (bottom left) and $N_a = 20$ dB/km (bottom right)

The color bar of the above figures is scaled from -15 to 15dB, but the obtained range of relative reflectivity values is physically unrealistic. This suggests for a better method to calculate enoglacial attenuation. This assumption of constant enoglacial attenuation for a complete dataset does not consider the spatial variations in attenuation rate, as discussed before the enoglacial attenuation varies spatially.

The relative enoglacial attenuation map for complete glacier using a constant enoglacial attenuation rate is shown below in Figure 4.5.

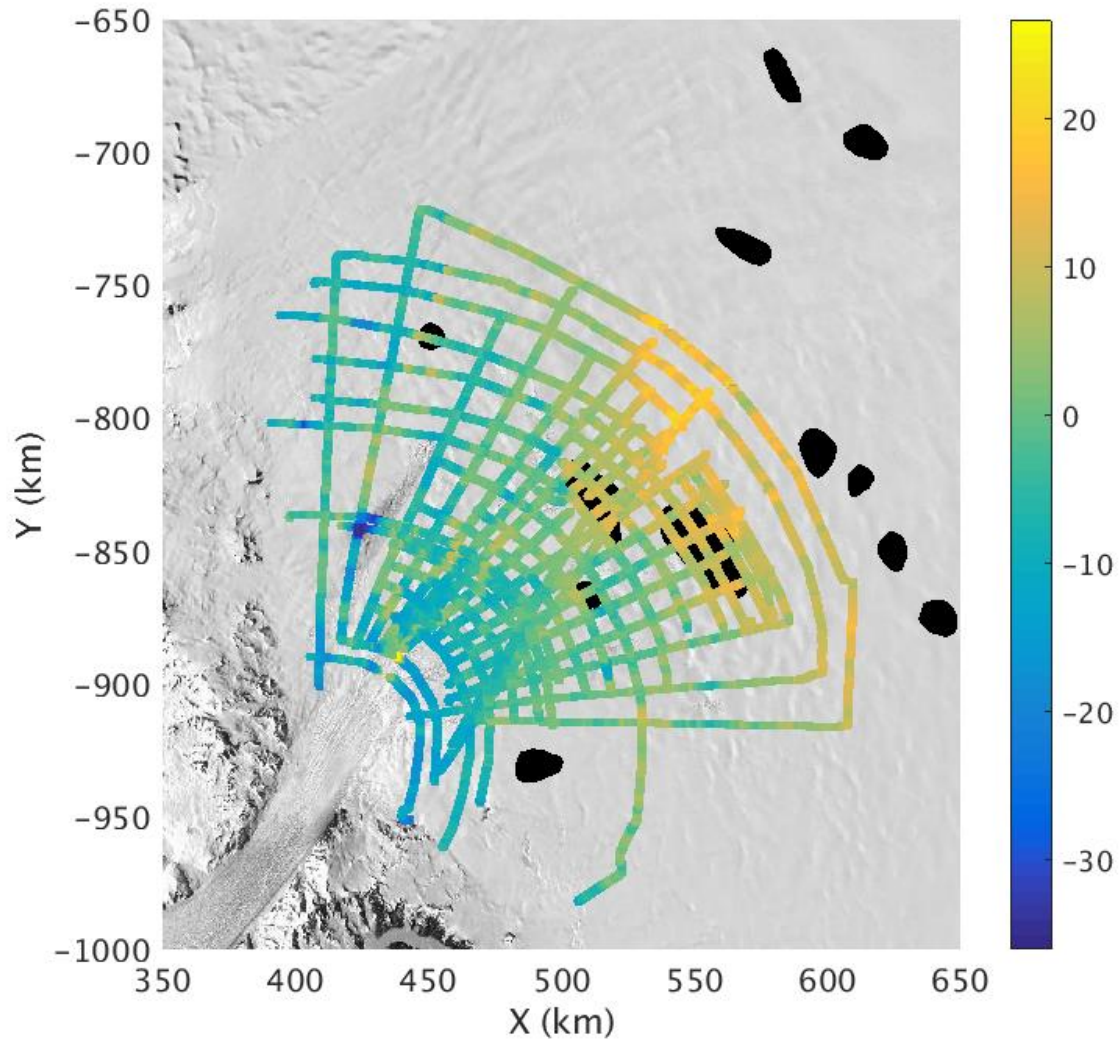


Figure 4.5 Relative englacial attenuation (dB) using a 10 dB/km englacial attenuation rate

In the case of regions where ice transitions from grounded ice sheet to freely floating ice shelf, and in regions with high air-firn interface roughness values, the assumption of a constant englacial attenuation can produce unrealistic basal reflectivity values [23]. In the case of the complete Byrd Glacier data set, the relationship between power (after correcting the geometric spreading loss) and depth is clearly not linear for all depths, as shown in Figure 4.6 below.

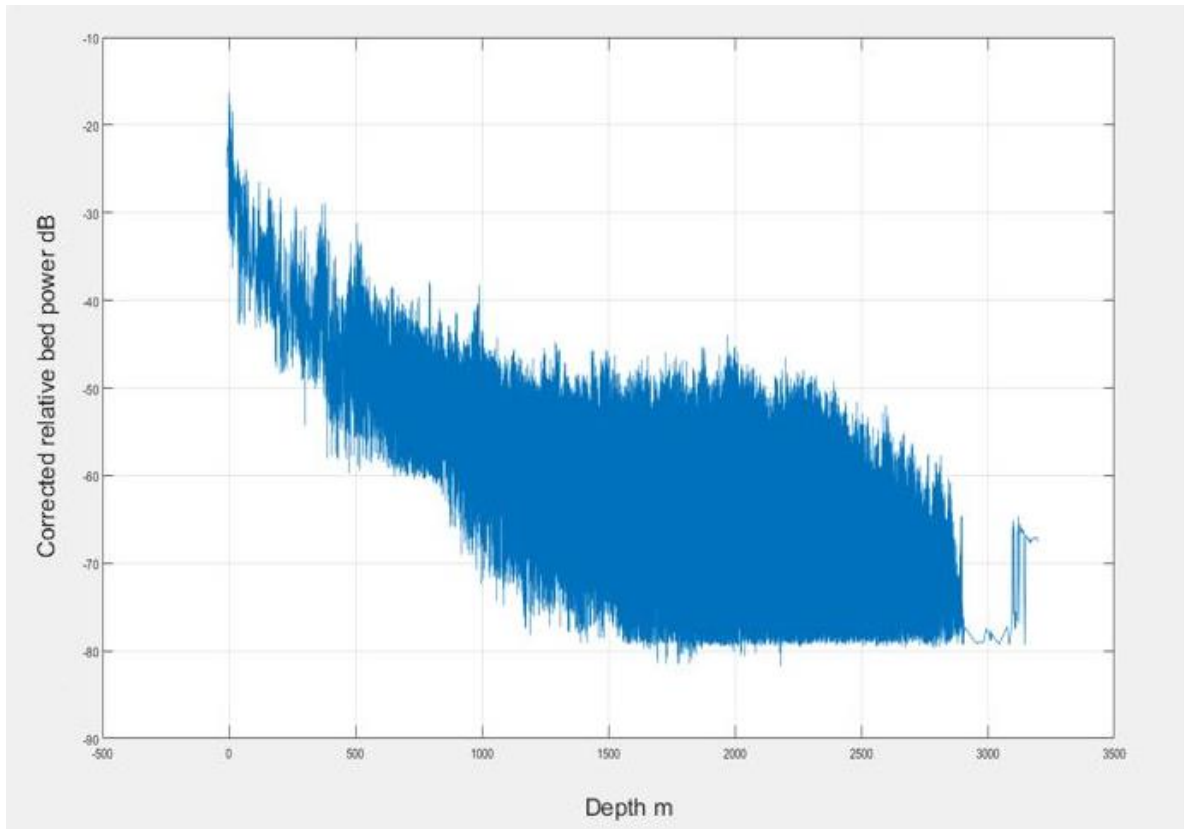


Figure 4.6 Need for spatially variable attenuation rate

From the above figure, the power seems to be much attenuated at a higher rate for the depths near the ice sheet surface than for those depths near the ice – bed interface. To infer basal conditions in these regions the englacial attenuation rate is modified [36].

4.2 Modified englacial attenuation

To account for spatially variable englacial attenuation rate, the modified attenuation rate is given as

$$N_a = \overline{N_a} + \frac{\partial N_a}{\partial x} (x - \bar{x}) \quad (4.5)$$

where $\overline{N_a}$ is the average attenuation rate, x is the along track position, \bar{x} is the mean position, and $\frac{\partial N_a}{\partial x}$ is the along track derivative of the attenuation rate [36].

In equation 4.3, if the reflectivity values are considered as a constant, then $[-P_r^c]_{dB}$ is the required apparent attenuation (caused due to two-way propagation of EM wave through the ice-column) to produce observed geometrically corrected relative bed-echo power signal. $\overline{N_a}$ is estimated for the complete data set, by assuming the bed reflectivity as a constant, smoothing the small-scale variations in $[R]_{dB}$ while retaining along track variations in N_a and $\frac{\partial N_a}{\partial x}$ is estimated for each flight line.

The improved relative reflectivity is given by,

$$[R_r]_{dB} = [P_r^c]_{dB} + 2 \left(\frac{\partial N_a}{\partial x} \right) (x - \bar{x}) \{z - \bar{z}\}_{l2} + 2\overline{N_a} \{z - \bar{z}\}_{l2} \quad (4.6)$$

In the above equation, $l2 = 100 \text{ m}$ is the filter length used to reduce the variations.

The estimated relative englacial attenuation using this modified method for the complete Byrd Glacier is shown below in Figure 4.7.

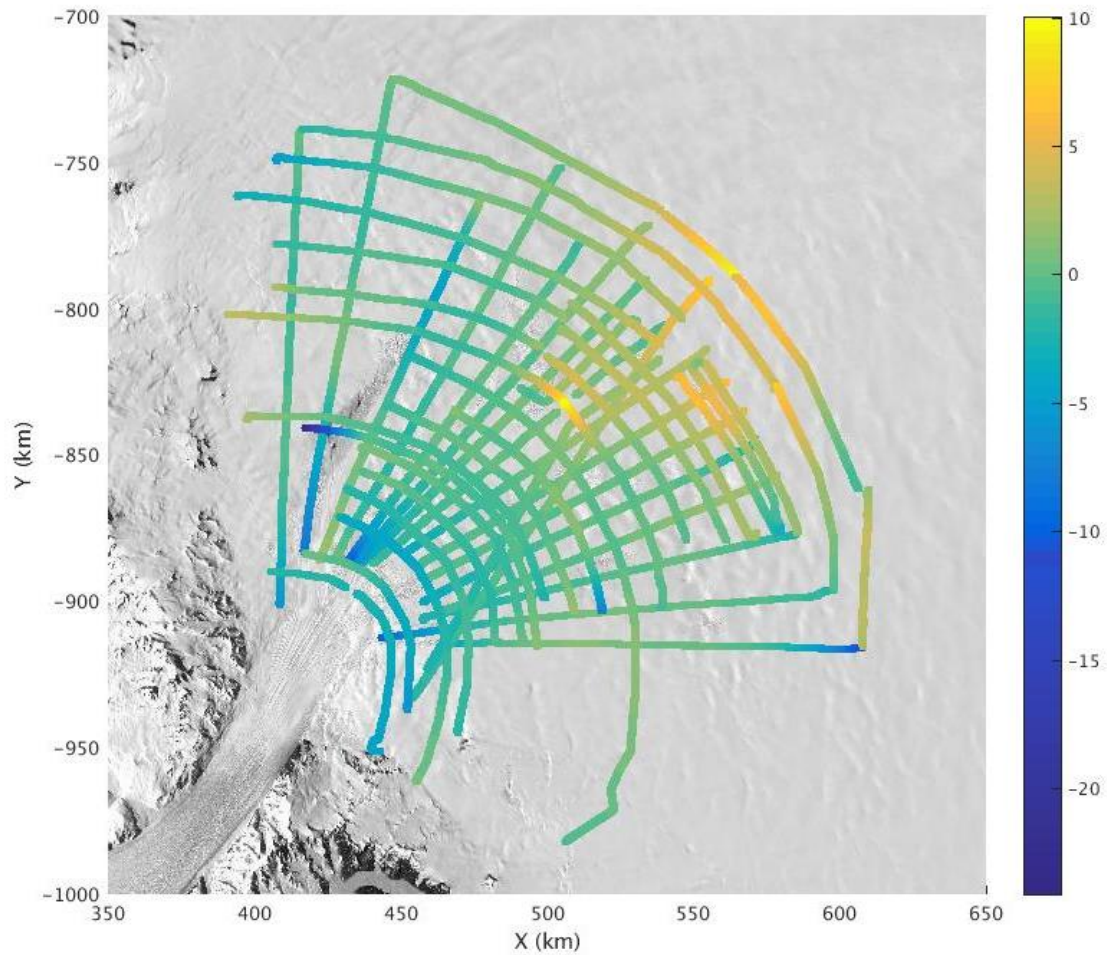


Figure 4.7 Estimated Relative englacial attenuation in dB using modified attenuation rate

Considering average power values for every 200m and after correcting for roughness using the method described in section 3.3 of Chapter 3, The complete map of relative reflectivity values estimated using the modified attenuation rate is shown in Figure 4.8. The areas with high relative reflectivity values might represent unfrozen subglacial materials or potentially a subglacial lake

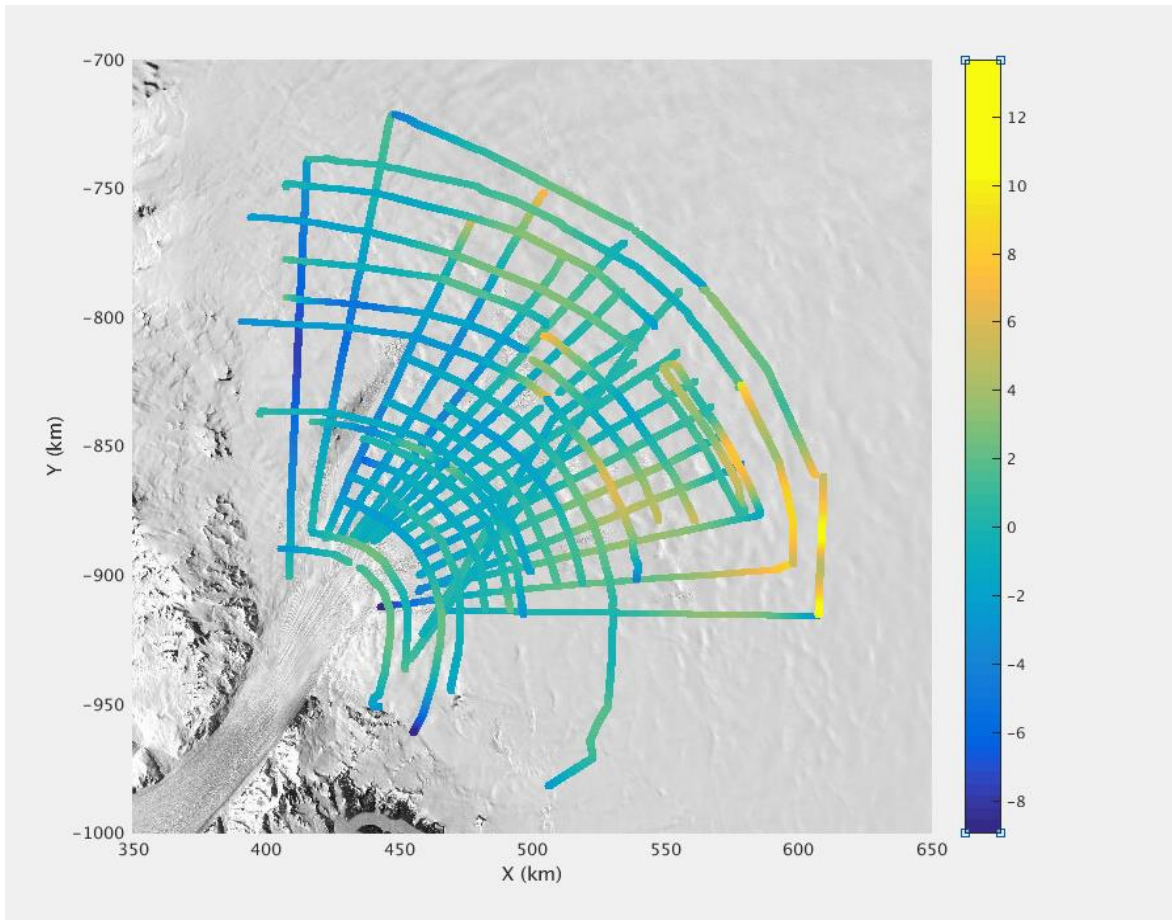


Figure 4.8 Relative reflectivity values estimated using the modified attenuation rate

The histograms of estimated basal conditions using a constant attenuation rate and this modified attenuation rate are shown below in Figure 4.9.

From the Figure 4.9, the range of reflectivity values estimated using modeled attenuation are more realistic than those estimated by considering a constant attenuation. This addresses the observed non-linear relationship between the apparent attenuation and depth.

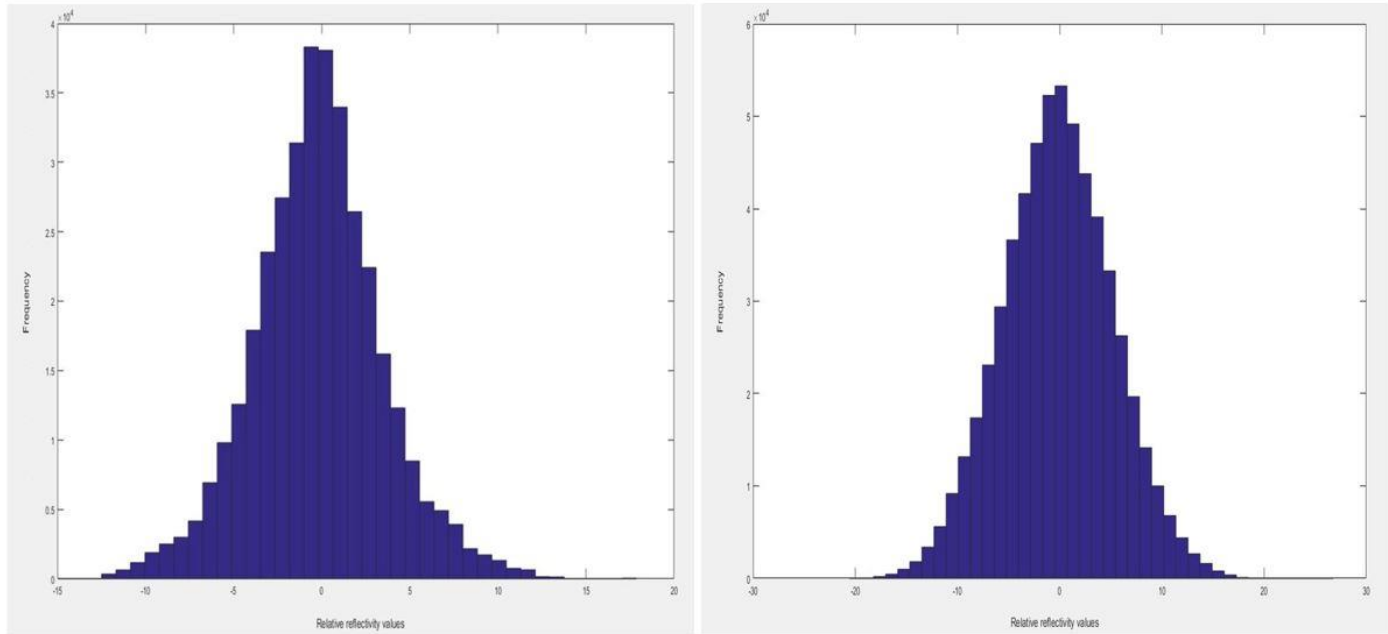


Figure 4.9 Histograms of estimated relative reflectivity values using modeled attenuation rate (on left) and constant attenuation rate (on right)

4.3 Localized englacial attenuation

Another way to address this non-linearity is to assume N_a as a constant for a short interval of depth. As shown in the Figure 4.10, N_a is assumed to be a constant over a range of depth intervals, i.e. N_a value is piece-wise linear.

Figure 4.11 shows the estimated N_a values in the along track dimension in red color and the apparent attenuation in blue

If this N_a value vector, as a function of depth, is used to generate the relative reflectivity values, the obtained range of reflectivity value is again physically unrealistic – maybe because the along track variations are not considered i.e., different locations at the same depths are treated as similar.

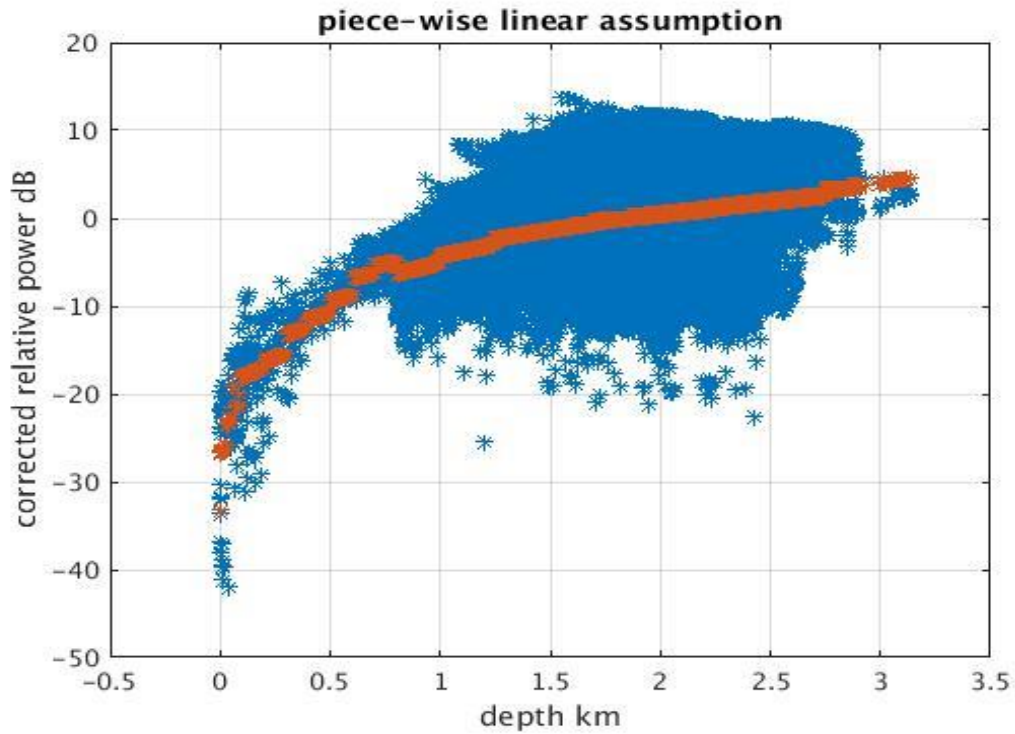


Figure 4.10 Variation of assumed N_a for different depth values

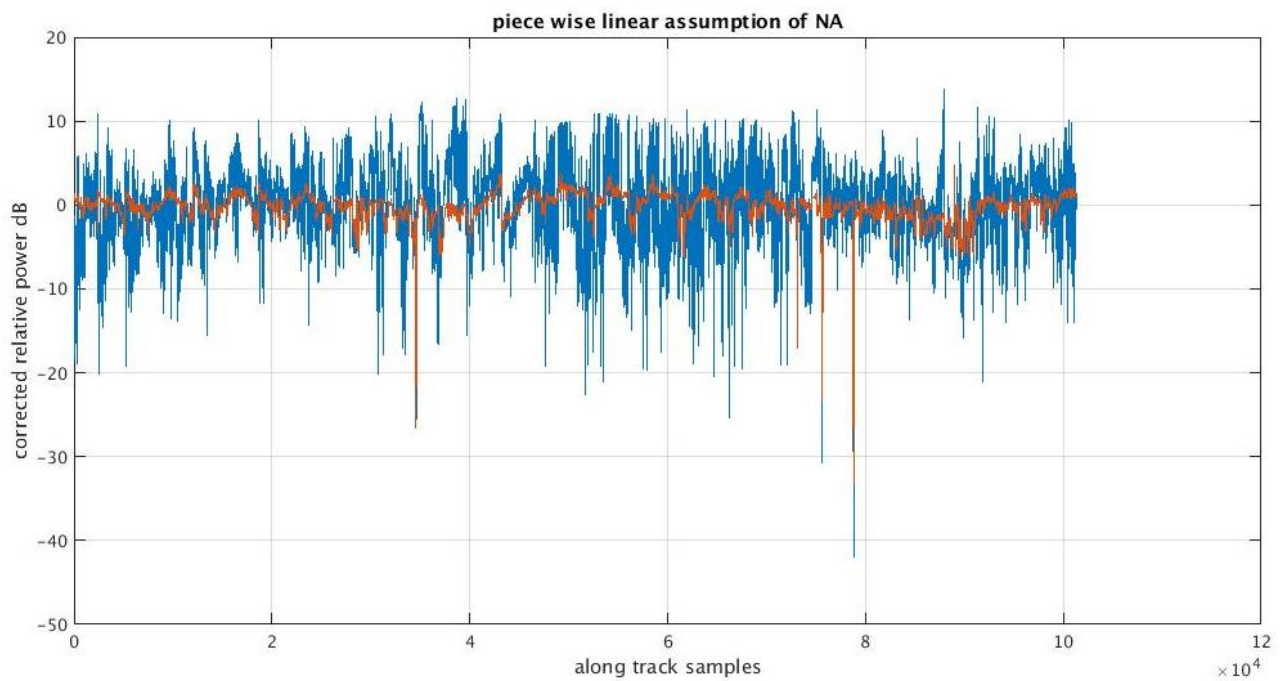


Figure 4.11 N_a values (shown in red color) in along track dimension and the apparent attenuation (shown in blue)

To constrain variations in both location and depth, a short interval of along track distance is considered such that the area considered is localized and the depth variation in the localized area is minimized. For each localized along track interval, a unique N_a value is estimated. Figure 4.12 shows the estimated N_a for short intervals in the along track direction:

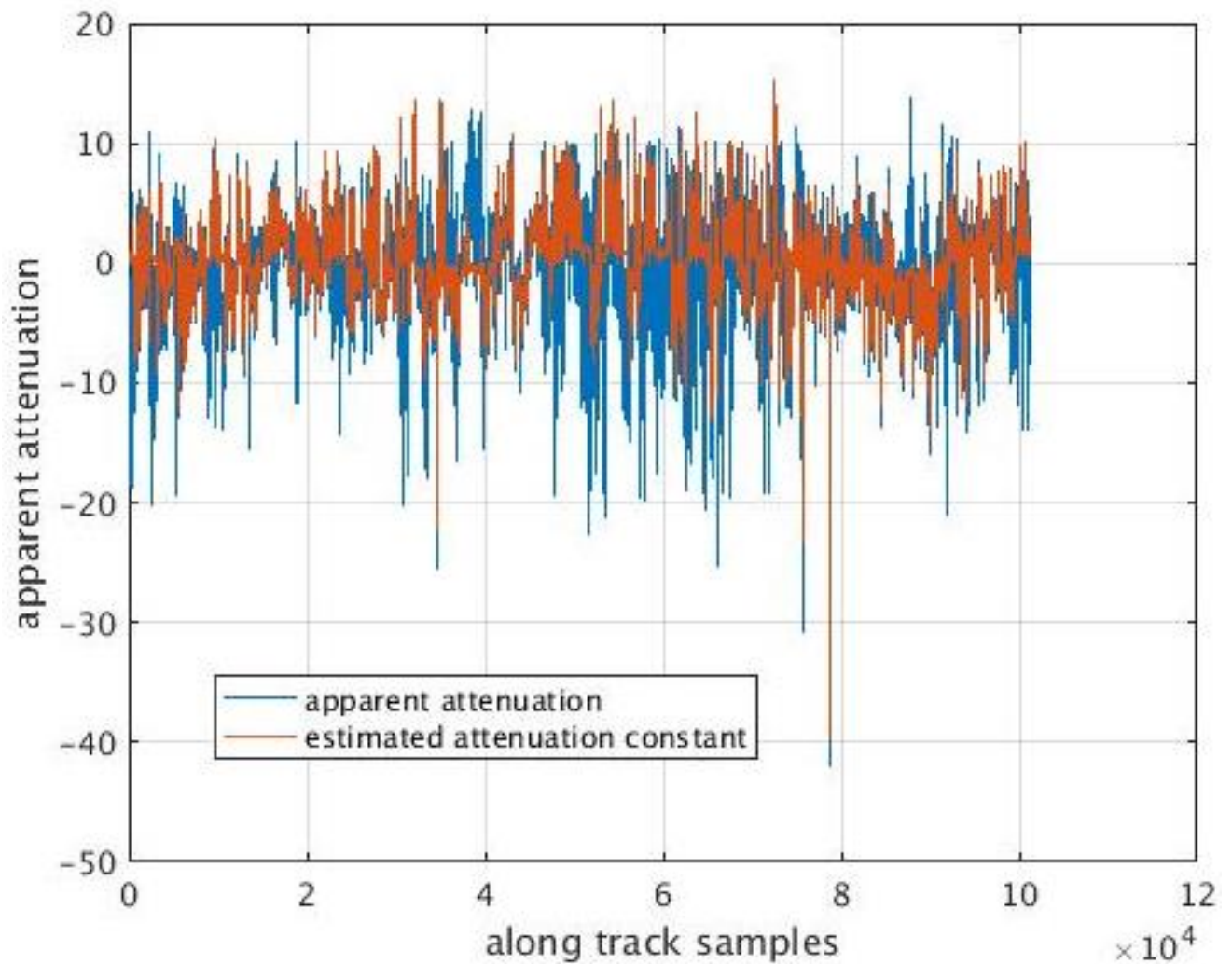


Figure 4.12 Estimated N_a for short intervals in the along track direction

This estimated englacial attenuation seems to have a better match with the apparent attenuation. The differences in the estimated relative englacial attenuation and the apparent attenuation are due to relative reflectivity values.

The estimated relative englacial attenuation map using the modeled N_a value for every 1 km of along track length is shown in Figure 4.13

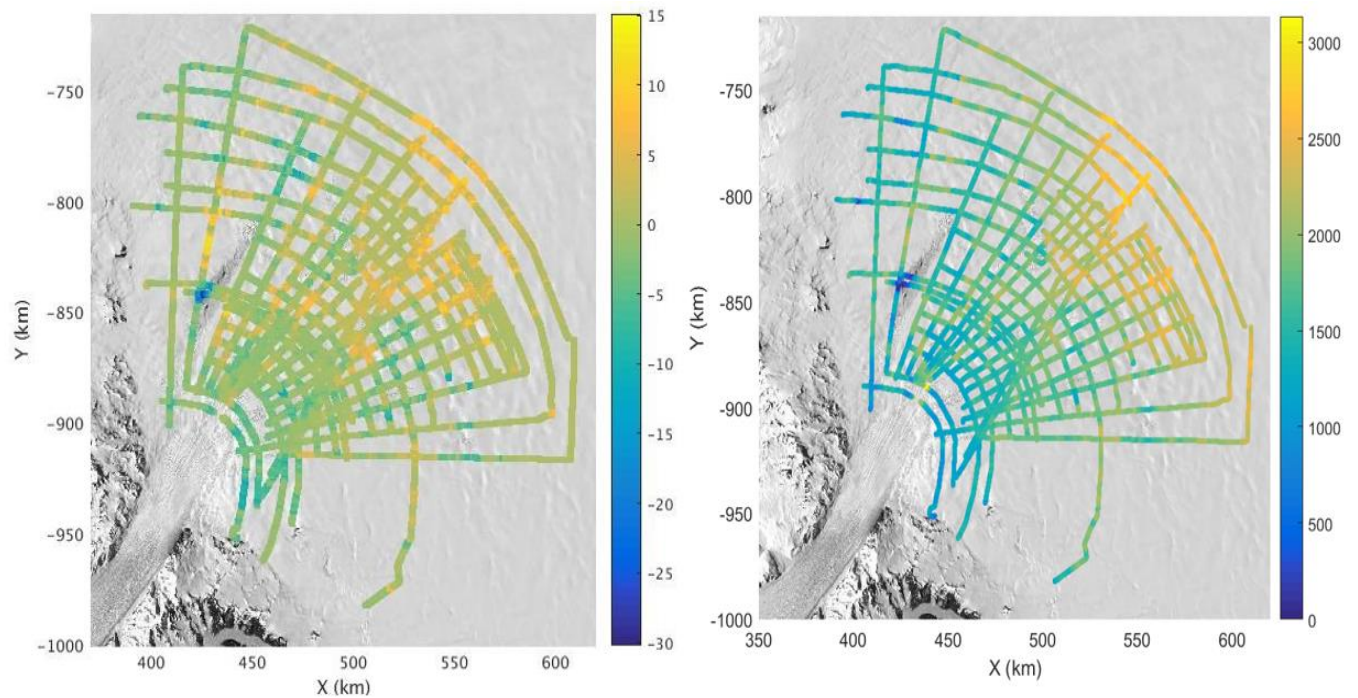


Figure 4.13 Estimated relative englacial attenuation in dB assuming a localized attenuation rate (shown on the left side) and the depth at the corresponding locations (shown on the right side)

From the above estimated englacial attenuation map, different englacial attenuation values for different locations – even if they have a relatively close range of depth values, can be observed.

Chapter 5 Results and validation

5.1 Estimated relative reflectivity values

The complete data are divided according to flight lines. For roughness estimation each flight line is again divided into chunks of about 200m in the along track dimension and roughness parameters are calculated for each chunk. The englacial attenuation is modeled for data chunks of every 1km of along track length. The estimated relative reflectivity values using the estimated N_a in the direction of along track are shown below in Figure 5.1 along with the previously identified locations with elevation changes [14]:

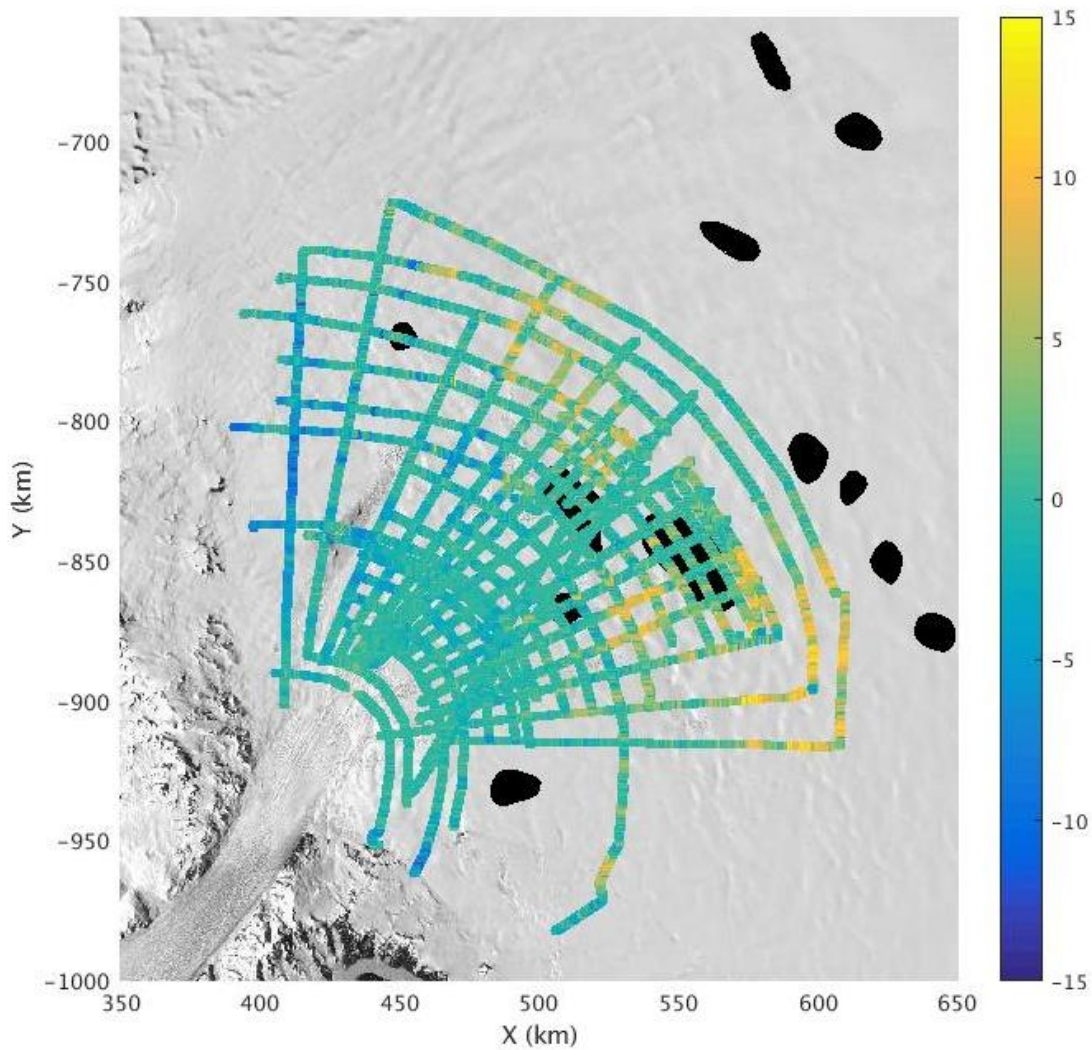


Figure 5.1 Relative reflectivity values using unique N_a for each 1km along track interval

5.2 Validation using cross-over analysis:

As shown in the above Figure 5.1, the relative high reflectivity values are evident in a few localized areas from different flight paths. Changing the englacial estimation window in the along-track dimension changes the estimated relative reflectivity values at few other location points – if the window length is increased to 10km in this case. A minimum window length is chosen to ensure the variations in the location and depth are minimized. There is no much difference in the estimated relative reflectivity values if the window length is further decreased below 1km.

At the same locations, the method should give similar relative reflectivity values. The cross over locations of the flight line are shown in the Figure 5.2.

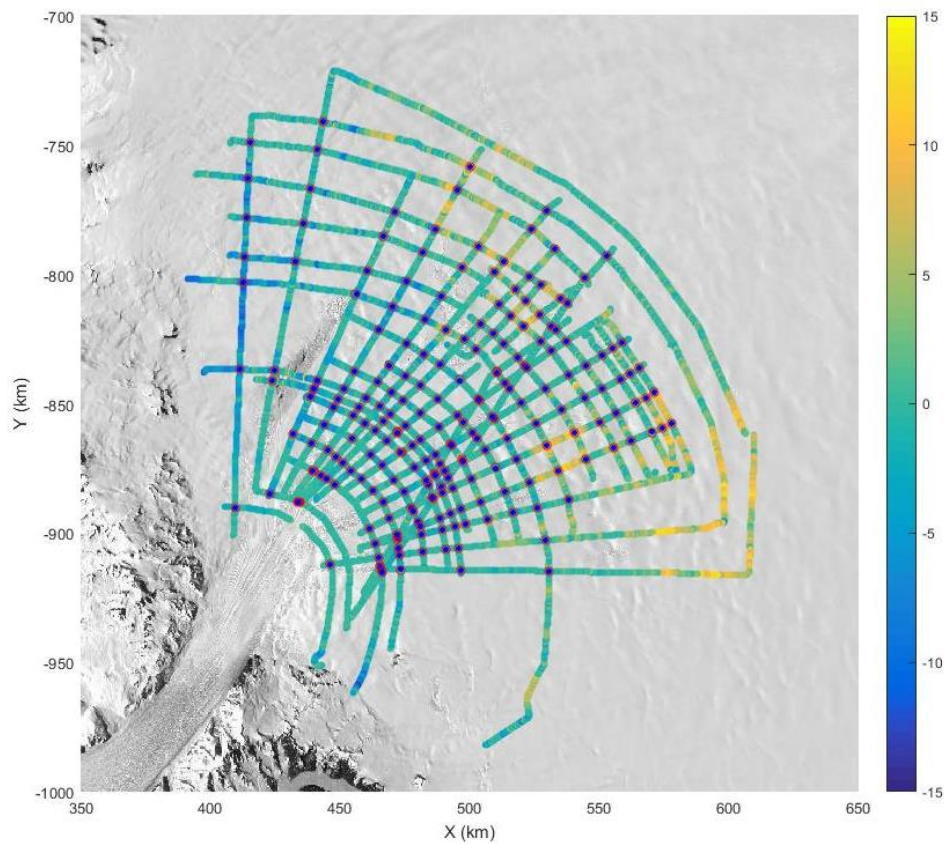


Figure 5.2 Relative reflectivity map with cross over locations

At the cross over locations of the flight paths, the difference in the estimated relative reflectivity values are shown in the Figure 5.3. The histogram of the difference in relative reflectivity values is shown in Figure 5.4 and the histogram of difference in depth at these locations is shown in Figure 5.5.

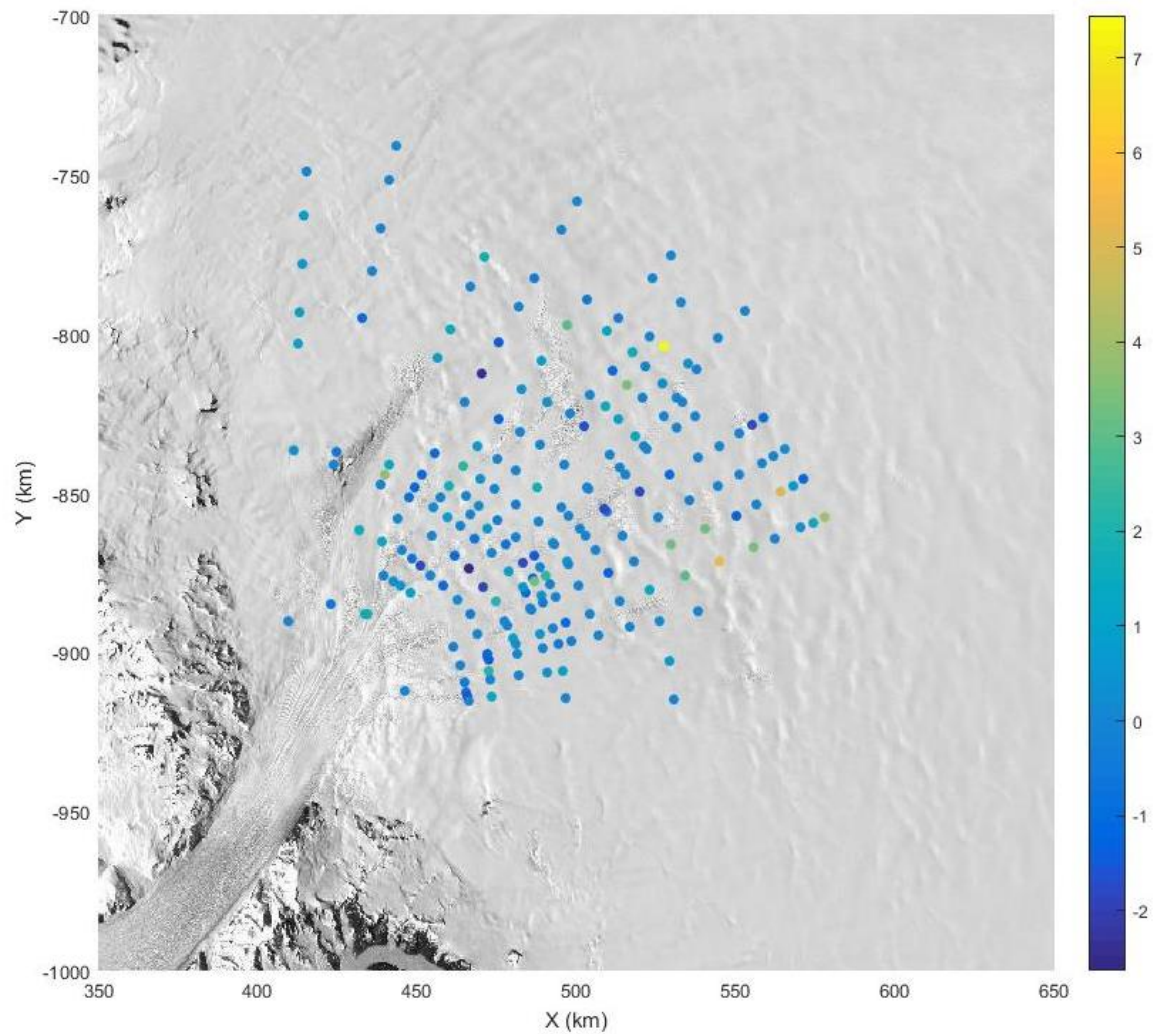


Figure 5.3 Difference in estimated relative reflectivity values at cross over locations

From the above figure, at most of the cross over locations, the differences in the estimated relative reflectivity values are less than 3dB.

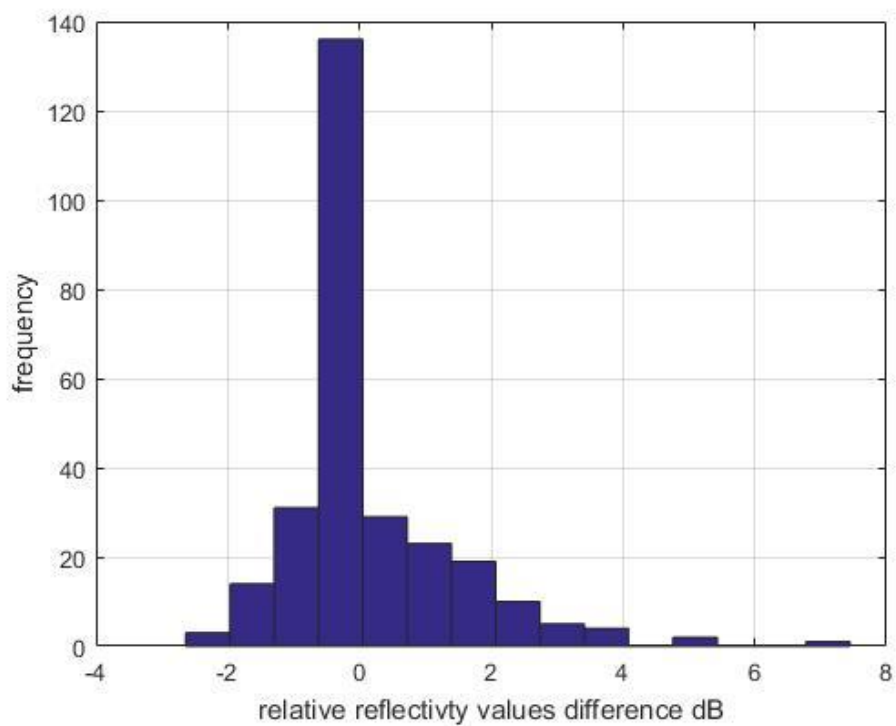


Figure 5.4 Histogram of estimated relative reflectivity value differences at cross over locations

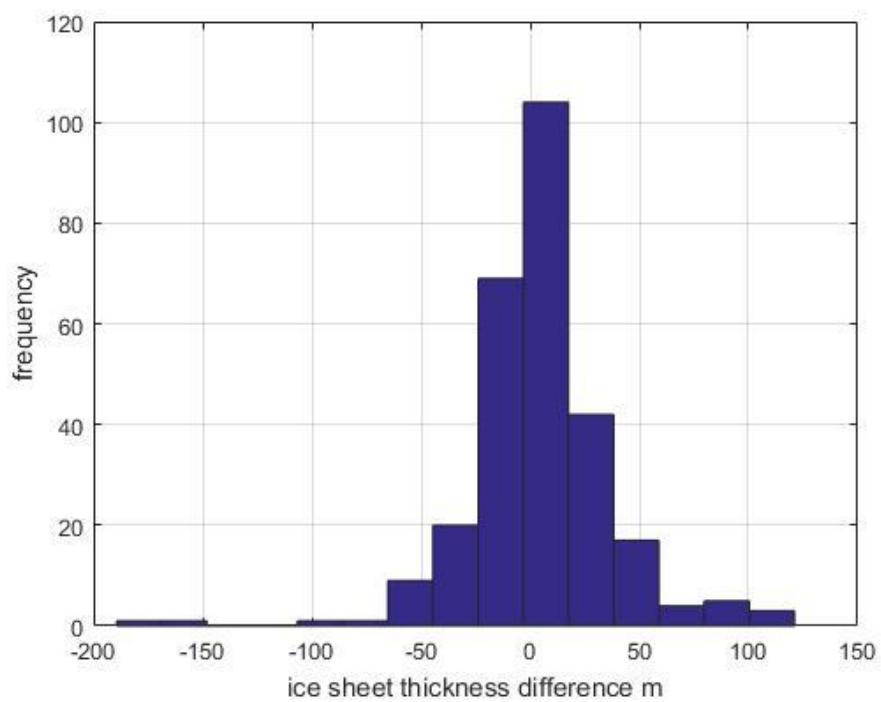


Figure 5.5 Difference in depth values of ice sheet at cross over locations

In the estimated relative reflectivity value difference map, the locations with differences greater than 5dB are shown in Figure 5.6 along with the plots of differences in relative reflectivity value and depth differences at those corresponding locations.

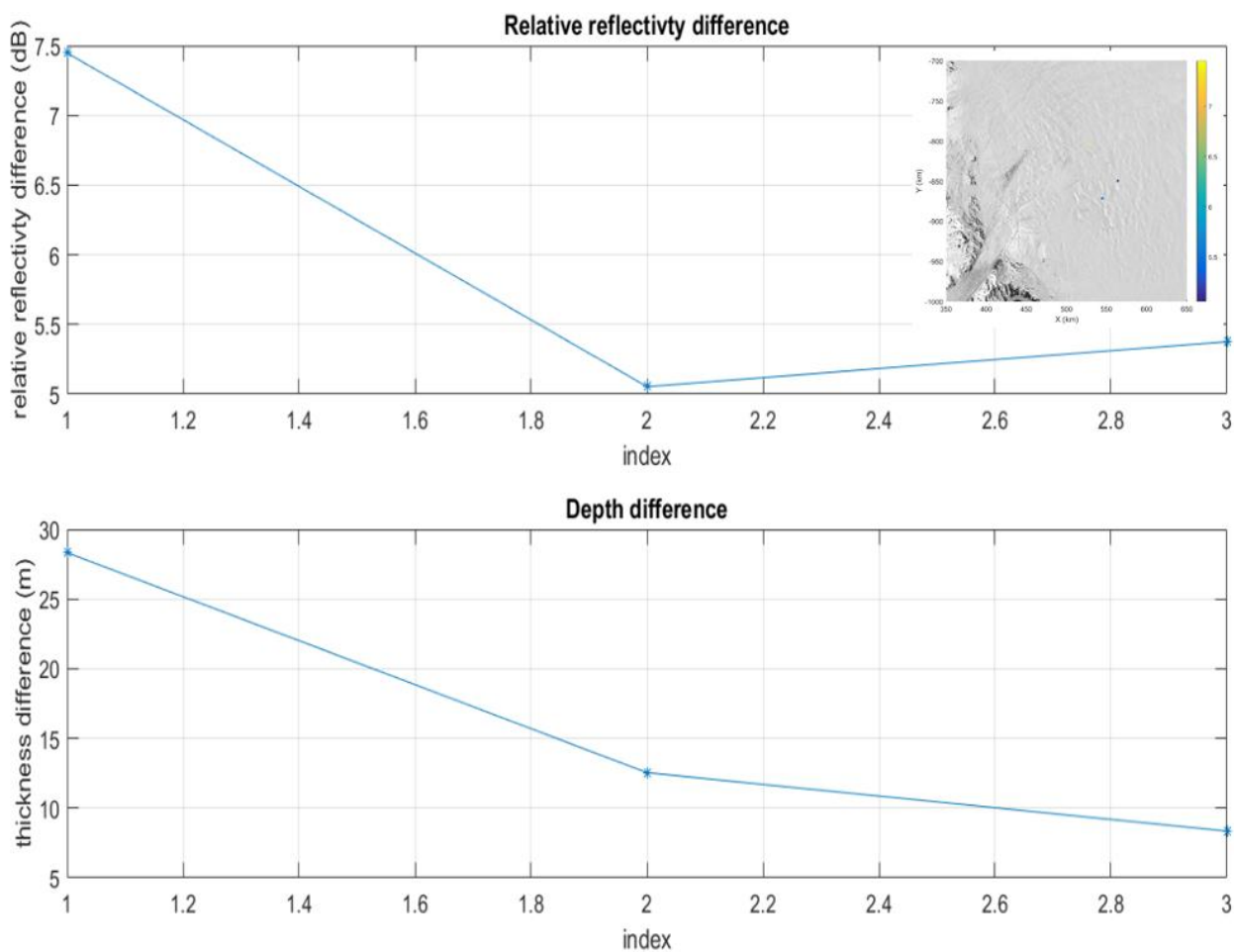


Figure 5.6 Differences in estimated relative reflectivity values and depth at the corresponding locations; these corresponding locations on the map are shown in top-right figure

The highest difference with a 7.5 dB value is caused by the roll effect of the flight, i.e. for one of the flight paths, power returned is reduced due to the roll of the aircraft which in turn caused the highest

difference in the estimated relative reflectivity values. The corresponding locations along with the received power and the roll angle of the aircraft at the crossover are shown in the Figure 5.7 below

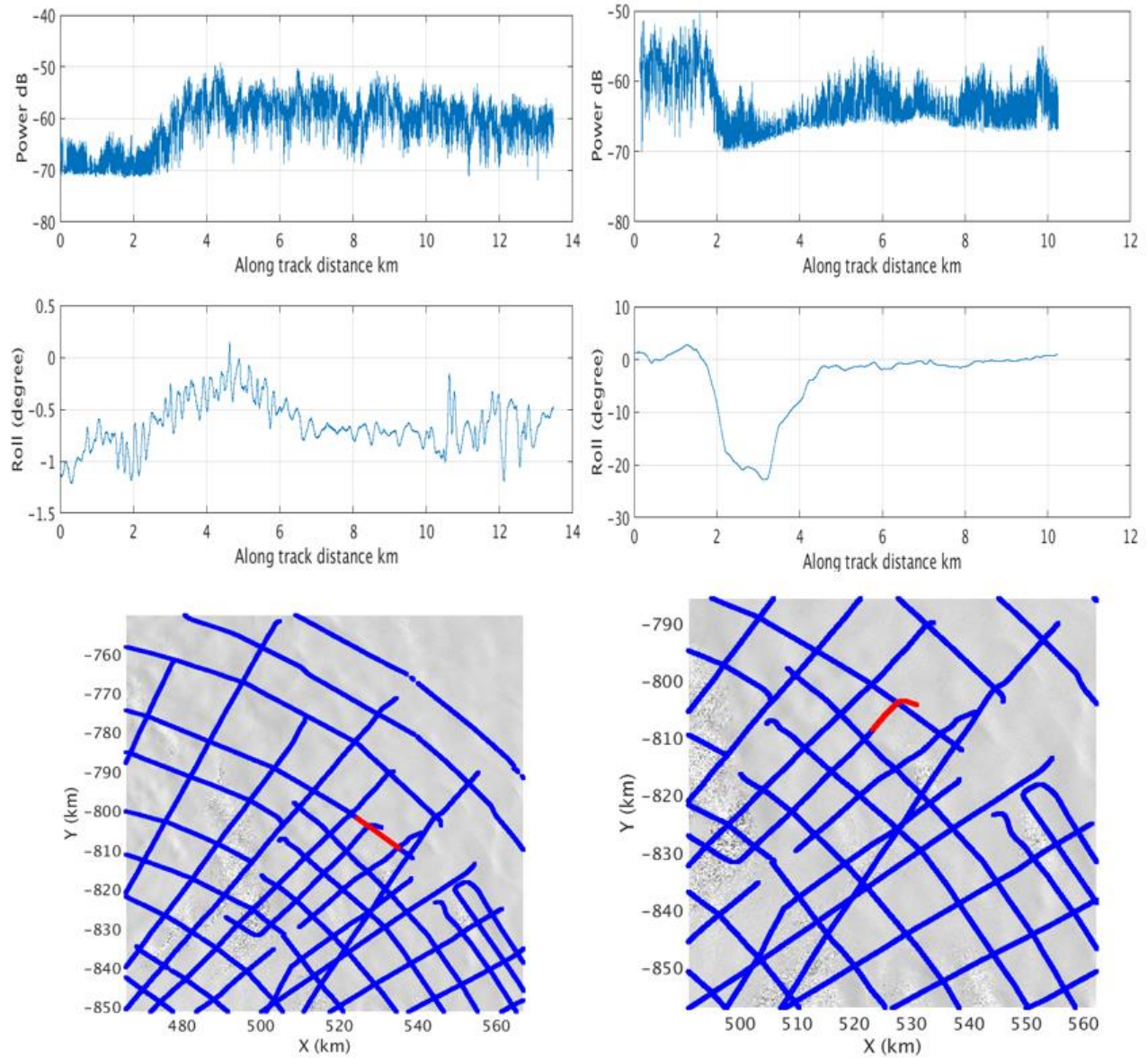


Figure 5.7 Plots of received power from ice-bed interface along with the roll of aircraft from corresponding flight path locations 20111212_01_018 (on left side) and 20111228_02_001 (on right side)

For other two locations with differences in relative reflectivity values around 5dB (shown in Figure 5.6), one of the flight line location resides on the boundary of the estimated high reflectivity area.

5.3 Validation using Geo-physical Features

In order for a subglacial water body to exist, it should have these following features [24],

- i) The thickness of the ice sheet should be large enough to insulate the heat. There should be a sufficient geothermal flux of earth. From the echograms in Figure 5.8, the large depths, about 2000 to 2500 m, at the ice – bed interface can be verified.

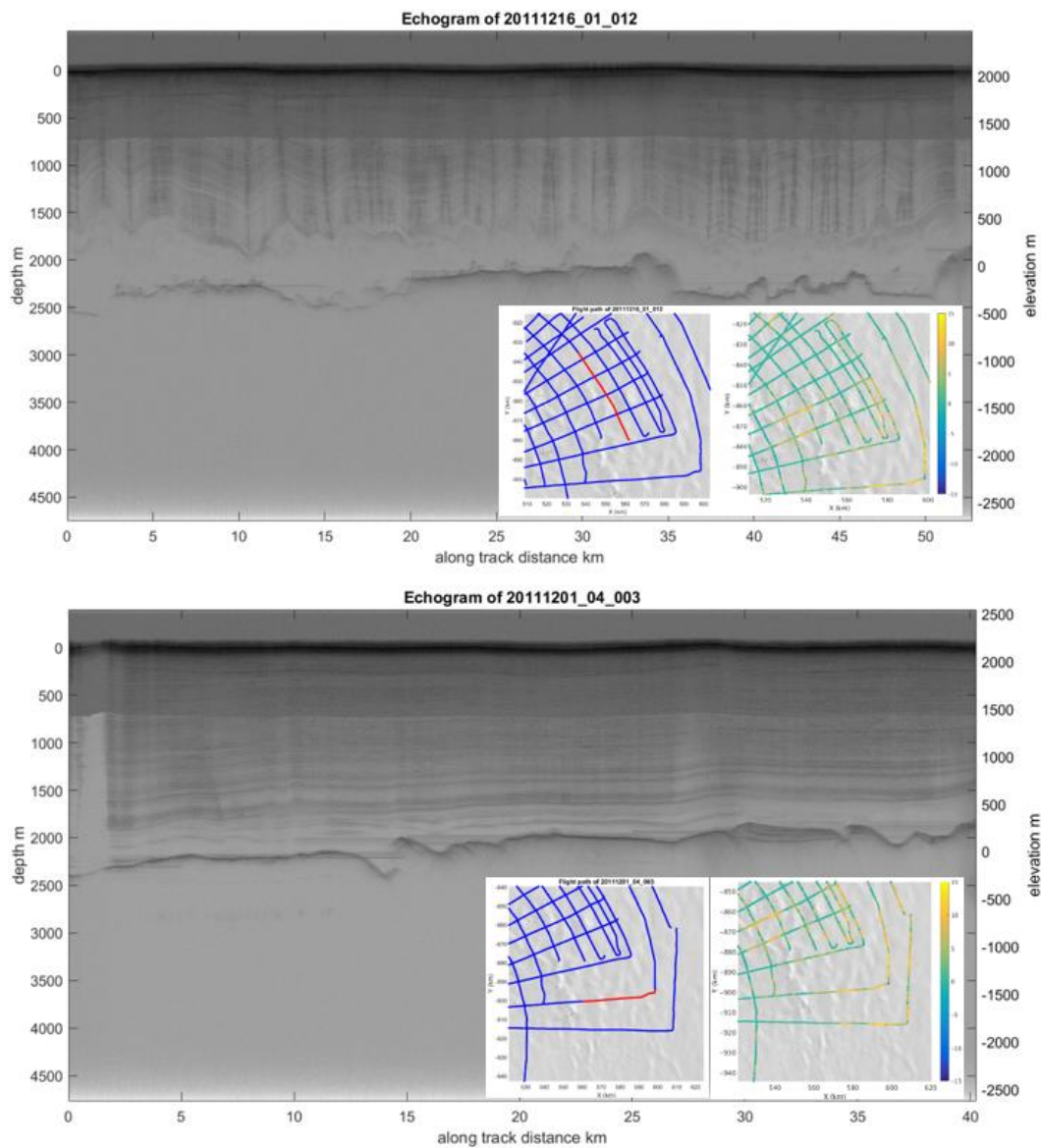


Figure 5.8 Examples for high thickness of the ice sheet with corresponding flight path locations and estimated relative reflectivity map shown inside the echogram

- ii) For the water to stay in a particular location, the ice – bed interface configuration should be such that the water can accumulate. This feature can be verified from the echograms of the Figure 5.9 along with the elevations at those locations.

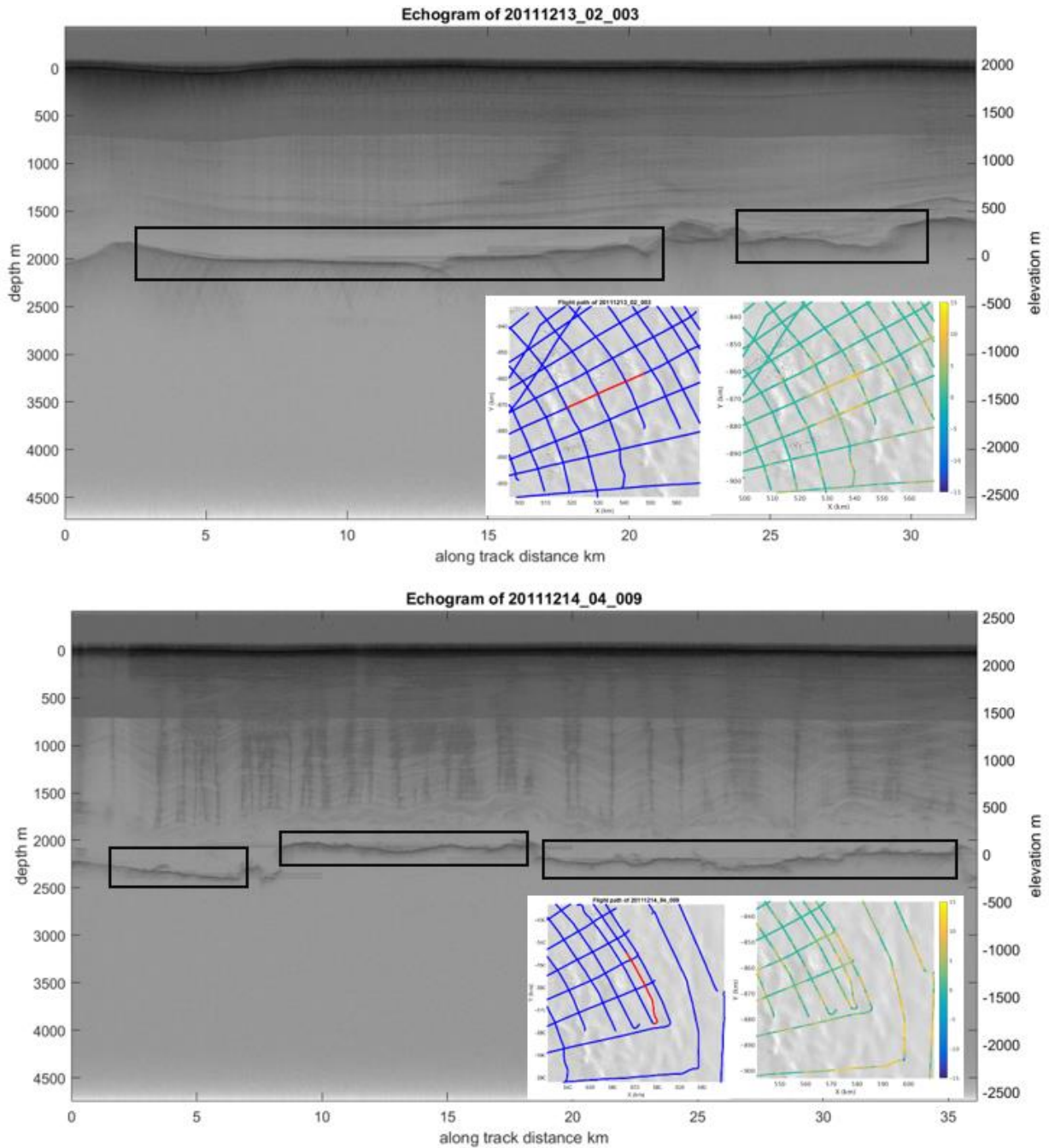


Figure 5.9 Examples for ice-bed interface configurations (highlighted with a black color rectangle) with corresponding flight path locations and estimated relative reflectivity map shown inside the echogram

- iii) When illuminating with electromagnetic energy, if there is a presence of water, then there would be a high dielectric contrast at the bed interface and this high dielectric contrast will give a bright ice- bed reflection in echograms. This feature can be observed in Figure 5.10.

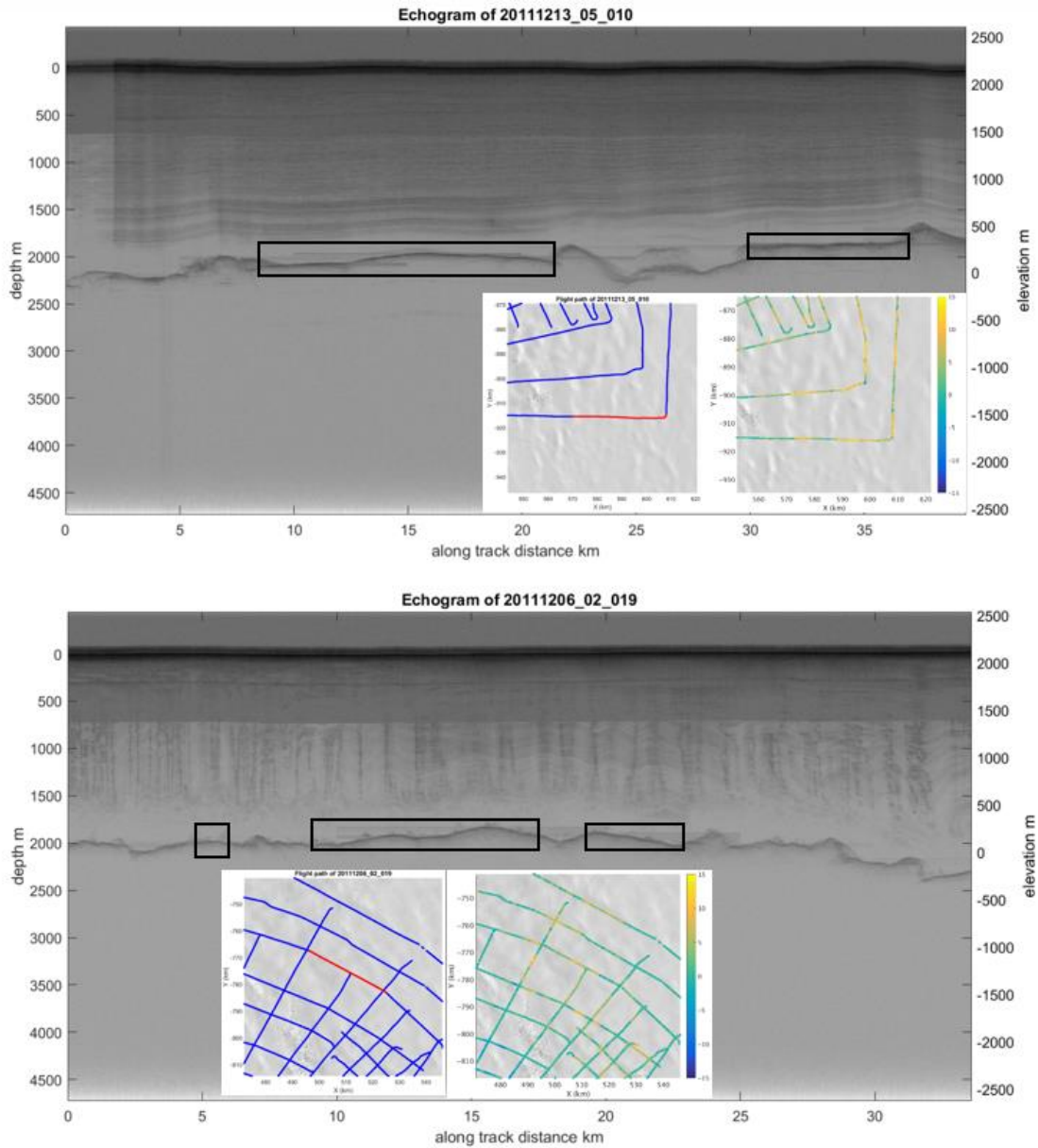


Figure 5.10 Examples for high dielectric contrast at the ice – bed interface (highlighted with a black color rectangle) with corresponding flight paths locations and estimated relative reflectivity map shown inside the echogram

- iv) If there is water present at the ice – bed interface, there will also be an absence of basal shear stress, which will give rise to a flat overlying ice sheet surface and water support the overburden pressure giving a flat ice – bed interface reflections than the surroundings. The correlations between the flat ice sheet surface and high relative reflectivity values can be observed from the air – firm interface roughness map and the relative reflectivity map from the Figure 3.13 and Figure 5.1. Echograms of two such locations are shown in Figure 5.11.

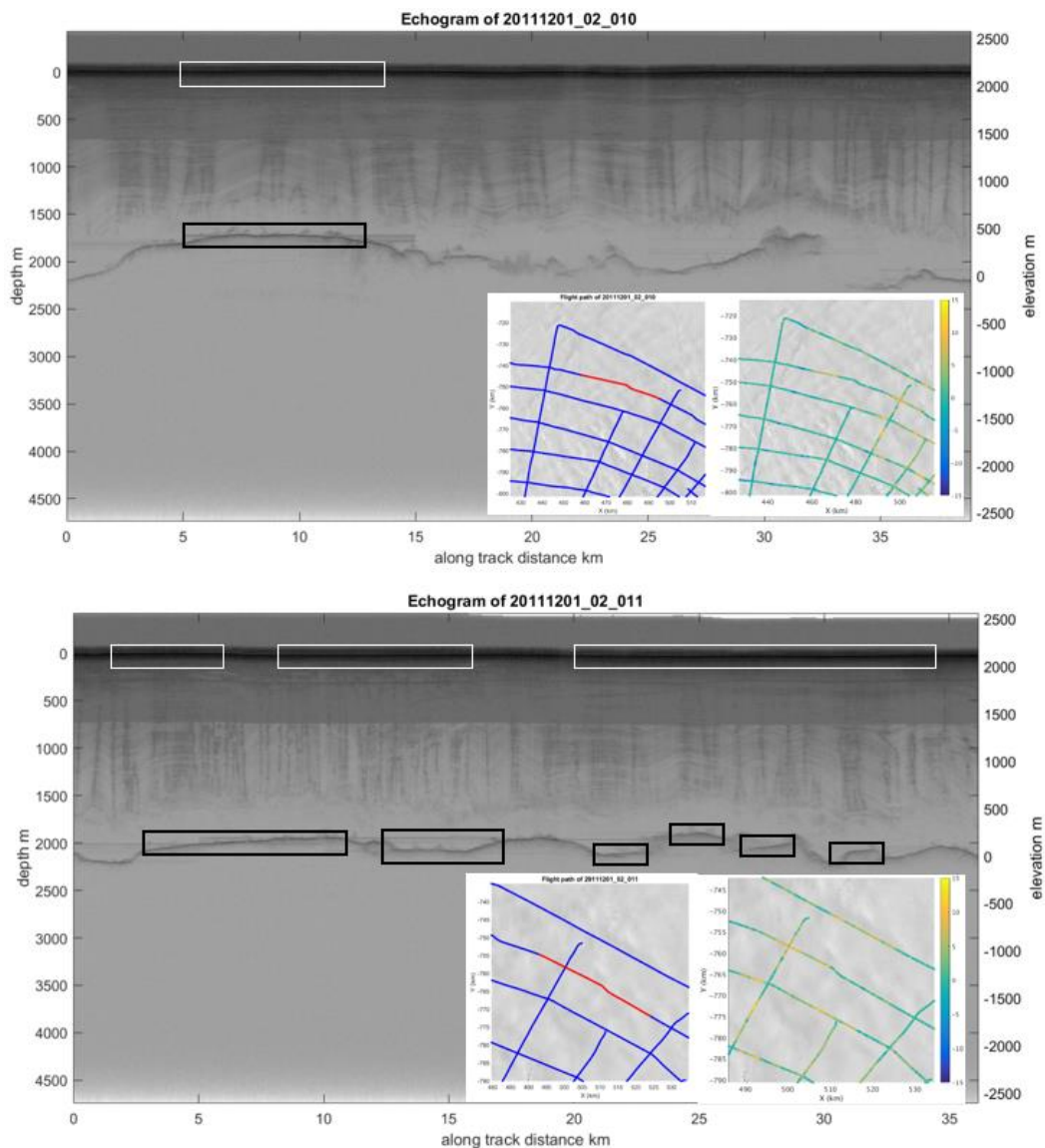


Figure 5.11 Examples for a flat air-firm interface and flat ice – bed interface (highlighted with white and black color rectangles, respectively) with corresponding flight path locations and estimated relative reflectivity map shown inside the echogram

- v) Due to the presence of water, the angle of internal reflectors dipping would be greater than the bed topography. This feature can be verified using the echograms in the Figure 5.12.

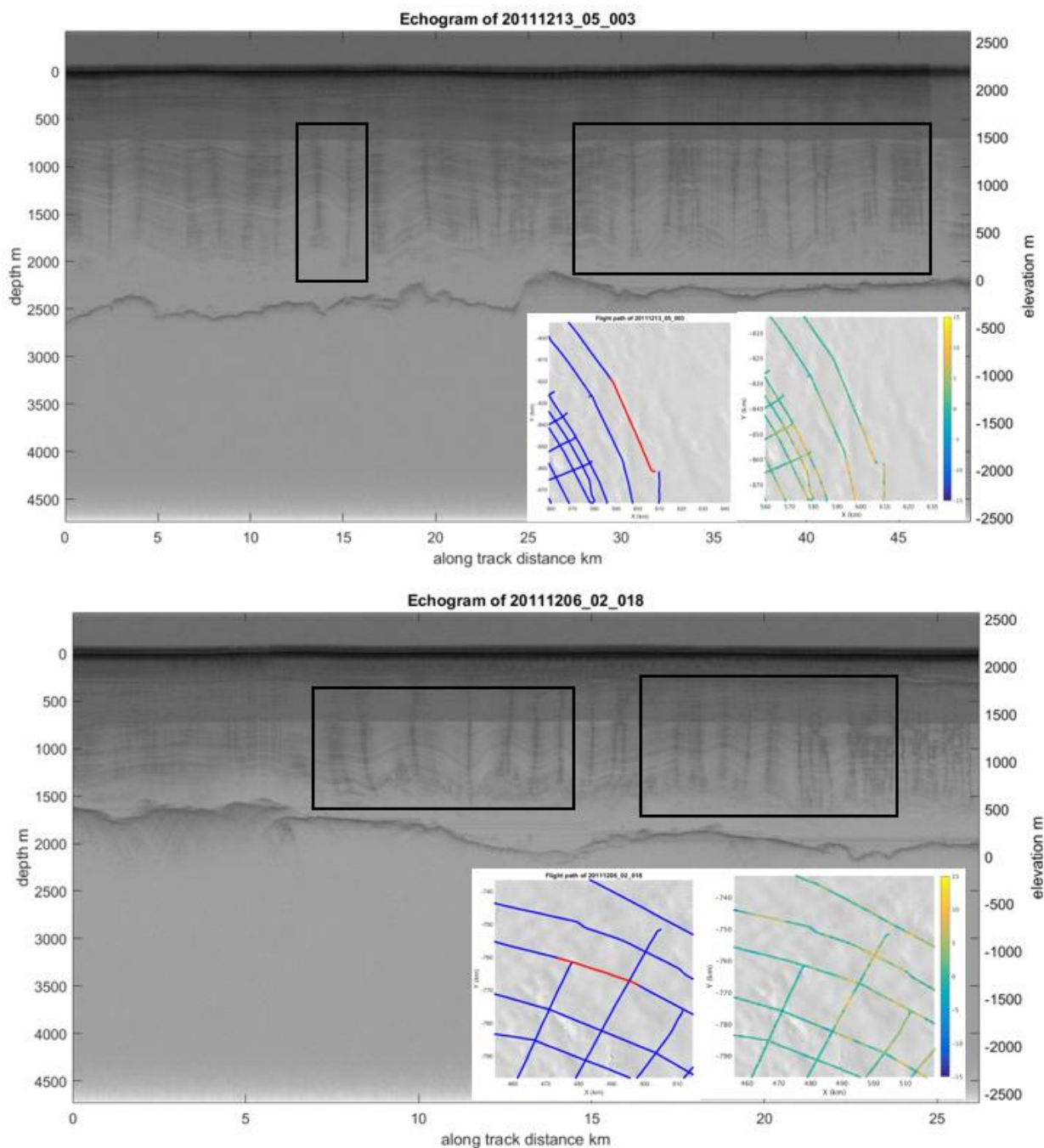


Figure 5.12 Examples for angle of internal reflectors dipping greater than bed topography (highlighted with a black color rectangle) with corresponding flight path locations and estimated relative reflectivity map shown inside the echogram

5.4 Validation using abruptness index:

The potential presence of water can also be validated using the reflection abruptness index [33]. The calculated reflection abruptness index values for the two locations with high estimated relative reflectivity values are shown in Figure 5.14 and Figure 5.15 along with flight path, corresponding echogram and plot of estimated relative reflectivity values. At these locations, previously discussed geo-physical features – high ice sheet thickness, high dielectric contrast, disturbances in the internal layers, ice-bed interface configuration suitable to accumulate subglacial water and flat air-ice interface can also be observed in the corresponding echograms.

The correlations between the calculated abruptness index and the estimated relative reflectivity values can be observed over the complete Byrd Glacier data in the Figure 5.13 below:

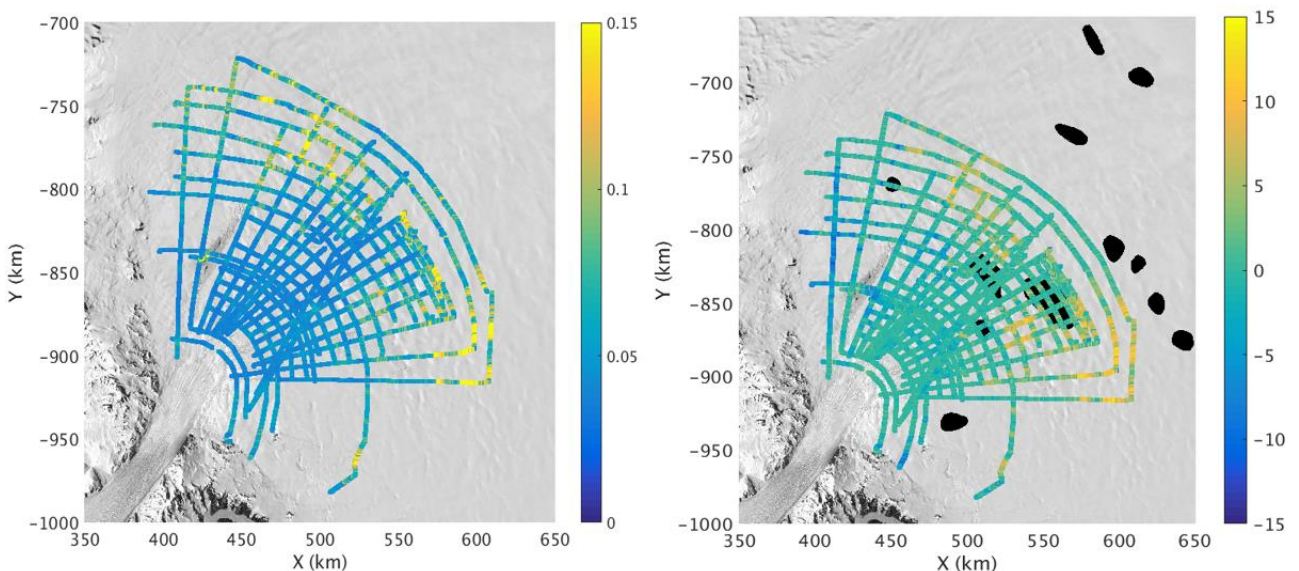


Figure 5.13 Abruptness index and estimated relative reflectivity maps

In the above figure, for most locations, there is a good match between the locations with high abruptness index values and high relative reflectivity values.

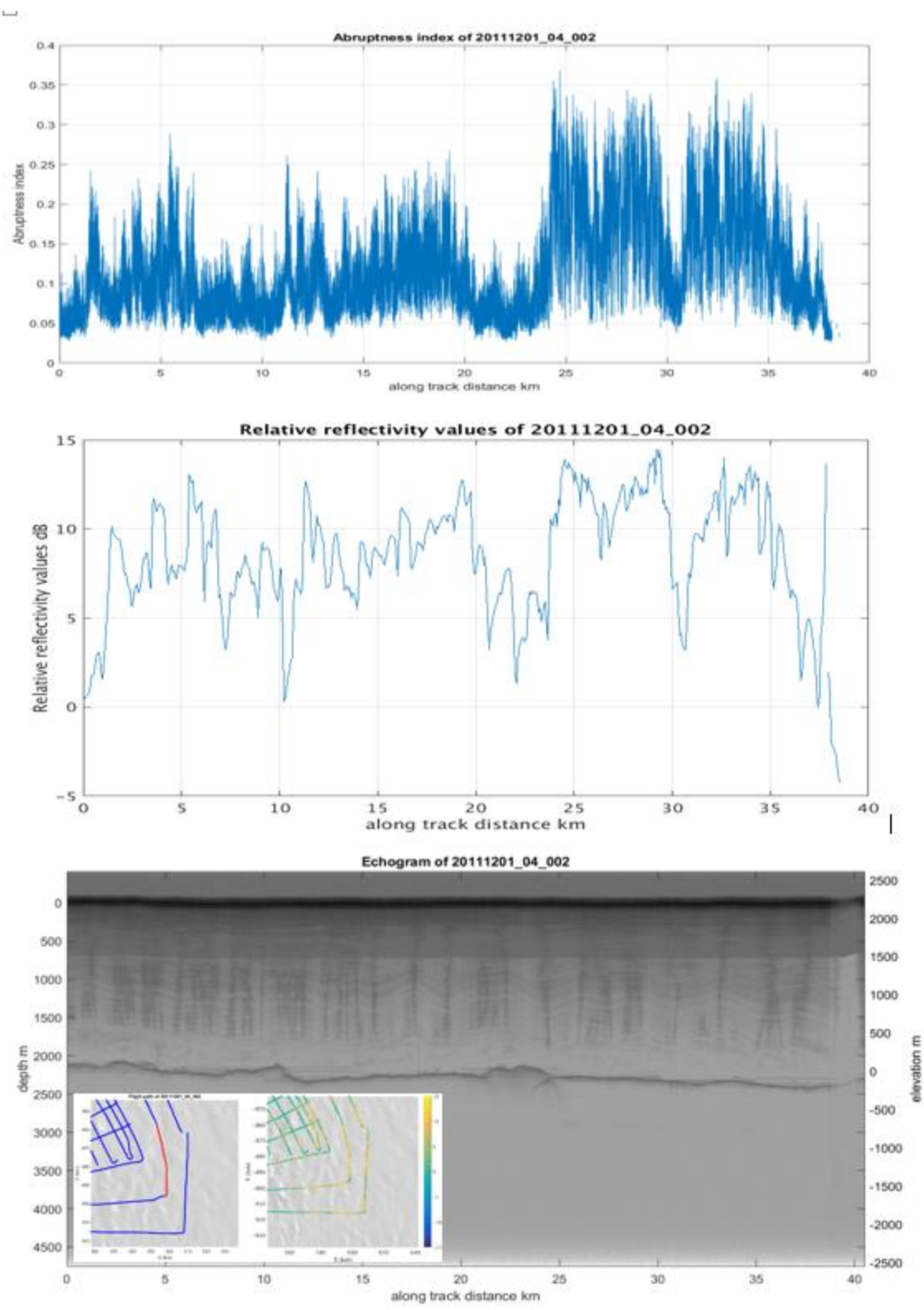


Figure 5.14 Abruptness values, relative reflectivity values and echogram with flight path locations for data frame 20111201_04_002

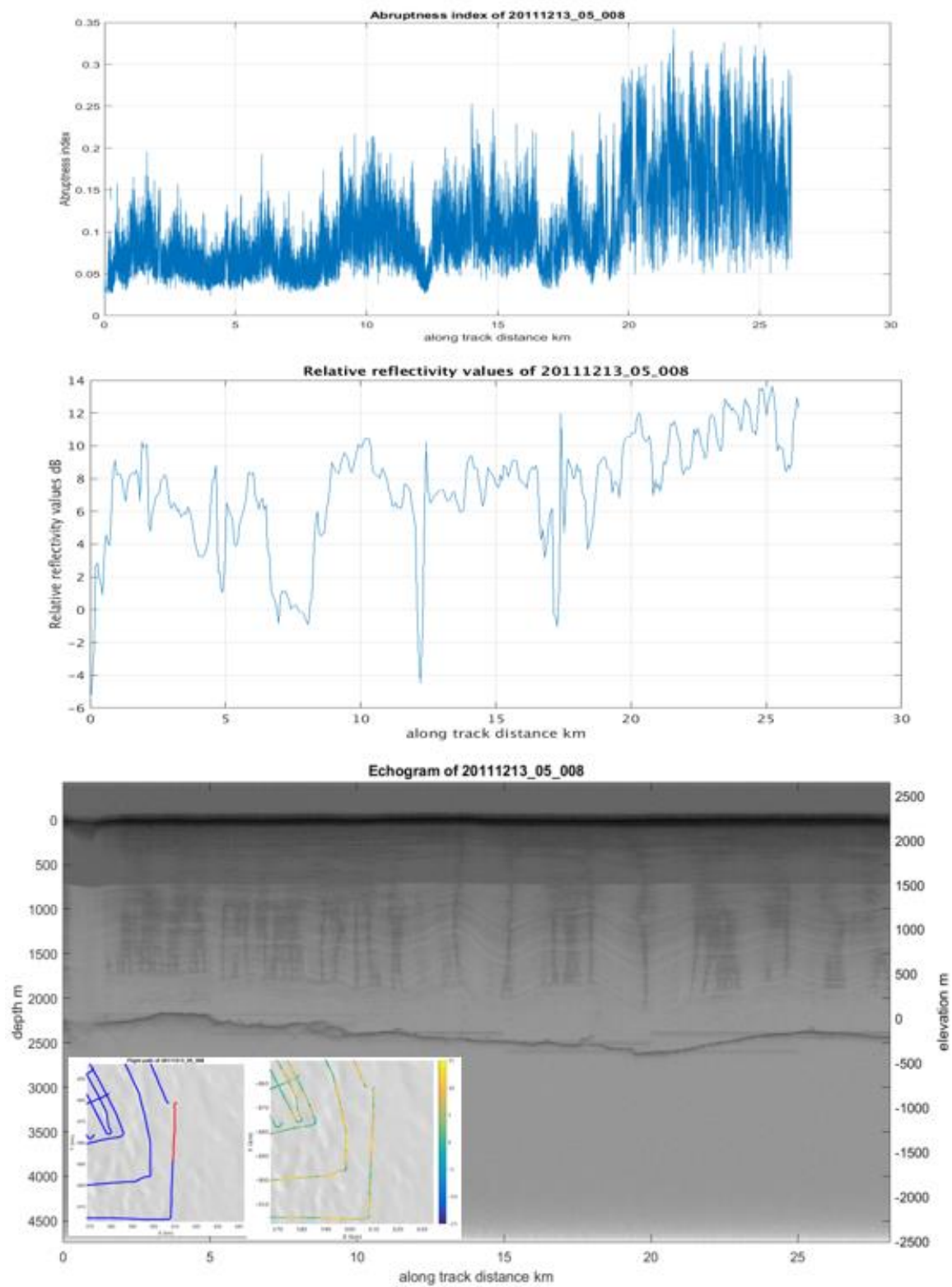


Figure 5.15 Abruptness values, relative reflectivity values and echogram with flight path locations for data frame 20111213_05_008

5.5 Correlation with predicted subglacial lakes and flow paths

Out of the seventeen sites of rapid ice-elevation changes identified within the Byrd Glacier catchment [14], twelve sites are close to the available data spatial extent. The rapid ice-elevation changes are calculated from the ICESat data collected during 2003 – 2008. The volume history of all the seventeen sites [21] are shown in the Figure 5.16 during 2003 – 2008.

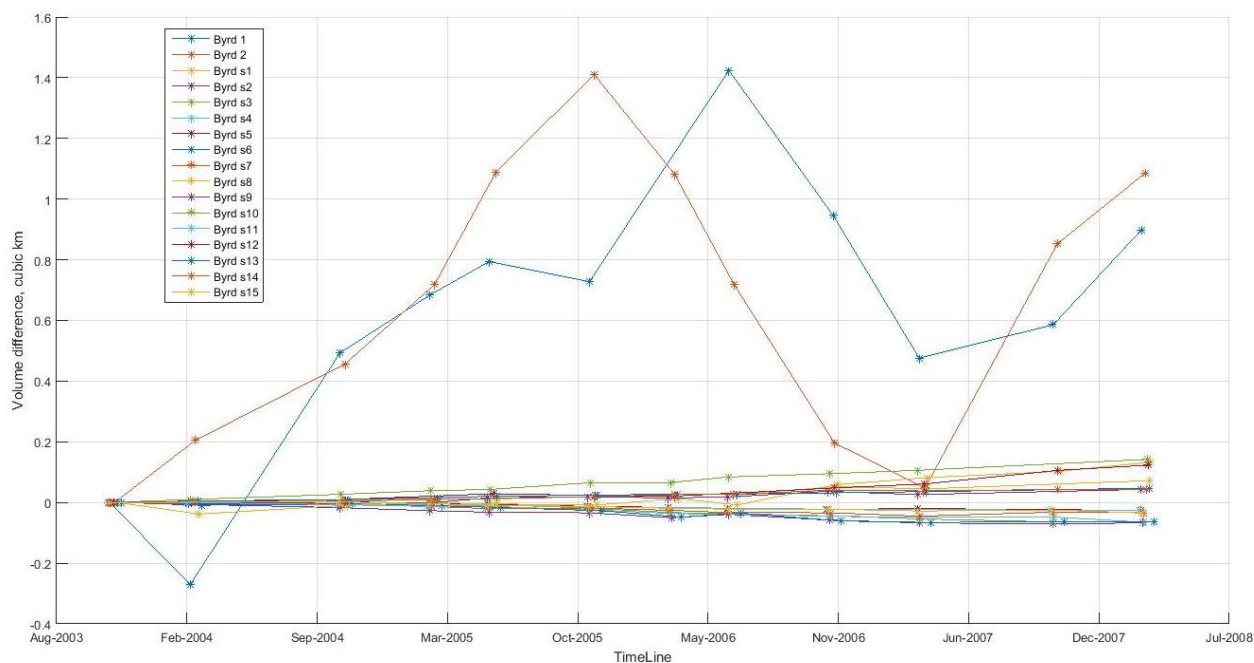


Figure 5.16 Volume change history of seventeen sites

In the above figure, the two sites with the highest changes are the two lakes with greater area shown in the relative reflectivity map. The locations with the estimated high reflectivity values do not exactly overlap with the previously identified locations with rapid ice elevation changes, but they are close to those locations. This could be due to the time difference of the data. This data is collected in 2011 over the Byrd glacier and the ICESat data is from 2003 – 2008. So the potential subglacial water could have moved beneath the ice sheet.

The potential subglacial water if exists and if it could have moved beneath the ice sheet, it will take the flow paths which are perpendicular to the contours of the hydraulic potential of the ice sheet. The hydraulic potential φ of an ice sheet is given by

$$\varphi = \rho_w g z_b + \rho_i g (z_s - z_b) \quad (5.1)$$

where g is the acceleration due to gravity (9.8 ms^{-2}), z_b is the elevation of the ice – bed interface and z_s is the elevation of the air – firm interface, ρ_w and ρ_i are the bulk densities of water (1000 kg m^{-3}) and ice (910 kg m^{-3}) respectively[39] [40].

The hydraulic potential map of Byrd Glacier in dB is shown in Figure 5.17 below

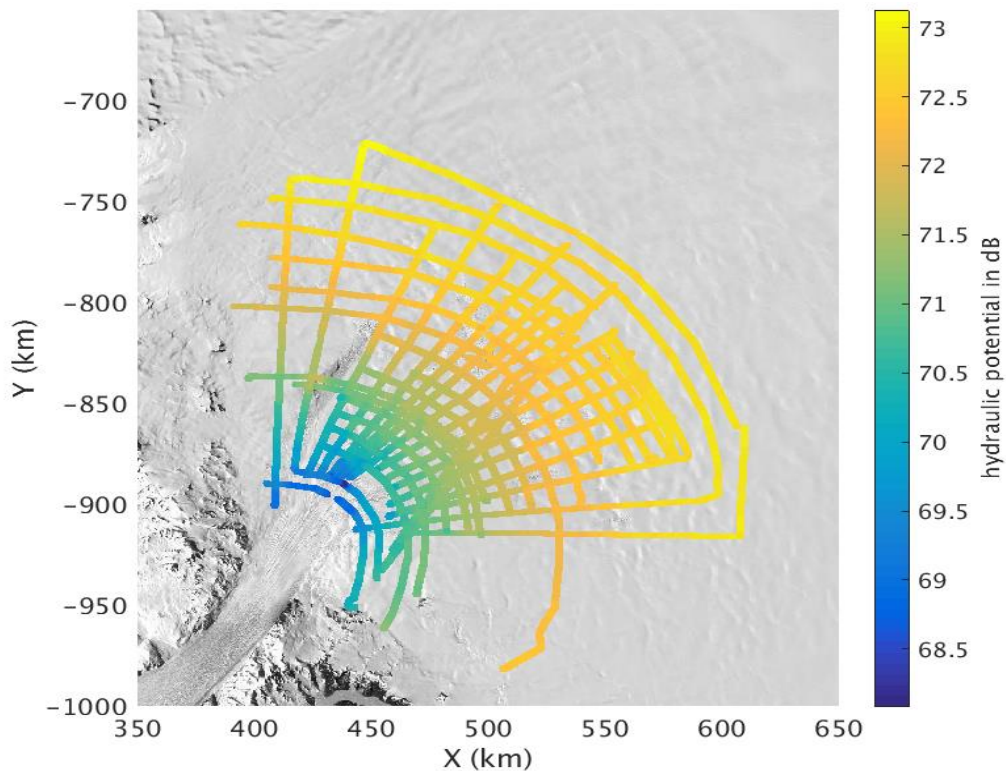


Figure 5.17 Hydraulic potential map of Byrd glacier in dB

The 2D interpolated relative hydraulic potential is shown in the Figure 5.18 below and the contours of equipotential of φ are shown in Figure 5.19

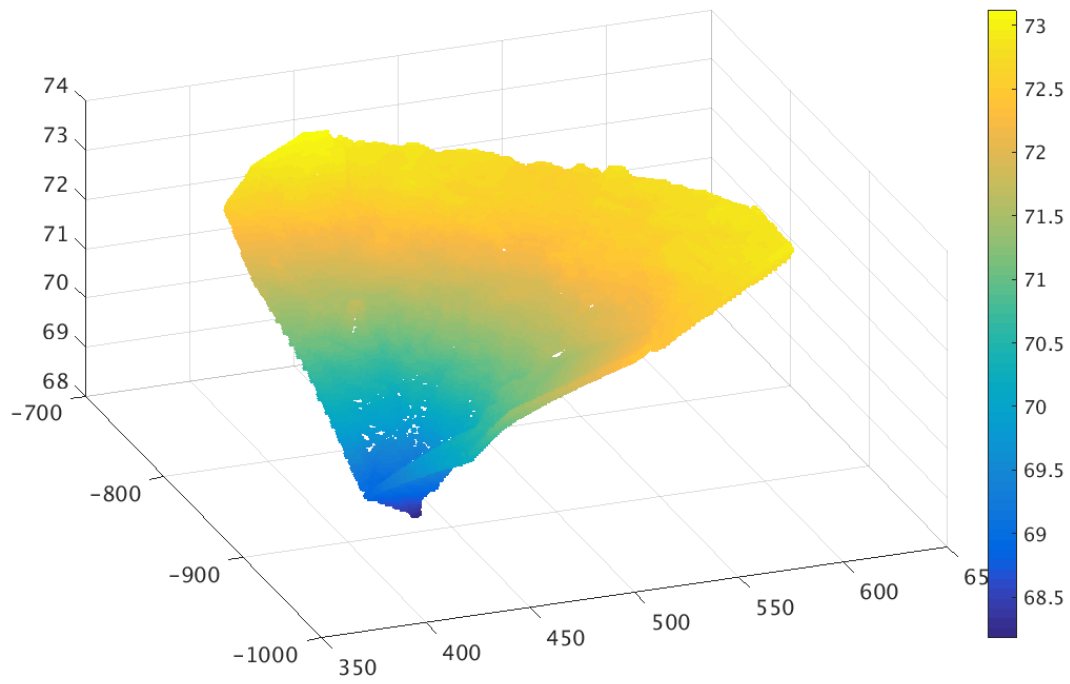


Figure 5.18 2D interpolated hydraulic potential map in dB

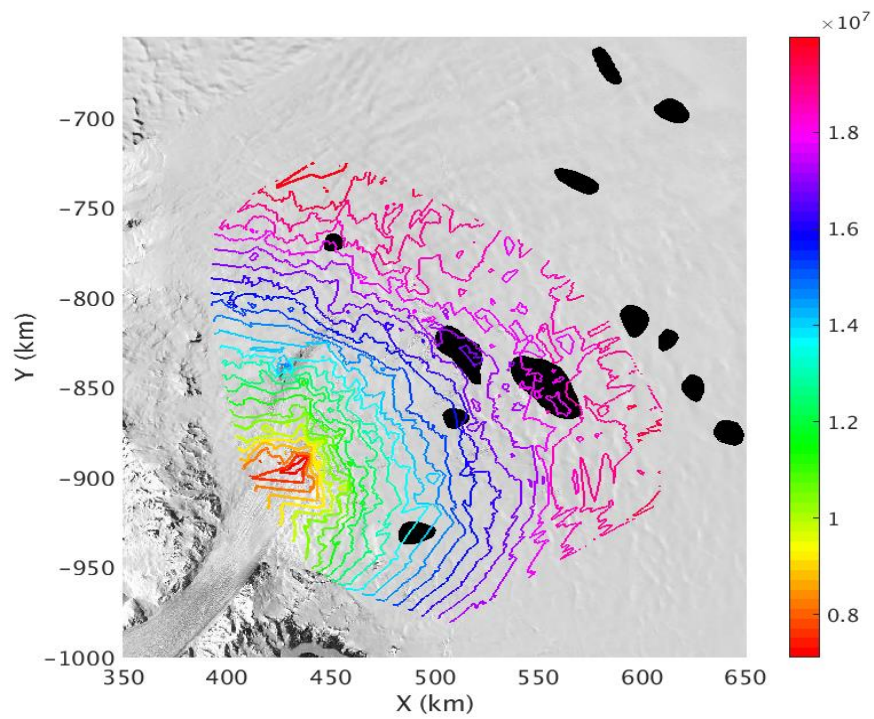


Figure 5.19 Equipotential contours of φ

As discussed, the flow paths would be perpendicular to the above shown contours of hydraulic potential. The estimated relative reflectivity map after overlapping the flow paths from [14] in the Byrd region, is shown in Figure 5.20.

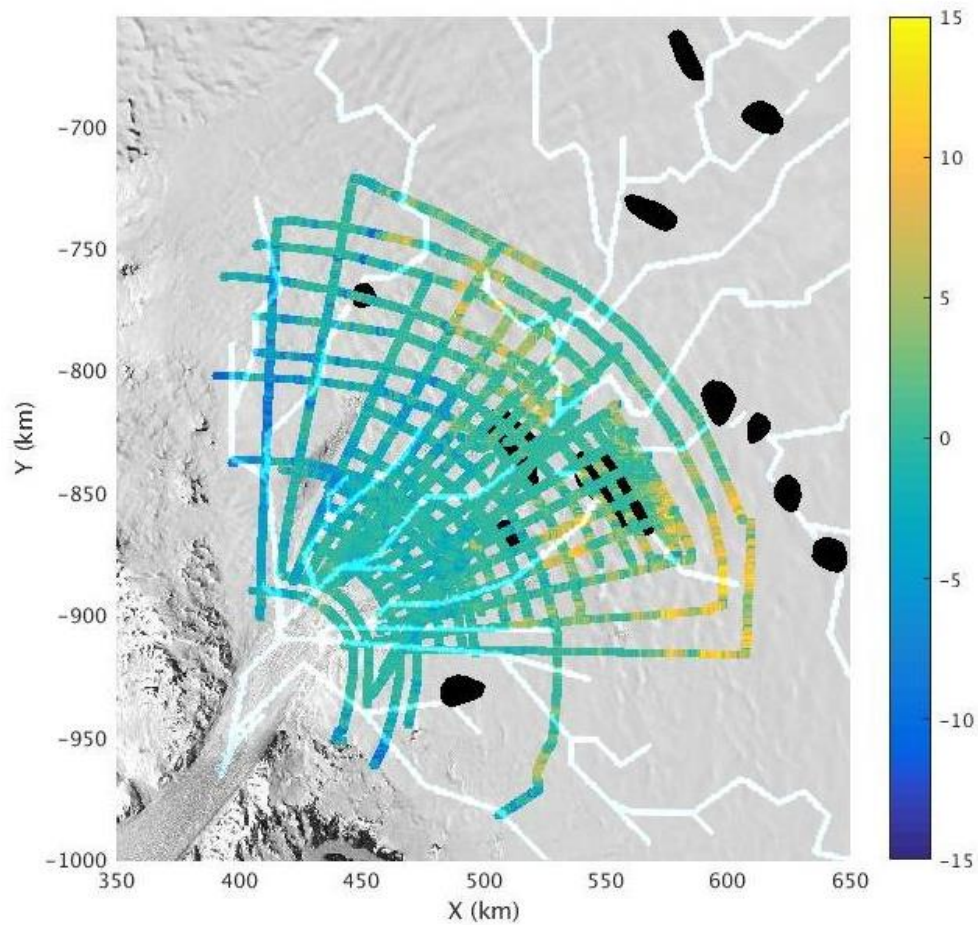


Figure 5.20 Estimated relative reflectivity map with flow paths

From the above Figure 5.20, the locations with high estimated relative reflectivity values exactly match with the predicted flow path locations, an example echogram from such location is shown in Figure 5.21 along with the corresponding flight line and estimated relative reflectivity values map.

In few locations there is an offset between the predicted flow lines and estimated potential areas with subglacial water, and this can be observed from the Figure 5.20. The estimated relative reflectivity map also discovered few new potential subglacial water flow paths. The echogram and relative reflectivity map from two such new potential flow path locations are shown in the Figure 5.22.

There is no exact match between the high relative reflective values and previously suspected lake locations based on elevation changes. Assuming there are subglacial lakes previously at the locations of the elevation changes, those lakes might have drained and the bed at those locations could have frozen by the time this data was collected (2011). This map could also be used to better understand the hydrological connectivity beneath the glacier.

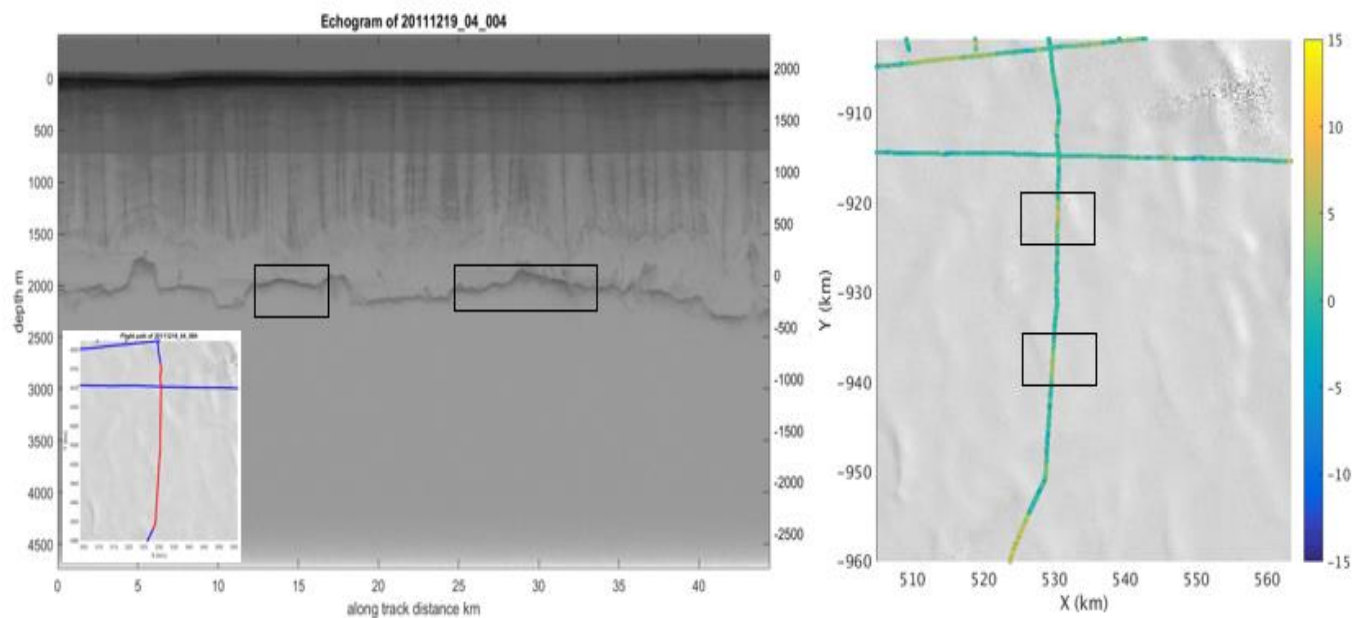


Figure 5.21 Areas with predicted flow path (highlighted in black colored rectangle) in echogram and in corresponding 20111219_04_004 flight path

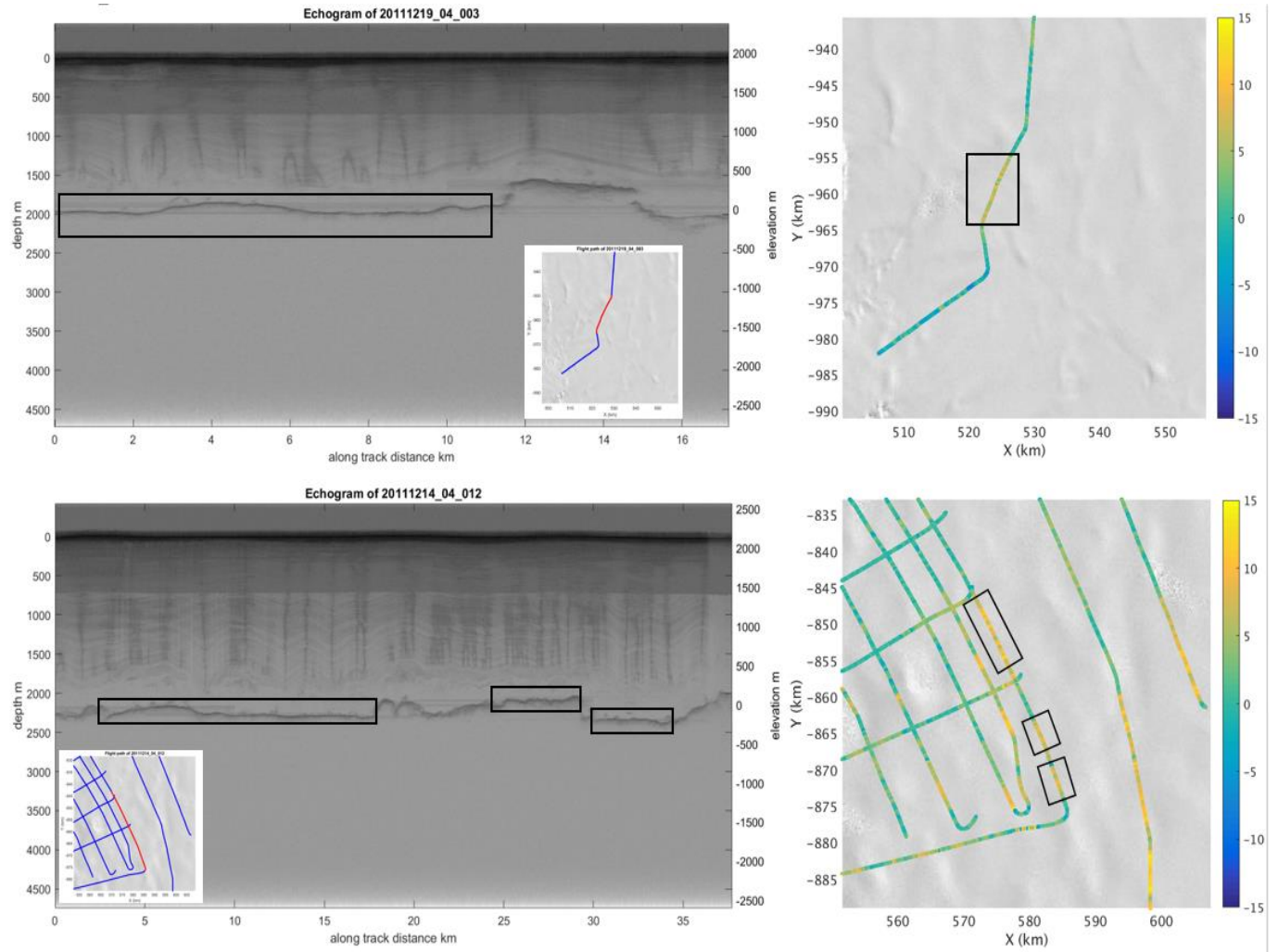


Figure 5.22 Echograms of flight path 20111214_04_012 and 20111219_04_003 (shown inside echograms) from estimated new potential subglacial water flow path locations (shown in black colored rectangles)

5.6 Clustering of estimated basal conditions

The estimated relative reflectivity values can be used to infer the subglacial materials [23] – like seawater, ground water, fresh water, frozen till, unfrozen till, frozen bedrock and unfrozen bedrock. To find the locations associated with the different subglacial materials, clustering of the estimated relative reflectivity values is done. To cluster the basal conditions, unsupervised learning algorithms like hierarchical clustering, k-Means clustering, and Gaussian Mixer Models (GMM) can be used.

K-means algorithm is selected for its fast computation speed over a large data set. K-means algorithm divides the data into clusters such that the data points in each cluster are as close to each other and data points from different clusters are as far from each other. Figure 5.23 and Figure 5.24 shows the sum of with-in cluster sums of absolute and squared point-to-centroid distances for each number of clusters assumed.

From the above figures, for the number of clusters greater than three, the sum is not decreasing significantly. So, the number of clusters present in the data is chosen as three.

Clustering is performed using the K-means algorithm is to obtain the clusters shown in Figure 5.25

According to estimated reflectivity values of subglacial materials [23], in the Figure 5.25, locations with blue-green [0 1 1] color could be the locations with unfrozen bedrock or unfrozen till (relative reflectivity values with around and greater than 10dB) and the locations with blue [0 0 1] color could be the locations with frozen bedrock (relative reflectivity values around 0 dB) and locations with blue-black [0 0 0.5] could represent the locations with frozen till (relative reflectivity values around -3 dB).

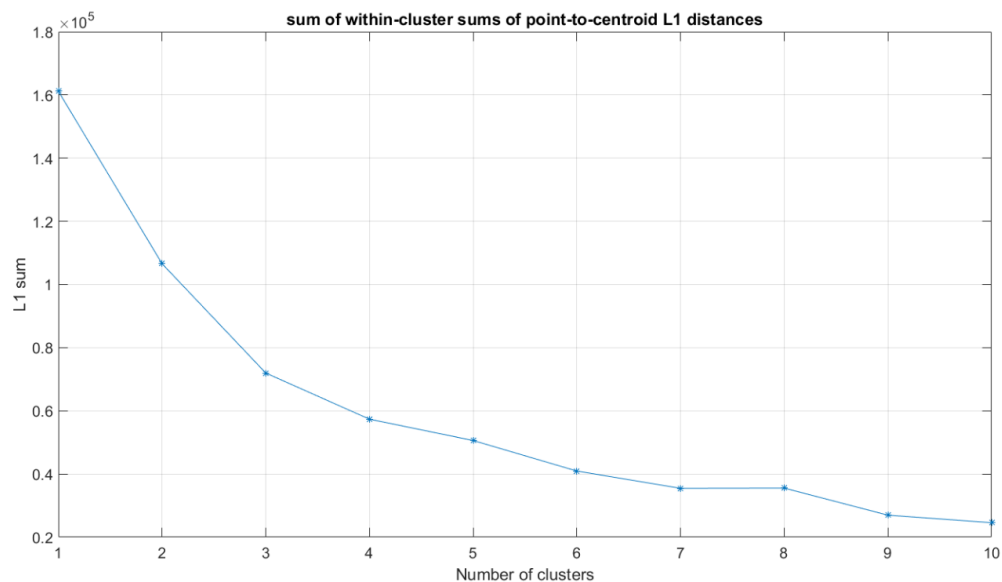


Figure 5.23 Sum of with-in cluster sums of point-to-centroid L1 distances

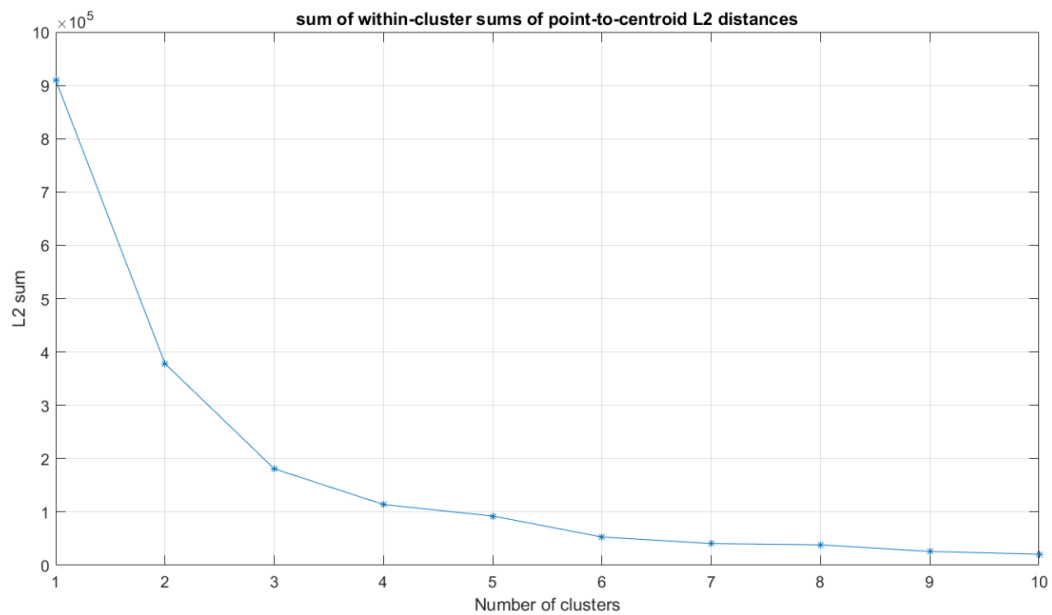


Figure 5.24 Sum of with-in cluster sums of point-to-centroid L2 distances

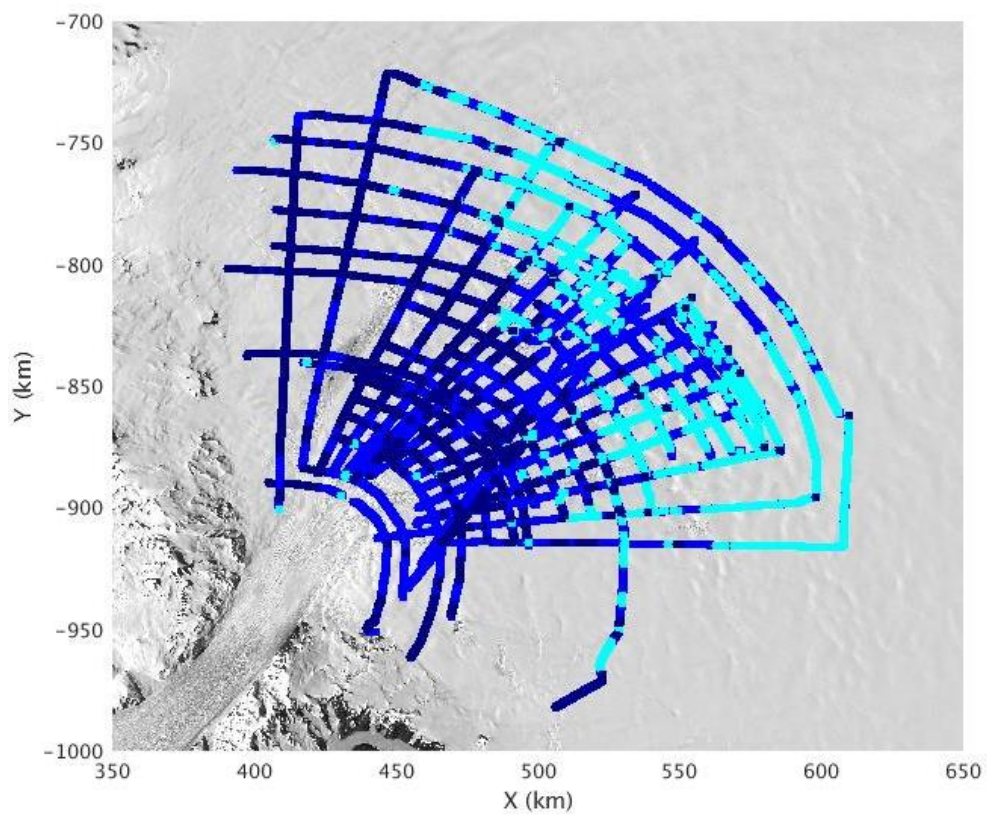


Figure 5.25 Estimated clusters of basal conditions

Chapter 6 Summary and Conclusions

6.1 Summary

In this work, the basal conditions of the Byrd Glacier are estimated using RES data by compensating the power loss due to the roughness of the air-firn and ice-bed interfaces, spherical spreading and englacial attenuation of the wave. For the received echoes, the power lost due to the roughness of the air-firn interface and the ice-bed interface are estimated using the amplitude distribution of received echoes in the along track direction. The englacial attenuation of the wave is assumed to be localized and a unique value of englacial attenuation is estimated from the received data for every 1km of along track distance. Hydraulic potential values and equipotential contours of hydraulic potential for the surveyed Byrd Glacier data are calculated. Previous methods used to find the roughness of an interface and englacial attenuation are also discussed along with their limitations and applicability to the Byrd Glacier RES data.

To validate, the estimated air-firn interface roughness parameters are compared with those estimated with the Neal's methods and Landsat Image Mosaic of Antarctica (LIMA). The relative reflectivity values estimated using the previous methods to find englacial attenuation and the method used in this work by assuming a localized constant englacial attenuation rate are compared. Abruptness index values are used to validate the estimated relative reflectivity values. Crossover analysis is done to validate the methods used. Locations with estimated high reflectivity values are compared with the previously identified locations with rapid elevation changes and previous flow paths to find correlations. The geophysical lake features are also observed in the echograms at the estimated high relative basal reflectivity locations.

The number of clusters present in the estimated relative reflectivity values is estimated as three based on the sum of with-in cluster sums of absolute and squared point-to-centroid distances, for each number of clusters assumed. The relative reflectivity values are clustered using k-means algorithm to

categorize the Byrd Glacier surveyed area into locations with unfrozen bed rock, frozen bedrock and frozen till.

6.2 Conclusions and future work

Using this work new potential locations with subglacial water are identified beneath the Byrd Glacier; these potential locations align exactly with a few previously predicted flow paths. The locations with high estimated relative reflectivity values could be a part of subglacial hydrological connectivity. The results from this work along with the previous discoveries, can be used to better understand the ice flow dynamics and subglacial hydrological connectivity underneath the Byrd Glacier.

These results can be improved by compensating the power loss caused due to roll of the aircraft at the turnings of flight paths. A detailed error analysis can be performed after every step to know the uncertainty range in the estimated relative reflectivity values. The received bed returns are also affected by the geometry of the ice – bed interface which is not compensated. By compensating these effects and by accurately calculating the englacial attenuation, the absolute reflectivity values can be obtained from the radiometrically calibrated ice bed power values.

References

- [1] Karl, T. R., J. T. Melillo, and T. C. Peterson, 2009: *Global Climate Change Impacts in the United States*. T.R. Karl, J.T. Melillo, and T.C. Peterson, Eds. Cambridge University Press, 189 pp
- [2] Douglas, Bruce C., and W. Richard Peltier, “*The puzzle of global sea-level rise*,” *Physics Today*, pp. 35-40, March 2002.
- [3] <https://sealevel.nasa.gov>
- [4] IPCC, 2013: *Climate Change 2013: The Physical Science Basis. Contribution of Working Group I to the Fifth Assessment Report of the Intergovernmental Panel on Climate Change* [Stocker, T.F., D. Qin, G.-K. Plattner, M. Tignor, S.K. Allen, J. Boschung, A. Nauels, Y. Xia, V. Bex and P.M. Midgley (eds.)]. Cambridge University Press, Cambridge, United Kingdom and New York, NY, USA, 1535 pp, doi: 10.1017/CBO9781107415324.
- [5] I. Allison, R. Alley, H. Fricker, R. Thomas, and R. Warner, “Ice sheet mass balance and sea level,” *Antarctic Sci.*, vol. 21, no. 5, pp. 413–426, Oct. 2009.
- [6] Lythe, M.B., D.G. Vaughan, and BEDMAP Consortium. 2001. BEDMAP: A new ice thickness and subglacial topographic model of Antarctica. *Journal of Geophysical Research* 106 (B6): 11335-11351
- [7] S. Solomon, D. Qin, M. Manning, Z. Chen, M. Marquis, K. B. Averyt, M. Tignor, and H. L. Miller, “*Climate Change 2007: The Physical Science Basis: Contribution of Working Group I to the Fourth Assessment Report of the Intergovernmental Panel on Climate Change (IPCC)*”. Cambridge, U.K.: Cambridge Univ. Press, 2007.
- [8] Robin GdeQ, Swithinbank CWM and Smith BME (1970) Radio echo exploration of the Antarctic ice sheet. *IASH Publ.* 86 (Symposium at Hanover 1968 – Antarctic Glaciological Exploration (ISAGE)), 97–115

- [9] Leigh A. Stearns, Benjamin E. Smith & Gordon S. Hamilton, Increased flow speed on a large East Antarctic outlet glacier caused by subglacial floods, *Nature Geoscience* 1, 827 - 831 (2008), doi: 10.1038/ngeo356
- [10] Stearns, L. A. Outlet Glacier Dynamics in East Greenland and East Antarctica. PhD thesis, Univ. of Maine (2007).
- [11] Wright & Siegert, (2012) *Antarctic Sci.* 24 (06): 659–664.
- [12] Andrew Wright and Martin Siegert, A fourth inventory of Antarctic subglacial lakes, *Antarctic Science* 24 (6), 659–664 (2012), doi: 10.1017/S095410201200048X
- [13] Wingham, D. J., Siegert, M. J., Shepherd, A. & Muir, A. S. Rapid discharge connects Antarctic subglacial lakes. *Nature* 440, 1033–1036 (2006).
- [14] Smith BE, Fricker HA, Joughin IR and Tulaczyk S (2009) an inventory of active subglacial lakes in Antarctica detected by ICESat (2003–2008). *J. Glaciol.*, 55(192), 573–595 (doi: 10.3189/002214309789470879)
- [15] Schoof, C., 2007, Ice sheet grounding line dynamics: Steady states, stability, and hysteresis: *Journal of Geophysical Research*, 112, F03S28, doi: 10.1029/2006JF000664
- [16] Gudmundsson, G. H., J. Krug, G. Durand, L. Favier, and O. Gagliardini, 2012, The stability of grounding lines on retrograde slopes: *The Cryosphere*, 6, 1497–1505, doi: 10.5194/tc-6-1497-2012.
- [17] Tsai, V. C., A. L. Stewart, and A. F. Thompson, 2015, Marine ice sheet profiles and stability under Coulomb basal conditions: *Journal of Glaciology*, 61, 205–215, doi: 10.3189/2015JoG14J221
- [18] Parizek, B. R., K. Christianson, S. Anandkrishnan, R. B. Alley, R. T. Walker, R. A. Edwards, D. S. Wolfe, G. T. Bertini, S. K. Rinehart, R. A. Bindschadler, and S. M. J. Nowicki, 2013, Dynamic (in)stability of Thwaites Glacier, West Antarctica: *Journal of Geophysical Research*, 118, 638–655, doi: 10.1002/jgrf.20044.

- [19] Fernando Rodríguez-Morales, Sivaprasad Gogineni, Carlton J. Leuschen, John D. Paden, Jilu Li, Cameron S. Lewis, Benjamin Panzer, Daniel Gomez-García Alvestegui, Aqsa Patel, Kyle Byers, Reid Crowe, Kevin Player, Richard D. Hale, Emily J. Arnold, Logan Smith, Christopher M. Gifford, David Braaten, and Christian Panton, “Advanced Multi frequency Radar Instrumentation for Polar Research” *IEEE TRANSACTIONS ON GEOSCIENCE AND REMOTE SENSING*, VOL. 52, NO. 5, MAY 2014
- [20] Anandakrishnan, Sridhar, personal communication, Sept 30, 2005.
- [21] Smith, B., I. Joughin, S. Tulaczyk, and H. Fricker. 2012. Antarctic Active Subglacial Lake Inventory from ICESat Altimetry, Version 1. Subset: Byrd, Boulder, Colorado USA. NSIDC: National Snow and Ice Data Center. doi: <http://dx.doi.org/10.7265/N57M05WS>, Date Accessed: May 2017.
- [22] https://nsidc.org/cryospwwhere/sotc/ice_sheets.html
- [23] Peters, M. E., D. D. Blankenship, and D. L. Moore, 2005, Analysis techniques for coherent airborne radar sounding: Application to West Antarctic ice streams: *Journal of Geophysical Research*, 110, B06303, doi: 10.1029/2004JB003222.
- [24] Sasha Peter Carter, *Evolving Subglacial Water Systems in East Antarctica from Airborne Radar Sounding*, Ph. D. Thesis, University of Texas at Austin, 2008
- [25] Gudmandsen, P. E. (1971), *Electromagnetic Probing of the Ice*, Golem Press, Boulder, Colo.
- [26] Joughin, I., S. Tulaczyk, J. L. Bamber, D. D. Blankenship, J. W. Holt, T. Scambos, and D. G. Vaughan, 2009, Basal conditions for Pine Island and Thwaites Glaciers, West Antarctica, determined using satellite and airborne data: *Journal of Glaciology*, 55, 245–257, doi:10.3189/002214309788608705.
- [27] Kanagaratnam, Pannirselvam, “Airborne radar for high-resolution mapping of internal layers in glacial ice to estimate accumulation rate,” Ph. D. Thesis, University of Kansas, 2002

- [28] Beckmann, P., and A. Spizzichino (1963), *the Scattering of Electromagnetic Waves from Rough Surfaces*, Elsevier, New York.
- [29] Moore, R. K. (1990), Ground echo, in *Radar Handbook*, 2nd Ed., edited by M. I. Skolnik, pp 12.1–12.54, McGraw-Hill, New York.
- [30] C. S. Neal, Radio echo determination of basal roughness characteristics on the Ross Ice Shelf, *Ann. Glaciol.*, 3, 1982, pp. 216– 221.
- [31] CReSIS. 2016. 2011 Antarctica TO Data, Lawrence, Kansas, USA. Digital Media.
<http://data.cresis.ku.edu/>.
- [32] G.S. Brown, The average impulse response of a rough surface and its applications, *IEEE Trans. Antennas Propagat.* 25, 1977, pp. 67–74.
- [33] G. K. A. Oswald and S. P. Gogineni, Recovery of subglacial water extent from Greenland radar survey data, *Journal of Glaciology*, VOL. 54, no. 184, 2008, pp. 94-106.
- [34] Paden John, “Synthetic aperture radar for imaging the basal conditions of the polar ice sheets”, Ph. D. Thesis, University of Kansas, 2006.
- [35] Cyril Grima, Dustin M. Schroeder, Donald D. Blankenship, 2014, Duncan A. Young, Planetary landing-zone reconnaissance using ice-penetrating radar data: Concept validation in Antarctica, *Planetary and Space Science*, 103:191–204.
- [36] Dustin M. Schroeder, Cyril Grima, and Donald D. Blankenship (2016). ”Evidence for variable grounding-zone and shear-margin basal conditions across Thwaites Glacier, West Antarctica.” *GEOPHYSICS*, 81(1), WA35-WA43. doi: 10.1190/geo2015-0122.1
- [37] Rignot, E., J. Mouginot, and B. Scheuchl. 2011. MEaSURES InSAR-Based Antarctica Ice Velocity Map. Boulder, Colorado USA: NASA EOSDIS Distributed Active Archive Center at NSIDC (May 2017). <http://nsidc.org/data/nsidc-0484.html>

[38] Jacobel, R. W., B. C. Welch, D. Oserhouse, R. Pettersson, and J. A. Mac-Gregor, 2009, Spatial variations of radar-derived basal conditions on Kamb Ice Stream, West Antarctica: *Annals of Glaciology*, 50, 10–16, doi: 10.3189/172756409789097504

[39] Shreve RL (1972) Movement of water in glaciers. *J. Glaciol.*, 11(62), 205–214

[40] Wright AP, Siegert MJ, Le Brocq AM and Gore DB (2008) High sensitivity of subglacial hydrological pathways in Antarctica to small ice-sheet changes. *Geophys. Res. Lett.*, 35(17), L17504 (doi: 10.1029/2008GL034937)